8-30-2023

Improving Irrigant Flow Characteristics for Enhanced Root Canal Therapy: A Numerical Study

BIBEK BANJADAY
Grand Valley State University

ScholarWorks Citation
BANJADAY, BIBEK, "Improving Irrigant Flow Characteristics for Enhanced Root Canal Therapy: A Numerical Study" (2023). *Masters Theses*. 1111.
https://scholarworks.gvsu.edu/theses/1111

Improving Irrigant Flow Characteristics for Enhanced Root Canal Therapy: A Numerical Study

Bibek Banjaday

A Thesis Submitted to the Graduate Faculty of

GRAND VALLEY STATE UNIVERSITY

In

Partial Fulfillment of the Requirements

For the Degree of

Masters of Science in Engineering

Padnos College of Engineering and Computing

August 2023

Thesis Approval Form

GRAND VALLEY
STATE UNIVERSITY

The signatories of the committee below indicate that they have read and approved the thesis of Bibek Banjaday in partial fulfillment of the requirements for the degree of Master of Science in Engineering.

08/03/23

Sanjivan Manoharan, Thesis committee chair — Date

07/27/23

Shabbir Choudhuri, Committee member — Date

7/27/23

Tikran Kocharian, Committee member — Date

Accepted and approved on behalf of the
Padnos College of Engineering and Computing

Dean of the College

August 4, 2023

Date

Accepted and approved on behalf of the
Graduate Faculty

Dean of The Graduate School

8/30/2023

Date

Acknowledgments

I would like to express my deepest appreciation to my thesis supervisor, Dr. Sanjivan Manoharan who guided me through the ups and downs of the journey. He has provided me with constant motivation and technical support to move forward. Moreover, he consistently provided a comprehensive understanding of the overarching concept while meticulously analyzing the intricacies during the entire journey. The successful completion of this work wouldn't have been possible without his unwavering encouragement and steadfast support, which played a pivotal role in keeping me motivated and focused throughout the entire process.

I would like to express my sincere appreciation to Prof. Tikran Kocharian, who has provided me with constant technical support and motivation during this work. I would like to thank Dr. Shabbir Choudhuri for his constant guidance and support throughout the journey.

I would like to thank Dr. Samhita Rhodes, Graduate Program Director, and Dr. Wael Mokhtar, Director of Engineering, for helping me through the process of completing the work.

I would also like to thank my friends, Bibek Kafle and Bibash Lama, who constantly motivated me during the process and helped me with meaningful discussions. Finally, I would like to express my gratefulness to my parents, my relatives, my brothers, and my friends who have constantly supported me during this thesis work.

Abstract

This numerical study investigates the flow characteristics within a root canal during a manual endodontic treatment. To underscore the difference in root canal geometry, a simplified root canal (frustum of a cone) and a more complex (realistic) root canal geometry were considered. The needle utilized in all simulations is a side-vented 30G KerrHaweIrrigation Probe, KerrHawe SA, Bioggio, Switzerland. For both root canal geometries, the effect of variation of fluid inlet velocity, needle insertion depth, and needle tilt angle on flow characteristics was examined via velocity contours, turbulent intensity, wall shear stress, and streamline and vector plots. The fluid was Sodium Hypochlorite, and fluid inlet velocities of 6 m/s, 8.6 m/s and 12 m/s were considered. Needle insertion depths of 1 mm, 2 mm, and 3 mm from the working length, and needle tilt angles of 1^o and 2^o (both clockwise and counterclockwise) were considered. The complex geometry showed better flow penetration, significantly lower apical pressures, and almost half the shear stress as flow velocity increased when compared to the simplified model. For the complex geometry, as the needle insertion depth increased the apical pressures were almost four times smaller, better flow penetration was seen, differences in turbulent intensity patterns right above the apical third were witnessed, and wall shear stresses were almost half when compared to the simplified geometry. Finally, with respect to tilt angle, clockwise rotation had better flow penetration, wall shear stresses were more than halved, and apical pressure was highest at 2^o counterclockwise rotation for complex geometry. Interestingly, for the simplified model, apical pressure was highest for 1^o clockwise tilt. The optimum combination of input parameters includes fluid inlet velocity of 8.6 m/s, needle insertion depth of 2 mm, and 1^o clockwise rotation of needle. Subsequently, the side vented needle was redesigned using fundamental fluid mechanics principles to enhance flow characteristics, especially at the apical third of the realistic root canal geometry.

Table of Contents

List of Tables

List of Figures

Chapter 1 Introduction

1.1 Introduction

Root canal therapy, also called endodontic treatment, is a dental procedure to treat infected pulp of a tooth. When the pulp becomes infected, it is necessary to treat it to get relief from severe tooth pain. Successful root canal treatment requires understanding of the anatomy of the tooth. The tooth can be divided into two parts: the crown which is the outer region, and the root which is the inner region. The pulp is the soft tissue inside the tooth which consists of nerves, tissues and blood vessels and is located at the inner region of the tooth surrounded by dentin, which is the inner hard region of tooth covered by the white enamel visible inside the mouth. The pulp expands from the crown of the tooth to the root where it connects the nerves and supporting ligament. Figure 1 identifies the main parts of a tooth.

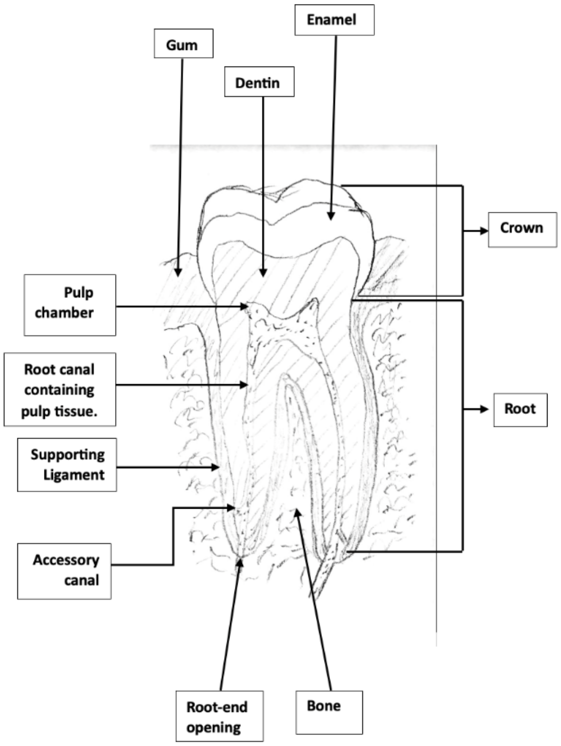

Figure 1: Geometry of the root canal

Root canal therapy is needed when the pulp is infected or inflamed, which could be due to internal or external factors. The procedures for the root canal therapy are mentioned below:

a. Initially, the tooth is X-Rayed to be aware of the condition. The root canal treatment is only executed if there is sign of inflammation or infection in the root canal. Figure 2 shows the cross-section of the tooth where there is decay in the enamel and dentin region of the tooth. The root canal is shown for two conditions: inflammation on the right side and abscess on the left. Abscess is the condition when pus is developed in the ligament of the tooth at the bottom of the root canal. Inflammation and abscess are the conditions caused by the bacterial infection inside the tooth.

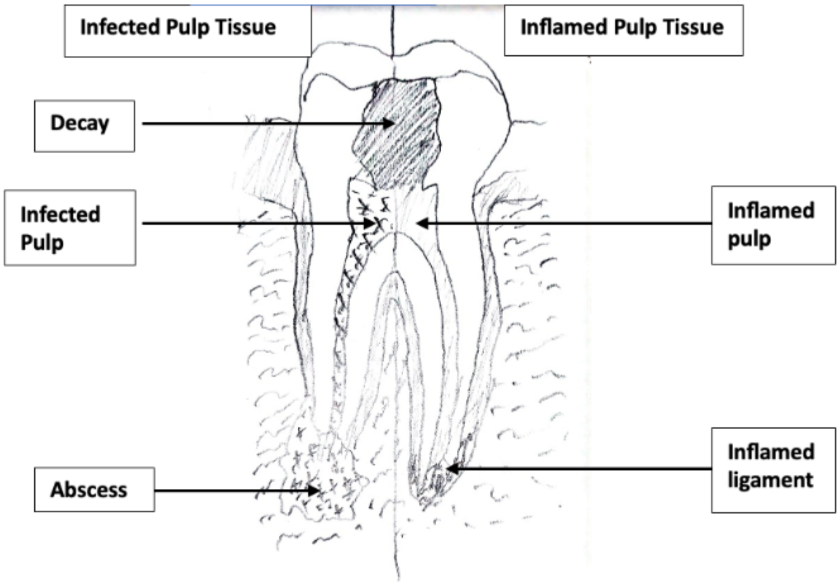

Figure 2: Infection in the root canal

b. The second procedure is to prepare the cavity in the crown for accessing the pulp chamber inside the dentin. The pulp is subsequently removed, and the drilling operation is done to make the area well-prepared to ease the filling of the material inside the root canal.

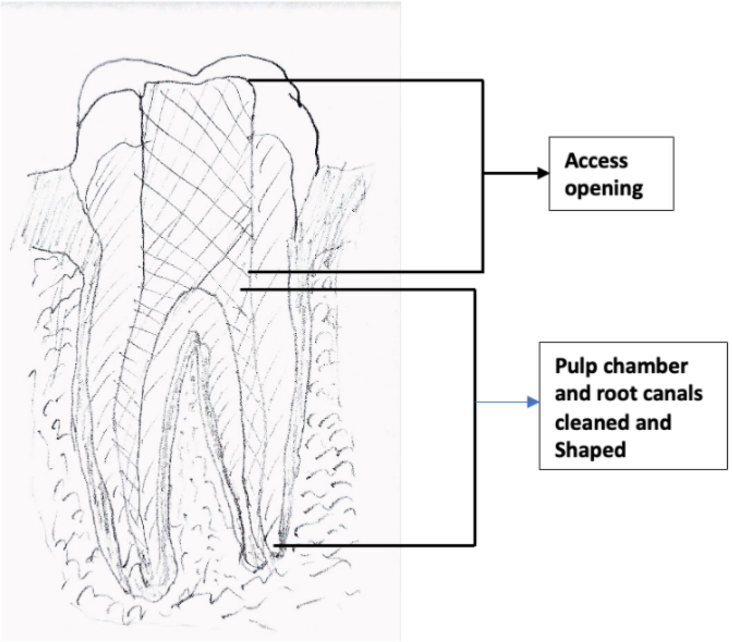

Figure 3: Mechanically prepared root canal

c. The root canal is irrigated so as to remove the remnant necrosis tissues and disinfect the root canal wall from the bacteria, which could be the major reason for the failure of root canal treatment. The fluid mostly utilized for root canal irrigation is Sodium Hypochlorite (NaOCl). This irrigant not only kills the bacteria but also dissolves the tissue, and this procedure should be performed very delicately.

d. The cavity is filled with the material called gutta percha with adhesive cement to seal the cavity completely. Sometimes the crown cap is kept ensuring the maximum protection of the tooth.

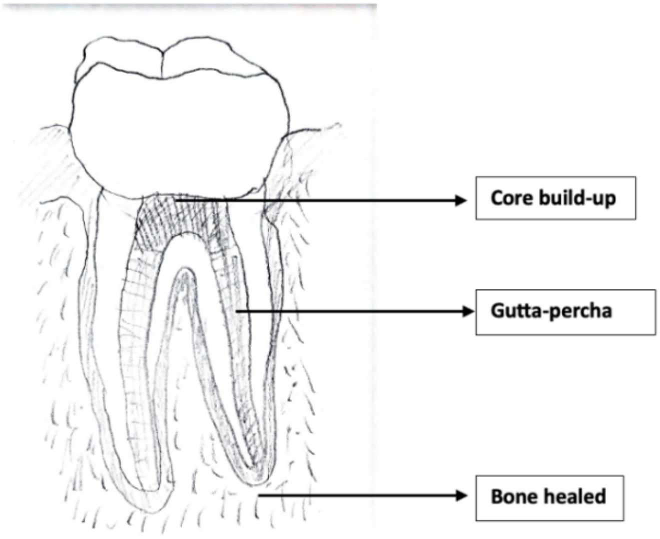

Figure 4: Root canal filled with gutta-percha

There are a several advanced technologies to experimentally study irrigation within a larger scaled version of the root canal or ex-vivo. These include CBCT (Cone Beam Computed Tomography) and PIV (Particle Image Velocimetry) techniques. PIV is an optical method where the image of the entrained particles is utilized to study the flow characteristics which could be used to obtain instantaneous velocity. The tracer particles are assumed to be similar to the bulk flow properties. The movement of the tracer particles are a primary factor for detecting the flow characteristics inside the root canal. CBCT is the technique to obtain the 3D image of the mouth. This method utilizes the X-ray beam in the conical shape to obtain the radiographic image which could be utilized while performing the endodontic experiment to make the treatment efficient.

While such techniques are useful in understanding flow patterns, they provide no insights into other important parameters such as wall shear stress, flow penetration depth, and turbulent intensity. This is where simulation of the process via Computational Fluid Dynamics (CFD) lends a helping hand. Using CFD, one can study the effect of process parameters on irrigant flow characteristics to aid in enhancing the efficacy of root canal therapy.

1.2 Scope of Study

This study utilizes the realistic root canal of a canine, for which, to the author's knowledge, no extensive study exists. Furthermore, there have been very few studies that use the more realistic (complex) root canal geometry to analyze flow patterns and irrigation efficacy. The first step of this work is to validate the simulation setup with existing data available in the literature. Given that almost all studies are associated with the simplified root canal, the validation study was done with this geometry as well. Next, the effect of variation of process parameters such as fluid inlet velocity, needle insertion depth, and needle tilt angle on flow behavior within the root canal was studied. This was achieved by studying contours obtained for velocity, turbulent intensity, wall shear stress, flow penetration depth, and apical pressure. These data provide baseline for the comparison of the trends of simplified root canal geometry with realistic geometry. All simulations were done with 30G side vented needles.

The realistic geometry was modeled in CAD using the data provided by Razumova et al. [17]. The numerical setup is kept the same for both root canal geometries, and the effect of the input parameters including variation of irrigant injection speed, needle insertion depth and needle tilt angle on flow within root canal are studied. These results are then compared to those obtained from the simplified root canal study to identify differences in values and trends. Following this, the best possible combination of input parameters is identified. This combination is subsequently used to investigate modified needle geometry.

The final section of this study involves modifying the existing side vented needles using basic fluid mechanics principles to enhance flow characteristics within root canal. The goal was to keep the changes as realistic as possible to aid in manufacturability of the needle. The intention was to improve the turbulence intensity, especially at the apical third.

1.3 Research Questions

a. Are the trends of flow characteristics same for the simplified and realistic root canal geometry?

b. Can the flow characteristics be improved for realistic root canal geometry?

1.4 Theoretical Background

The governing equations for any numerical fluid flow are the conservation of mass, momentum, and energy. Depending on the type of flow, selection of turbulent model will involve other equations as well.

1.4.1 Conservation of Mass

Conservation of mass states that for a specified control volume, the rate of mass entering the system is always equal to the rate of mass exiting the system plus accumulation rate within the control volume itself. The general equation for the conservation of mass in differential form can be written as:

$$\frac{\partial \rho}{\partial t} + \frac{\partial (\rho u)}{\partial x} + \frac{\partial (\rho v)}{\partial y} + \frac{\partial (\rho w)}{\partial z} = 0 \tag{1}$$

Here,

ρ = density

u = x-component of velocity

v= y- component of velocity

w = z-component of velocity

If the flow is incompressible (i.e., flow density is constant) and is also at steady state, the equation simplifies to:

$$\frac{\partial u}{\partial x}+\frac{\partial v}{\partial y}+\frac{\partial w}{\partial z}=0 \tag{2}$$

1.4.2 Conservation of Momentum

Conservation of momentum is based on Newton's Second law of motion, i.e., net force acting on the system is mass multiplied by acceleration. The forces acting on the fluid system can are typically grouped into body forces and surface forces. Pressure and viscous forces are called surface forces (normal and shear stresses), while gravity is considered a body force. The conservation of momentum in the x, y and z direction. The differential form of the conservation of momentum is given as follows:

$$\frac{\partial(\rho u)}{\partial t}+\frac{\partial(\rho uu)}{\partial t}+\frac{\partial(\rho vu)}{\partial t}+\frac{\partial(\rho wu)}{\partial t} = -\frac{\partial p}{\partial x}+\frac{\partial \tau_{xx}}{\partial x}+\frac{\partial \tau_{xy}}{\partial y}+\frac{\partial \tau_{zx}}{\partial z}+\rho f_x \tag{3}$$

$$\frac{\partial(\rho v)}{\partial t}+\frac{\partial(\rho uv)}{\partial t}+\frac{\partial(\rho vv)}{\partial t}+\frac{\partial(\rho wv)}{\partial t} = -\frac{\partial p}{\partial y}+\frac{\partial \tau_{xy}}{\partial x}+\frac{\partial \tau_{yy}}{\partial y}+\frac{\partial \tau_{zy}}{\partial z}+\rho f_y \tag{4}$$

$$\frac{\partial(\rho w)}{\partial t}+\frac{\partial(\rho uw)}{\partial t}+\frac{\partial(\rho vw)}{\partial t}+\frac{\partial(\rho ww)}{\partial t} = -\frac{\partial p}{\partial z}+\frac{\partial \tau_{xz}}{\partial x}+\frac{\partial \tau_{yz}}{\partial y}+\frac{\partial \tau_{zz}}{\partial z}+\rho f_z \tag{5}$$

Here, ρ denotes density, 'p' denotes static pressure, and 'u', 'v', and 'w' denote component of velocity in the x, y and z-direction, respectively. 'τ_{xx}', 'τ_{yy} ', and 'τ_{zz}' are normal stress in x, y and z-direction, respectively, while 'τ_{xy} ', and 'τ_{xz}' are shear stresses in x-direction, 'τ_{yx} ', and 'τ_{yz}' are shear stress in y-direction, 'τ_{zx} ', and 'τ_{zy}' are shear stress in z-direction, and f_x, f_y, and f_z denote body forces in x, y and z-direction, respectively.

1.4.3 Conservation of Energy

The law of conservation of energy is based on the first law of thermodynamics, which states that the rate of increase in energy is equal to sum of rate of heat added and rate of work done. The rate of increase in energy includes increase in kinetic energy, potential energy and internal energy. The equation for the conservation of energy can be written as:

$$\rho\frac{De}{Dt} = \rho q + \frac{\partial}{\partial x}\left(k\frac{\partial T}{\partial x}\right) + \frac{\partial}{\partial x}\left(k\frac{\partial T}{\partial x}\right) + \frac{\partial}{\partial x}\left(k\frac{\partial T}{\partial x}\right) - p\left(\frac{\partial u}{\partial x} + \frac{\partial v}{\partial y} + \frac{\partial w}{\partial z}\right) + \tau_{xx}\frac{\partial u}{\partial x} + \tau_{yz}\frac{\partial u}{\partial y} + \tau_{zx}\frac{\partial u}{\partial z} + \tau_{xy}\frac{\partial v}{\partial x} + \tau_{yy}\frac{\partial v}{\partial y} + \tau_{zy}\frac{\partial v}{\partial z} + \tau_{xz}\frac{\partial w}{\partial x} + \tau_{yz}\frac{\partial w}{\partial y} + \tau_{zz}\frac{\partial w}{\partial z} \tag{6}$$

Here, ρ denotes density, ‘p’ denotes static pressure, ‘u’, ‘v’, and ‘w’ denote component of velocity in x, y and z-direction, respectively. ‘τ_{xx}’, ‘τ_{yy}’ , and ‘τ_{zz}’are normal stress in x, y and z-direction, respectively, ‘τ_{xy}’, and ‘τ_{xz}’ are shear stress in x-direction, ‘τ_{yx}’, and ‘τ_{yz}’ are shear stress in y-direction, ‘τ_{zx}’, and ‘τ_{zy}’ are shear stress in z-direction, and f_x, f_y, and f_z denotes body forces in x, y and z-direction, respectively. The k denotes thermal conductivity and q denotes overall heat added to the control volume.

1.4.4 Navier – Stokes Equations

Navier-stokes equations are set of partial differential equations governing the fluid motion. It assumes that the fluid is isotropic, which implies the viscous stresses aren’t function of direction and the fluid is Newtonian, which implies the viscous stresses are proportional to strain rate. With these assumptions, the stress components can be written as:

$$\tau_{xx} = \lambda(\frac{\partial(u)}{\partial x} + \frac{\partial(v)}{\partial y} + \frac{\partial(w)}{\partial z}) + 2\mu\frac{\partial u}{\partial x} \tag{7}$$

$$\tau_{yy} = \lambda(\frac{\partial(u)}{\partial x} + \frac{\partial(v)}{\partial y} + \frac{\partial(w)}{\partial z}) + 2\mu\frac{\partial v}{\partial y} \tag{8}$$

$$\tau_{zz} = \lambda(\frac{\partial(u)}{\partial x} + \frac{\partial(v)}{\partial y} + \frac{\partial(w)}{\partial z}) + 2\mu\frac{\partial w}{\partial z} \tag{9}$$

$$\tau_{xy} = \tau_{yx} = \mu(\frac{\partial v}{\partial x} + \frac{\partial u}{\partial y}) \tag{10}$$

$$\tau_{xz} = \tau_{zx} = \mu(\frac{\partial u}{\partial z} + \frac{\partial w}{\partial x}) \tag{11}$$

$$\tau_{yz} = \tau_{zy} = \mu(\frac{\partial w}{\partial y} + \frac{\partial v}{\partial z}) \tag{12}$$

Here, μ denotes first viscosity coefficient, which is related to linear strain rate, and λ denotes second viscosity coefficient which is equal to -2μ/3. Combining relevant equations results in the Navier-Stokes equations for incompressible flow which are given below:

$$\rho(\frac{\partial u}{\partial t} + u\frac{\partial u}{\partial x} + v\frac{\partial u}{\partial y} + w\frac{\partial u}{\partial z}) = -\frac{\partial p}{\partial x} + \mu(\frac{\partial^2 u}{\partial x^2} + \frac{\partial^2 u}{\partial y^2} + \frac{\partial^2 u}{\partial z^2}) + \rho g_x \tag{13}$$

$$\rho(\frac{\partial v}{\partial t} + u\frac{\partial v}{\partial x} + v\frac{\partial v}{\partial y} + w\frac{\partial v}{\partial z}) = -\frac{\partial p}{\partial y} + \mu(\frac{\partial^2 v}{\partial x^2} + \frac{\partial^2 v}{\partial y^2} + \frac{\partial^2 v}{\partial z^2}) + \rho g_y \tag{14}$$

$$\rho(\frac{\partial w}{\partial t} + u\frac{\partial w}{\partial x} + v\frac{\partial w}{\partial y} + w\frac{\partial w}{\partial z}) = -\frac{\partial p}{\partial z} + \mu(\frac{\partial^2 w}{\partial x^2} + \frac{\partial^2 w}{\partial y^2} + \frac{\partial^2 w}{\partial z^2}) + \rho g_z \tag{15}$$

1.4.5 K-Epsilon Turbulence model

K-Epsilon (k-ɛ) is an extensively used two-equation, turbulence model in computational fluid dynamics. The application of k-ɛ turbulence model is generally best suited for regions with small separation. This model is based on the idea of turbulence dissipation rate (epsilon) and turbulent kinetic energy (k). The governing equation for k-epsilon turbulence model is:

$$\frac{\partial \rho K}{\partial \tau}+\frac{\partial \rho U_j K}{\partial x_j}=\frac{\partial \rho}{\partial x_j}\left[\left(\mu+\frac{\mu_t}{s_k}\right)\frac{\partial K}{\partial x_j}\right]+P_k+G_k-\rho e \tag{16}$$

$$\frac{\partial \rho e}{\partial \tau}+\frac{\partial \rho \mathrm{U}_j e}{\partial \mathrm{x}_j}=\frac{\partial}{\partial \mathrm{x}_j}\left[\left(\mu+\frac{\mu_t}{s_e}\right)\frac{\partial e}{\partial \mathrm{x}_j}\right]+\mathrm{C}_{e1}(\mathrm{P}_k+\mathrm{C}_{e3}\mathrm{G}_k)\frac{e}{K}-\mathrm{C}_{e2}\rho\frac{e^2}{K} \tag{17}$$

Here, ρ denotes density, ‘K’ denotes turbulent kinetic energy, ‘m’ denotes turbulent viscosity, ‘m_t’ denotes coefficient of turbulent viscosity, ‘e’ denotes turbulence dissipation rate, and ‘P_k’ denotes turbulent production term, which is rate of transfer of mean flow kinetic energy to turbulent kinetic energy. ‘G_k’ is a term for improving behavior near solid walls and streamline curvature effects, ‘U_j’ denotes component of velocity in x, y or z direction, ‘x_j’ denotes the spatial co-ordinates, s_k and s_e are model constants added to stabilize the k-epsilon model, and C_{e1}, C_{e2}, C_{e3} are empirical constants in the model.

1.5 Definition

Working Length: The working length is defined as the distance from the top of the root canal to the point where the mechanical preparation of the root canal is done. Generally, the working length in actual practice is 0.5 – 1 mm. In this study, the working length is kept at 0.6 mm.

Needle Insertion Depth: Needle insertion depth represents the position of needle short of working length. For example, if the needle insertion depth is 1 mm, the tip of the needle is placed at a distance of 1.6 mm from the bottom of the root canal. As needle insertion depth increases, the needle moves away from the apical foramen.

Flow Penetration Depth: The flow penetration depth is the distance measured from the tip of the needle to the plane which corresponds to the lowest point of the streamline. To measure this, a plane is created at the lowest point of the streamline, and the distance from the bottom of the needle to this plane is measured using numerical software.

Chapter 2 Literature Review

The success rate of a root canal treatment varies between 86 and 98 % [1]. A survey conducted by American Dental Association in 2000 indicated that the number of root canal treatments conducted ranged from 24 to 50 million [2] per year. Given this high number, even a 2% failure rate amounts to 0.48 to 1 million cases, which isn't a small number. Given that root canal complications can have severe consequences on humans, it is important to consider every procedure deliberately to ensure the effectiveness of root canal treatment. Bacteria remaining in the root canal is one of the major reasons for the failure of root canal therapy [3]. Therefore, it is important to make sure that the root canal is free of bacteria as much as possible before filling it up with material. In addition, the necrosis tissues if left untreated will create an environment that aids in the growth of bacteria which can worsen the infection in the root canal. Thus, irrigation is the critical step of the root canal treatment since it cleans the necrosis tissues and dentine remnants and disinfects the bacteria present in the root canal [4].

The selection of an appropriate irrigant is important in root canal irrigation to effectively dissolve necrotic tissues and disinfect the root canal system. Sodium Hypochlorite (NaOCl) is one of the most widely used irrigants for root canal treatment. In 1984, John W. Harrison conducted a study that highlighted the benefits of using Sodium Hypochlorite as an irrigant in root canal therapy [5]. Harrison found that Sodium Hypochlorite exhibited excellent dissolving properties for necrotic tissues, demonstrated potent antimicrobial properties, and effectively eliminated bacteria and biofilms within the root canal. Azhar Ali et al. [6] in 2022 conducted a study that reaffirmed Sodium Hypochlorite as an excellent irrigant for root canal therapy and validated the effectiveness of Sodium Hypochlorite in dissolving organic debris along with its antimicrobial characteristics.

While NaOCl (Sodium hypochlorite) is considered an effective irrigant, it is essential to ensure its safe use to prevent any mishaps or complications for both the patient and the health worker [7].

In 2006, Boutsioukis et al. conducted experiments with the assistance of various dentists in using prepared root canals [8]. The objective of the study was to measure the pressure and flow rate associated with three different endodontic needles: 25-Gauge, 27-Gauge, and 30-Gauge. The experiment revealed that the smaller-diameter needles (higher gauge) resulted in higher pressure readings. The maximum pressure recorded within the root canal ranged from 400 – 550 kPa. Furthermore, the study found that the irrigant flowrate was a significant factor which directly influenced the flow beneath the needle tip. While experiments are very useful in studying the effect of certain parameters on performance within the root canal, they do not help us understand certain intricate details such as flow pattern and characteristics. It is here that Computational Fluid Dynamics (CFD) plays a significant role in improving our understanding and optimizing the process of root canal irrigation. It helps in visualizing fluid dynamics, optimizing irrigation techniques, assessing fluid dynamics parameters, studying irrigant behavior, and enabling virtual experimentation. However, CFD studies must be validated to some degree with experimental data.

In 2009, Boutsiokis et al. [9] conducted an experiment to validate a Computational Fluid Dynamics (CFD) model by comparing it with actual experimental data using high-speed imaging; PIV was employed to obtain the experimental results. The study focused on a simplified root canal (without apical foramen), a geometrical frustum of a cone, and utilized a 30-gauge (30G) needle during the experiments. Water was the irrigant, and an inlet flow velocity of 8.6 m/s (0.26 mL/s) was applied since this mimicked the flow of a clinical trial. The study found a close agreement between the experimental and simulated results thereby instilling confidence in the CFD model. The same study also considered the effects of needle offset and observed that small lateral displacements had limited impact on the flow characteristics. In the same year, Boutsioukis et al. [10] conducted experiments on simplified root canals with an apical foramen (a very constricted region at the bottom of the root canal) to study the impact of different irrigant flow rates. Flow speeds of 1 m/s (0.030 mL/s), 6 m/s (0.18 mL/s), 12 m/s (0.36 mL/s), 24 m/s (0.72 mL/s), and 36 m/s (1.07 mL/s) were applied at the inlet of the root canal. Sodium Hypochlorite was used as the irrigant. A 30G needle was positioned 3 mm short of the working length and centered within the root canal. The authors concluded that the replacement of irrigant occurred primarily within 1-1.5 mm from the bottom of the needle, suggesting that the irrigant had limited penetration beyond this point. This implies that the fluid penetration depth was 1 – 1.5 mm measured from the needle tip. Variation of inlet velocity significantly influenced the flow pattern within the root canal.

Boutsioukis et al. [11] also conducted a study focusing on the analysis of flow within the root canal by considering different needle geometries. Both open-ended and closed-end needle geometries were assessed. The irrigant, Sodium Hypochlorite, was given an inlet velocity of 8.6 m/s (0.26 mL/s). The primary objective of the study was to assess the replacement of the irrigant (i.e., mixing efficiency) at the apex of the root canal. The analysis focused on evaluating parameters such as velocity, apical pressure, and shear stress on the canal wall to understand the flow dynamics. They concluded that the open-ended needle geometry was more effective in terms of irrigant replacement; however, it was observed that the use of open-ended needles resulted in higher apical pressure.

Boutsioukis et al. [11] also studied the effect of needle insertion depth of 1, 2, 3, 4, and 5 mm short of working length for open ended (flat bottomed) and side vented 30G needles. The effects on apical pressure, wall shear stress, and fluid replacement were observed. The study revealed that regardless of the needle position, a similar flow pattern was observed beyond the needle. The working length is the distance from the top of the canal to the bottom of the prepared region. In the study, it was found that the irrigant replacement occurred when the needle was positioned 1 mm from the working length for the side vented geometry, whereas open ended needle showed irrigant replacement even when placed 2 mm from the working length. This shows that open ended needles have better flow penetration over their side vented counterparts. For both needles, shear stress was found to decrease with the increase in needle distance from the working length (i.e., as the needle moved further away from the apical region). Regarding apical pressure, it was found to decrease as the distance from the working length increased for both types of needles. More importantly, the open-ended needle induced higher pressure at the apical foramen when compared to the side-vented needle.

In their 2010 study, Boutsioukis et al. [13] evaluated the velocity, shear stress, and apical pressure associated with different taper configurations of root canals using 30G, side-vented needles. The study considered various root canal dimensions, including size 30 with 0.02 taper, size 30 with 0.04 taper, size 30 with 0.06 taper, ProTaper F3, and size 60 with 0.02 taper. In each case, the needle was positioned concentrically with the root canal, 3 mm short of the working length. The flow velocity of 8.6 m/s was maintained for all root canal configurations during the simulations. The authors found that regardless of the needle type, the wall shear stress decreased as the taper of the root canal increased. Furthermore, the study revealed that the apical pressure gradually decreased with an increase in the taper of the root canal for both types of needles. However, the open needle imposed greater apical pressure when compared to the side-vented needle, same observations reported by as Boutsioukis et al. [11].

E. Konstantinidi, et al [4] initiated the review study where relevant findings were collected for the comparison of negative pressure irrigation vs. positive pressure irrigation. Negative pressure irrigation works with the method of suctioning the liquid form the needle placed closer to the working length. The negative pressure irrigation prevents the chances of apical extrusion which is possible where the flow is directly ejecting into the root canal. However, no significant evidence was found to declare the superiority of one method versus the other one.

In 2014, Zeya Quadri et al. [14] conducted an analysis of irrigant flow in maxillary (upper jaw) and mandibular (lower jaw) teeth using a simplified model (geometrical frustum of a cone) of the root canal. The study utilized a 30G side-vented needle for the simulation. A flow velocity of 8.6 m/s (0.26 mL/s irrigant flowrate) was considered. Results indicated that in order to achieve similar results in maxillary teeth compared to mandibular teeth, it was necessary to insert the needle at a greater depth for maxillary teeth. Furthermore, the study observed higher wall shear stress in maxillary teeth compared to mandibular teeth as the irrigant exited the needle.

Since manual irrigation involves human intervention, there are multiple human factors and needle parameters that influence the performance of root canal irrigation [8]. Therefore, automation of the irrigation set up is important. In their 2021 study, Kavalipurapu V. Teja et al. [15] attempted to develop a device for automating the root canal irrigation procedure and delivering the irrigant at a constant flow rate. Unfortunately, there are various factors that are involved in the irrigation that should be standardized so that it can be utilized in the automation setup to ensure consistent and reliable results.

Na Zhou et al. [16], experimented on different needle working lengths and root canal curvatures where the model of root canal was generated from the real tooth having a curvature of 23.4°. The 30G needle was utilized where the working length of short of 4.75 mm, 5 mm, 5.25 mm, and 5.5 mm were used to position the needle. Moreover, the curvature was also varied to 0°, 5°, 10°, 20°, and 30^0 in the software. It was observed that the efficiency of irrigation improved with the decrease in needle working length (needle closer to apical foramen). Improved wall shear stress was observed for the more severely curved root canal.

Razumova et. Al [17] studied the quality of root canal therapy with change in geometry of the root canal. In their study, they utilized an optical microscope to obtain the geometry of the root canal, and this geometry is one of the most reliable geometries of the realistic root canal available in literature. The authors observed that among the 100 different samples of root canals collected, the irrigant failed to reach the apical third.

In the book "Grossman Endodontic practice", it is mentioned that the approximate intrapulpal pressure in the root canal is 10 mmHg [18]. It also mentions that reversible changes can occur if the pressure increases from 13 mmHg to 35 mmHg. However, if the pressure increases greater than that, it causes irreversible changes in the root canal geometry. This is critical as the threshold pressure must not exceed the limit which could cause the ligament to rupture, i.e., the apical pressure must be kept lower than 35 mmHg, and existing studies do not account for this. Table 1 gives a more convenient summary of the literature conducted for this thesis.

Table 1: Literature Review Summary

Year	**Author**	**Conclusion**
1984	John W. Harrison	Sodium Hypochlorite has been effective due to its antimicrobial property, most efficient necrotic tissue solvent and effective in removing organic debris.
2000	Hulsmann M, Hahn W., Germany	Sodium Hypochlorite should be well-handled for the prevention of mishappening to the patient and health worker.

Year	**Author**	**Conclusion**
2006	C. Boutsioukis , T. Lambrianidis, E. Kastrinakis & P. Bekiaroglou	Irrigant flow rate is an important factor for flow beyond needle. Finer needle created higher inter-barrel pressure. Syringe Irrigation is difficult to standardize.
2009	C. Boutsioukis, T. Lambrianidis, & E. Kastrinakis	Irrigant replacement was limited to 1-1.5 mm from the tip of the needle for all flowrates.
2009	C. Boutsioukis, B. Verhaagen, M. Versluis, E. Kastrinakis, L. W. M. van der Sluis	CFD is efficient in evaluation of root canal and is valid compared with the microscopic PIV and theoretical calculation. Offset of needle position had limited effect on flow pattern and velocity.
2010	Christor Boutsioukis, Bram Berhagen, Michel Versluis, Eleftherios Kastrinakis, Paul R. Wesselink and Lucas W.M van der Sluis.	Open ended needles are efficient in the replacement of irrigant but also create high apical pressure.
2010	Christos Boutsioukis, Theodor Lambrianidis, Bram Verhaagen, Michel Versluis, Eleftherios Kastrinakis, Paul R. Wesselink, and Lucas W.M. van der Sluis	Side vented replaced irrigant only when placed 1 mm from WL, open ended replaced when positioned at 2 mm. Apical pressure increased with increase in distance from WL. Shear stress decreased with the increase in distance from WL.
2010	C. Boutsioukis, C. Gogos, B. Verhaagen, M. Versluis, E.	Increase in root canal taper improved irrigant flow and wall shear stress. Also, increase in apical preparation size with minimally tapered size also had same effect.

Year	Author	Conclusion
	Kastrinakis, L. W. M van der Sluis	
2012	C. Boutiouskis, Z. Psimma & L.W.M van der Sluis	Review article (inconclusive study due to methodological limitation) - not simulating the preapical tissue - need to be investigated in future.
2014	Zeya Quadri, Kyaw Zeya, Mohammad Faisal	Upper jaws teeth require more velocity.
2017	E. Konstantinidi, Z. Psimma, L. E. Chavez de Paz & C. Boutsioukis	Not enough relevant data to claim the superiority of negative or positive irrigation methods.
2021	Kavalipurapu V. Geja, Sindhu Ramesh, Kaligotla A. Vasundhara, K.C. Janani, Jerry Jose, Gopi Battineni	Preliminary automated system for irrigation of needle designed.
2022	Na Zhou, Zhengqiu Huang, Mingzhou Yu, Shuli Deng, Baiping Fu, and Hanhui Jin	Lower positioning of needle towards the working length had positive impact on efficiency.

Chapter 3 Methodology

The numerical study was conducted using ANSYS FLUENT R22. First, the study was conducted using a simplified root canal geometry, which is an inverted frustum of a cone. This step was necessary to validate the numerical setup since most studies in the literature were done with simplified geometry. The solution sequence includes creating and importing the CAD model, generating the appropriate mesh, setting up the solver, and post processing. The said steps are discussed in more detail below.

3.1 CAD Model

The geometry of the simplified root canal was obtained from a study conducted by Boutsiouskis et al. [11]. This geometry is utilized for validation and further experimentation in the simplified root canal to establish baseline data for comparison purposes. The 3D-model of the root canal and needle was created in SolidWorks 2022. The length of root canal is 19 mm, while the apical diameter is 0.45 mm resulting in a 6% taper. The constriction of the apical foramen is considered to be 0.3 mm which extends 0.5 mm below where the diameter broadens to 0.36 mm. Associated dimensions are given in Fig. 5.

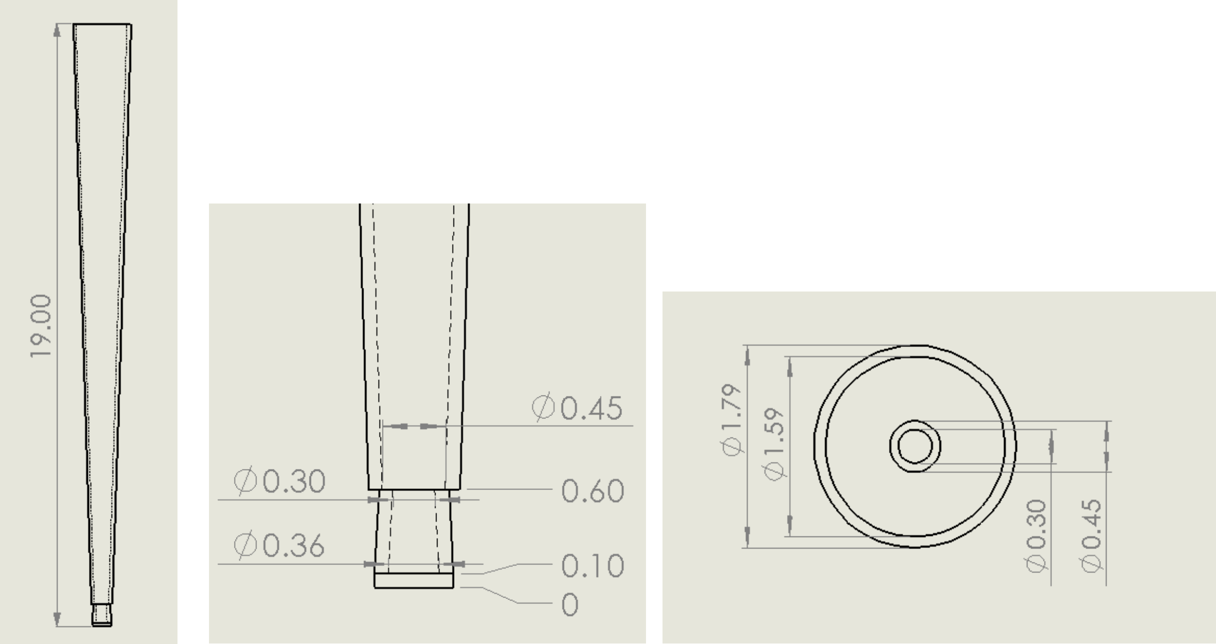

Figure 5: Detailed Drawing of Simplified root canal

The side vented needle was selected for this study as it has been widely utilized in literature. The reason for extensive use of this particular needle is due to its enhanced safety as there is no sharp edge at the bottom which could hurt tissues during the irrigation process Moreover, the fluid doesn't directly flow into the root canal apex unlike the flat bottom needle. The side ejection of the fluid prevents extrusion of the root canal apex, which is the major concern for dentists. The dimensions of the 30G needle were also obtained from Boutsiouskis et al. [11]. The length of the needle is 31 mm, while the external and internal diameters are 320 µm and 196 µm, respectively. The detailed cut dimension is shown in Fig. 6 below. The same needle geometry is used for both the root canal studies: the simplified and realistic root canals.

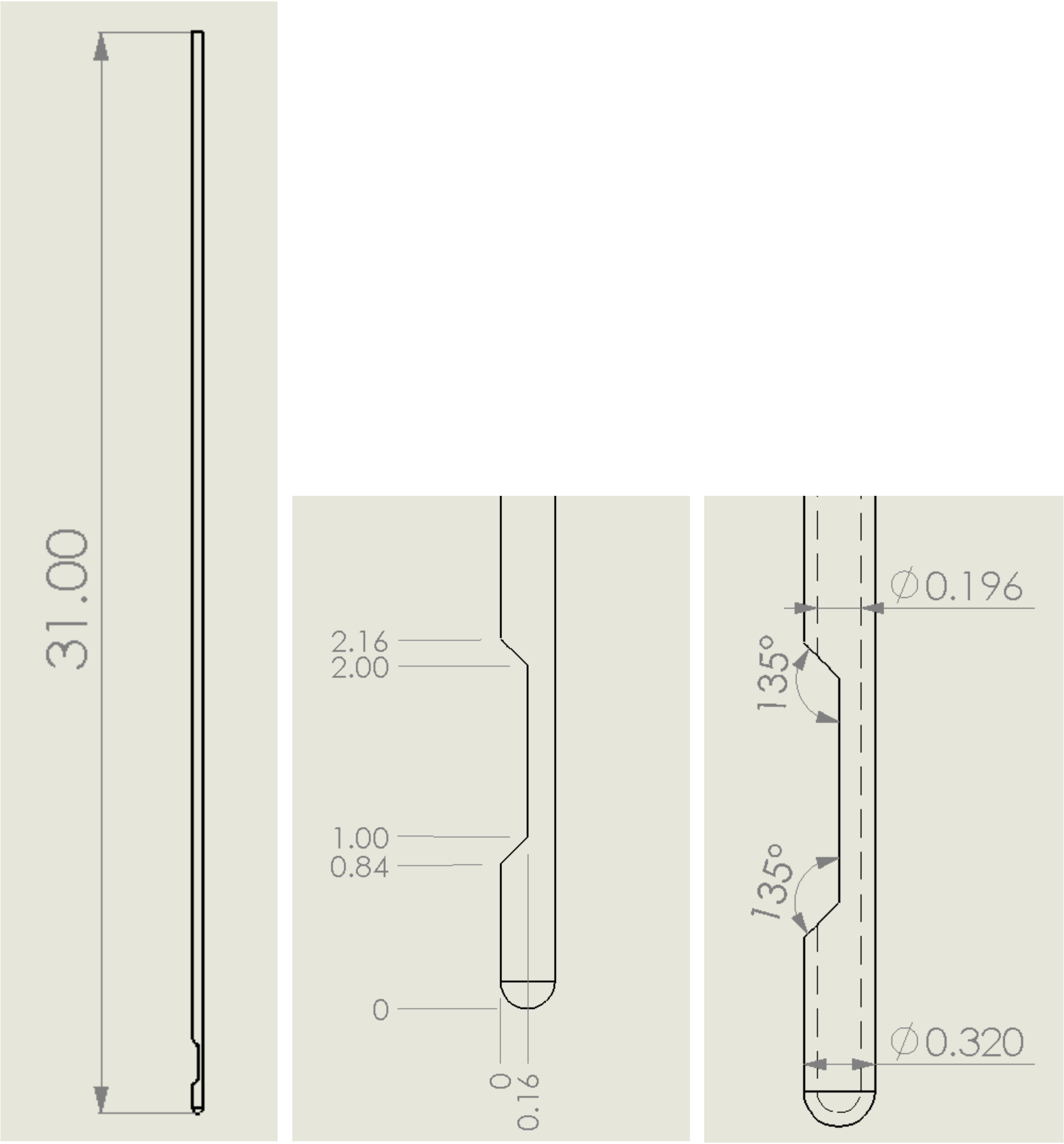

Figure 6: Detail drawing of 30G needle

The more realistic root canal geometry was created based on dimensions provided by Razumova et al. [17]; they obtained the dimensions using an optical microscope. Figure 7 below shows the realistic geometry of the prepared root canal. The assembly file was created using the part model in SolidWorks, saved as a Parasolid file (.x_b) and then imported into ANSYS

Workbench 2022 R2. Figures 8 and 9 illustrate the side vented needle inside the simplified and realistic (complex) root canal geometries, respectively.

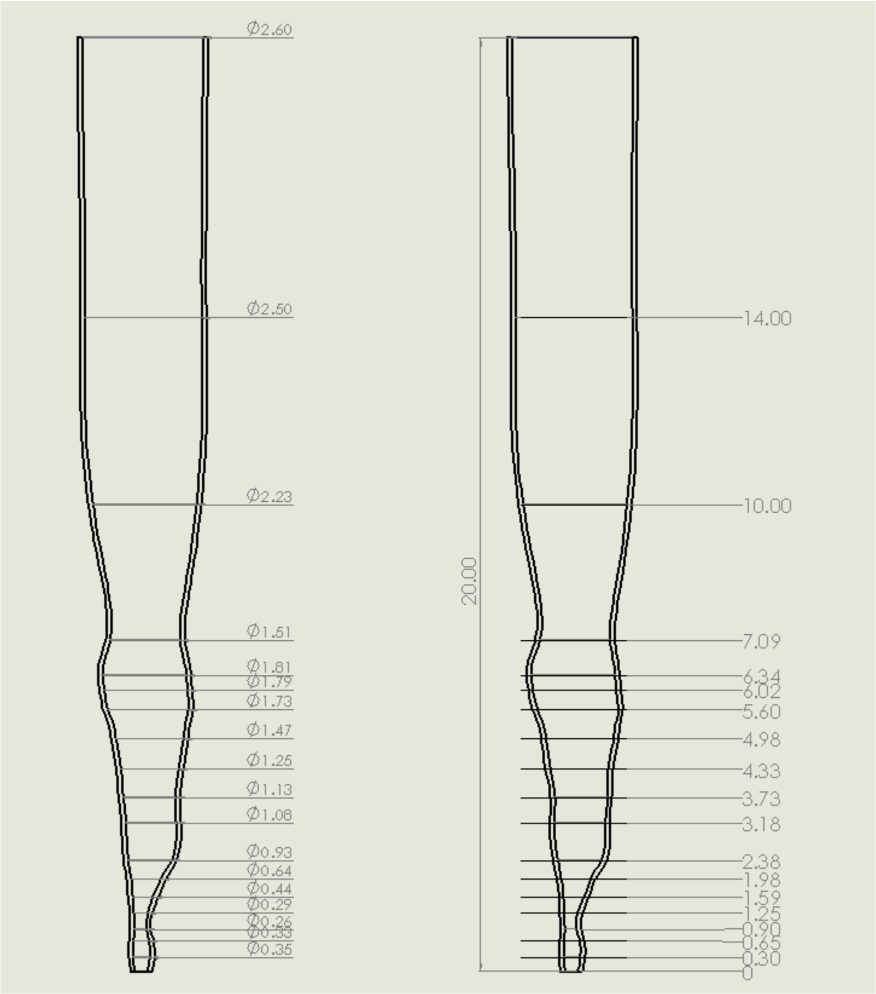

Figure 7: Detail drawing of realistic root canal

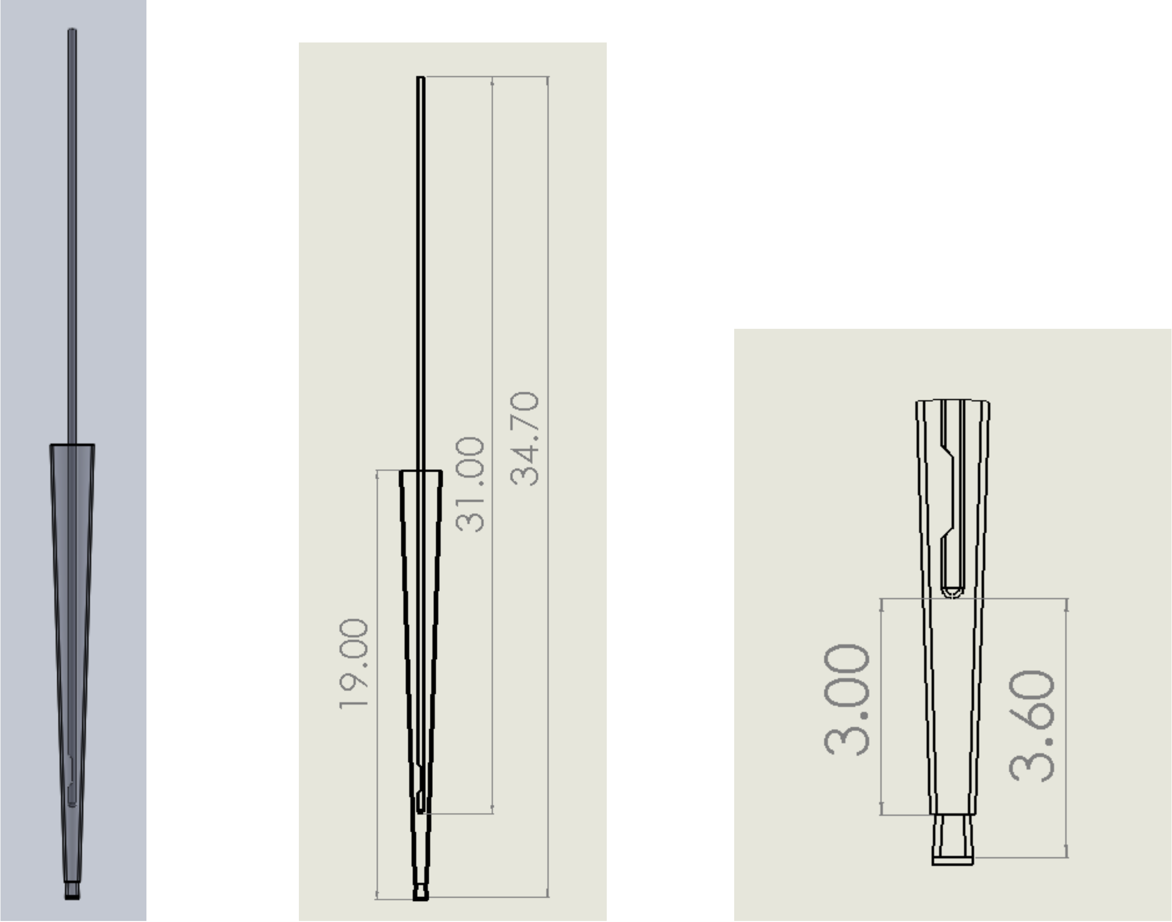

Figure 8: Assembly of simplified root canal and needle

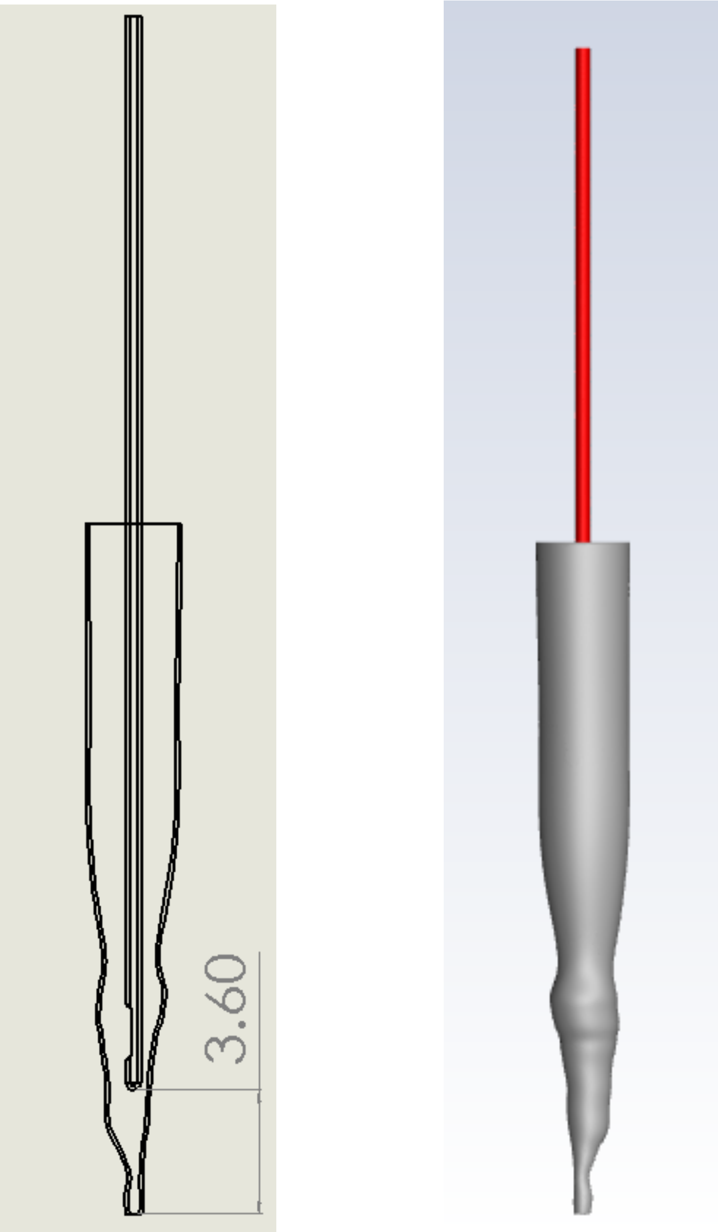

Figure 9: Assembly of realistic root canal and needle

Following the CAD creation, the geometry is then exported to ANSYS Design modeler. The fluid is filled inside the needle and root canal, and then Boolean function is used to combine the fluid of root canal and needle and subtract the needle region from the combined fluid. Once these operations are done, the geometry is ready for the meshing process.

3.2 Meshing and Boundary Conditions

The maximum element size was 0.01794 mm. In addition, inflation layers were added to the interface of the root canal wall and fluid located within the root canal fluid domain. The number of inflation layers was 5, the transition ratio to was 0.1, and the growth rate was 1.05. The body sizing function was used to refine the mesh at the region where needle ejects the fluid. This resulted in the total number of cells varying between 996,345 and 1,011,886 (variation due to change in needle insertion depth and tilt angle) for the simplified geometry and between 1,167,234 and 1,213,009 for the realistic geometry. The aforementioned numbers represent the optimum mesh density that was obtained via a grid independence study. Various mesh densities were considered, and the final cell count was identified when the results for maximum velocity did not change by more than 2%. Figure 10 shows the detailed mesh for the simplified root canal, while Fig. 11 shows the detailed mesh for the more complex countertype.

As for boundary conditions, the top face of the needle is set as inlet velocity boundary type while the top face of root canal is set to pressure outlet boundary condition. The rest of the faces are considered to be no-slip walls. Depending on the flow rate studied, the needle inlet velocity was varied within the simulation. Figure 12 highlights the location of the velocity inlet and pressure outlet boundary conditions.

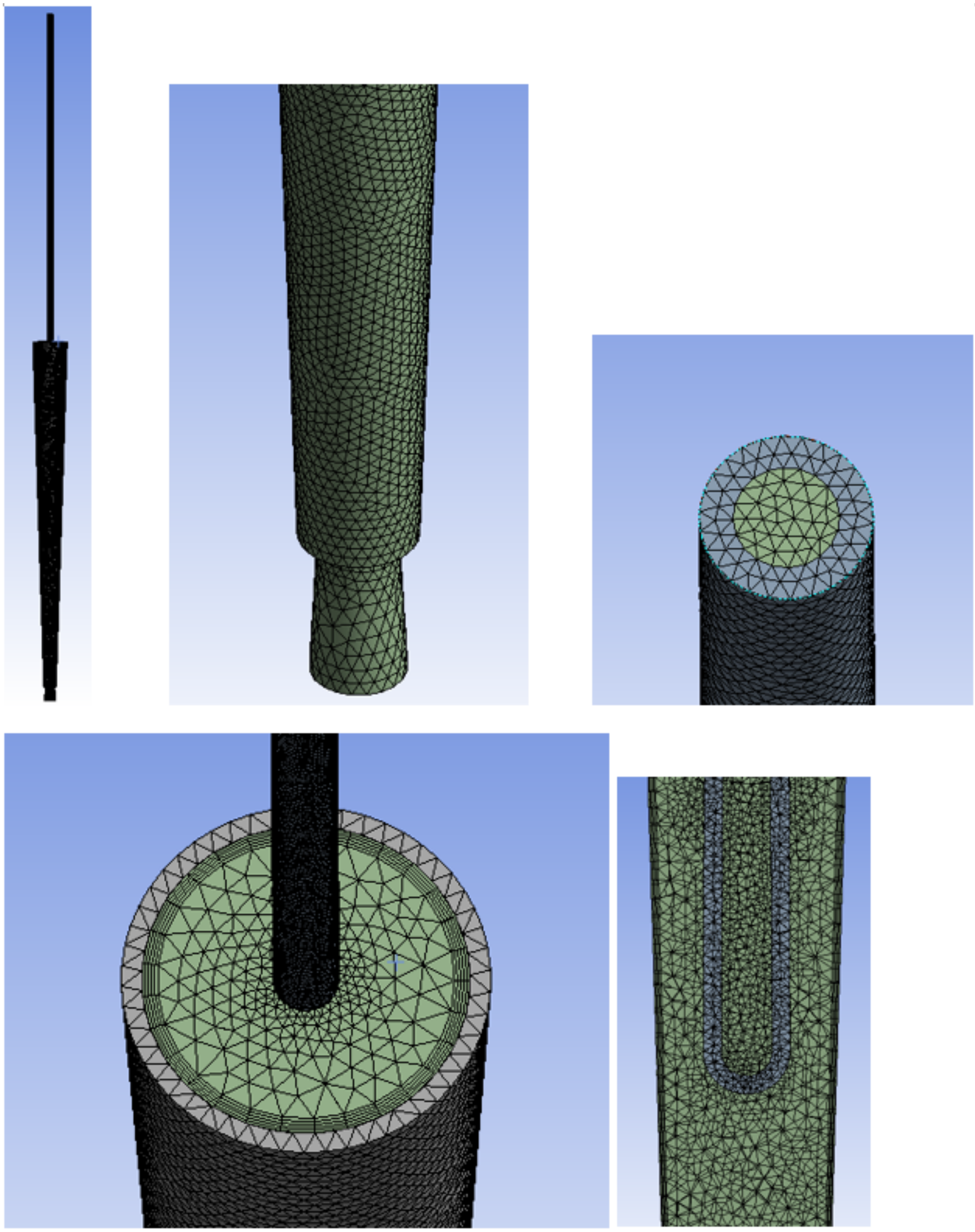

Figure 10: Simplified root canal mesh

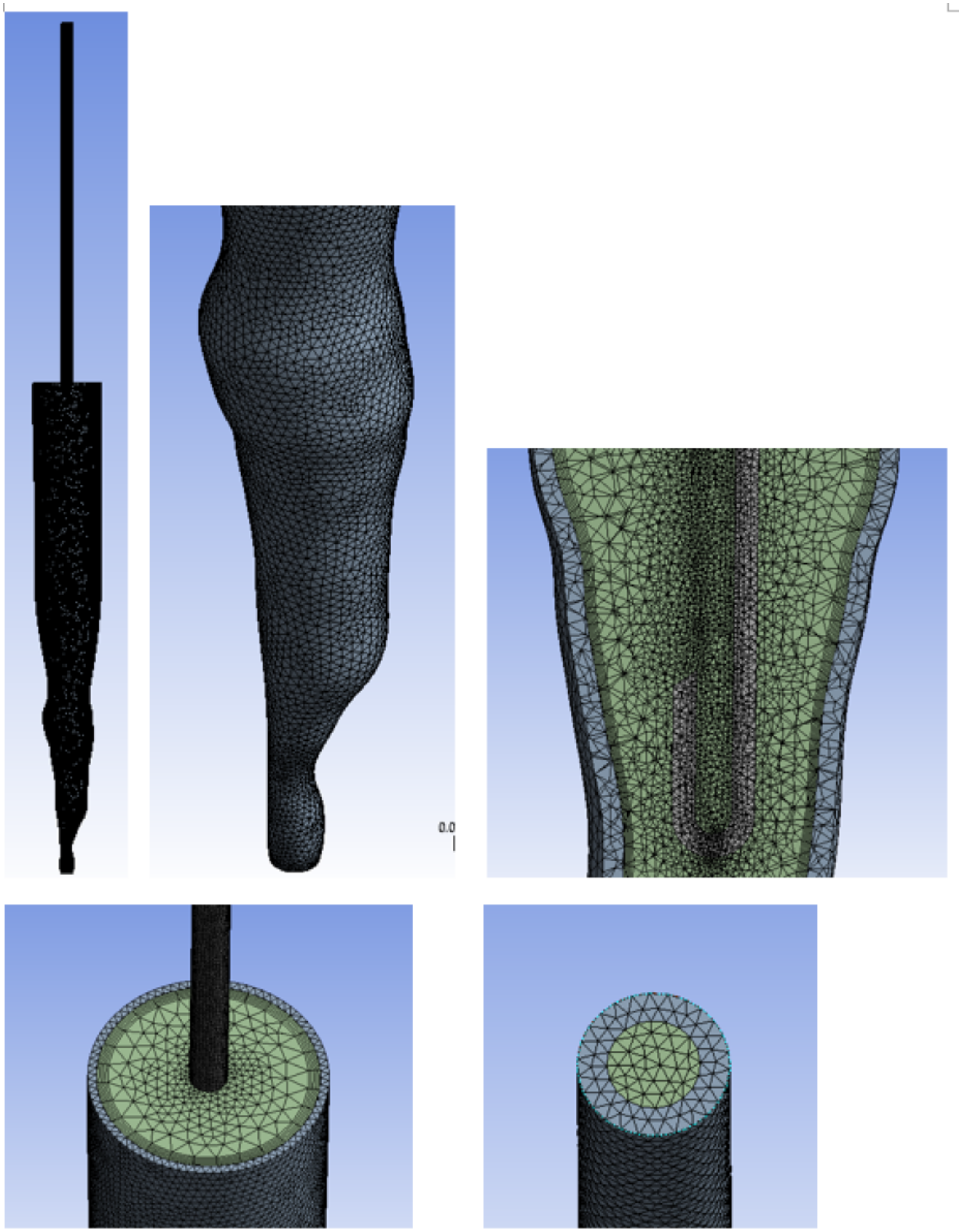

Figure 11: Realistic root canal assembly mesh

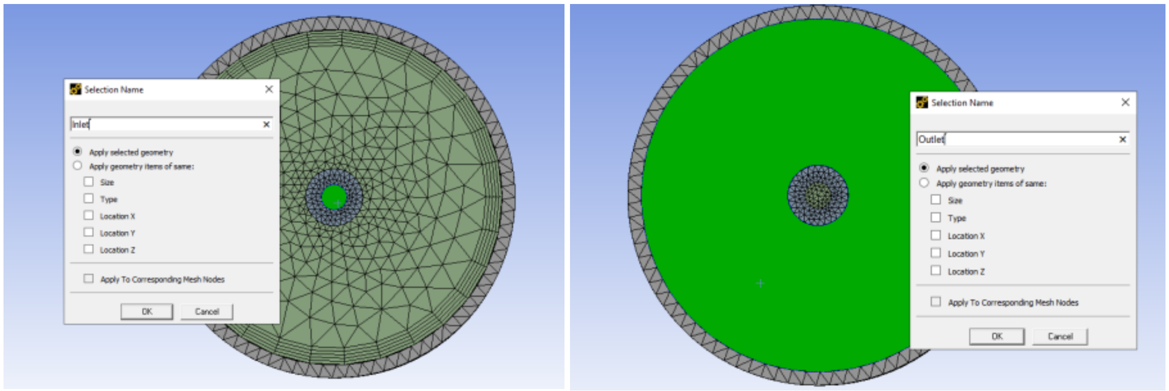

Figure 12: Specifying the name for inlet and outlet in mesh.

3.3 Numerical Setup

The flow was considered to be unsteady, three dimensional, incompressible, isothermal, and turbulent. Gravity was turned on in the y-direction. The standard k-epsilon turbulent model was selected so that the simulation parameters were consistent with Boutsiouskis et al. [11]. While water was selected as the fluid, the fluid viscosity and density were changed to match that of Sodium hypochlorite, i.e., fluid density was 1040 kg/m3 and fluid absolute/dynamic viscosity was 0.00099 Pa.s. The inlet velocities were changed depending on simulation type, while the pressure outlet domain was always zero-gauge pressure. The convergence was set to 1×10^{-6}, and the coupled solver (pressure-velocity) was selected. The total simulation time was 50 milliseconds with a time step of 0.00023s.

3.4 Post Processing

A mid-plane was created which was parallel to the cut of the needle to have clear visualization of the flow leaving the needle (see Fig. 13). To capture the apical pressure, a point is created 0.25 mm from the bottom of the root canal. The area-weighted average and facet maxima option is selected for obtaining wall shear stress and apical pressure. The contour of velocity and turbulent intensity are plotted in the midplane. The wall shear stress is plotted at the interface between fluid and root canal wall. Moreover, the streamline is plotted starting from the inlet and a scene is created showing the needle, transparent root canal and the streamline starting from inlet. Finally, vectors are also plotted in the mid-plane to see the distribution of the fluid particles inside the root canal.

Chapter 4 Results and Discussion

The results obtained for the initial validation of the model are discussed, followed by results for the simplified root canal and more realistic root canal. The comparison between the two different root canal geometries is done at last.

4.1 Validation of the Model

The numerical setup is verified with the study conducted by Boutsioukis et al. [11]. The simplified root canal geometry is considered, while the needle type was a side vented one (see CAD Model section for dimensions of root canal and needle). For the validation study, the needle is considered to be 3mm short of working length. This means that the needle was kept at a distance of 3 mm from the apical constriction, which is 3.5 mm from the bottom of the root canal.

Flow pattern, maximum velocity, and apical pressure were considered as the output parameters for validating the simulation. The velocity contour is utilized to obtain the maximum velocity in the root canal as shown in Fig. 13. The maximum velocity was found to be close to that reported by Boutsioukis et al. [11]; 13 m/s for current study vs. 11.8 m/s from literature.

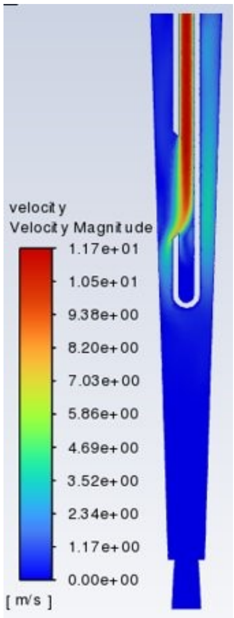

Figure 13:Velocity contour for validation

In addition, the streamline plot obtained in this study (Fig. 14) was comparable to that obtained by Boutsioskis [11]. For this, a scene was created where the needle (red color), root canal (transparent gray), and streamlines were plotted to observe the flow pattern which was similar to that shown in the literature. A point was also created at the bottom of the root canal at a distance of 0.25 mm from the bottom. The pressure is obtained from the surface integral feature utilizing the area-weighted average of the static pressure. The apical pressure was also found to be comparable to the value provided by Boutsioukis et al. [11]; 8.7 KPa (current study) vs. 9.5 KPa. Interestingly, the maximum velocity and apical pressure were below their respective values reported in the literature. One major reason could be the mesh. The current study employed a mesh which was much more refined than that found in [11].

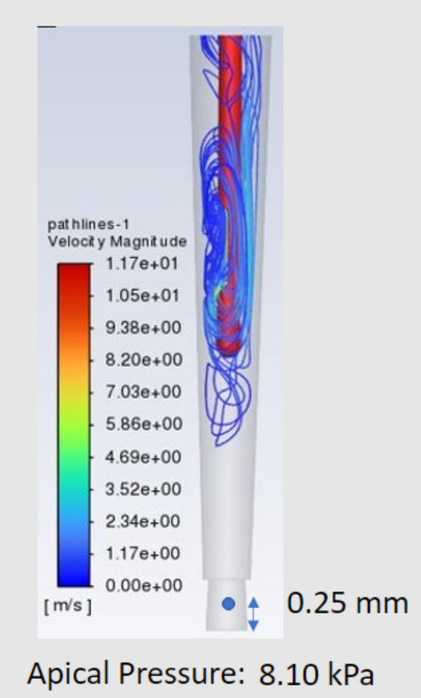

Figure 14: Streamline Scene for validation of flow pattern

Once the validation was performed, the simulations were then conducted using simplified geometry to obtain baseline data and trends. The process parameters of interest were fluid inlet velocity, needle insertion depth, needle tilt angle. The irrigant flow rates considered were 0.181 mL/s, 0.26 mL/s, and 0.36 mL/s, and this translates to fluid inlet velocity of 6 m/s, 8.6 m/s, and 12 m/s, respectively [2]. The irrigant flow rate of 0.26 mL/s is considered to be a clinically realistic fluid flow rate in the irrigation of a root canal [11]. Needle insertion depth of 1 mm, 2 mm, and 3 mm short of the working length were considered, and needle tilt angles of 1° and 2° clockwise and anticlockwise were also considered. The aforementioned process parameter values were kept the same for the simulation in the realistic root canal geometry as well.

To investigate the irrigation efficacy, the following output parameters were considered: flow pattern, maximum velocity, wall shear stress, apical pressure, and penetration depth. The flow pattern is observed using a streamline plot of the flow within the needle and root canal. The maximum velocity is obtained from the velocity contour on the mid-plane, while the wall shear stress is determined from the contact region between the fluid and root canal interface. More information on how the values were determined is provided in the “Post Processing” section. The penetration depth is considered to be the distance between lowest point on the streamline and the bottom of the needle.

The detailed results are presented in the following order. First, the effect on flow characteristics due to variation of irrigant flow rate, needle insertion depth, and needle tilt angle are studied for the simplified root canal geometry. Next, the same study is repeated but for the more realistic root canal geometry instead. Subsequently, the comparison between the two root canal geometries is examined to understand differences and select the optimal combination of process parameters.

Finally, the standard side vented needle is modified to improve irrigant flow characteristics within the more realistic root canal for the optimal combination identified previously.

4.2 Simplified root canal

The effect of variation in flow rate, needle depth and needle tilt angle for the simplified root canal are discussed in this section. The results are discussed based on the velocity contour, wall shear stress contour, penetration depth, flow pattern, apical pressure, turbulent intensity contour, and vector plot for different input process parameters.

4.2.1 Variation of Flow rate:

Three different flow rates were considered: 0.181 mL/s, 0.26 mL/s, and 0.36 mL/s which translate to fluid inlet velocities of 6 m/s, 8.6 m/s and 12 m/s, respectively. Since 0.26 mL/s is considered as the clinically realistic flow rate, one above the value (0.36 mL/s) and one below (0.181 mL/s) are considered for the simulation. The needle is kept at 3 mm short of working length, centered within the root canal for each experiment. It was observed that with the increase in fluid inlet velocity, the maximum velocity increased almost linearly. This was expected as the fluid was falling under the influence of gravity. The maximum velocity was 8.38 m/s for fluid inlet velocity of 6 m/s, 11.7 m/s for inlet velocity of 8.6 m/s, and 16 m/s for inlet velocity of 12 m/s. As an example, the velocity contour for the 8.6 m/s case is shown below in Fig. 15. The contours for the other two simulation cases are given in the appendix; the same trend is followed for the other results that are discussed below.

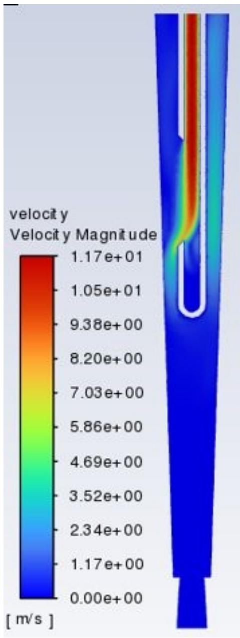

Figure 15: Velocity Contour for 8.6 m/s inlet velocity for simplified geometry

Similarly, the flow pattern for each of the simulations was also obtained. Figure 16 shows the flow pattern for inlet velocity of 8.6 m/s via a streamline plot. The flow penetration depth is obtained by creating the plane at the lowest point of the curve of the streamline. Then, the distance between the bottom of the needle and this plane is measured to obtain the penetration depth. For an inlet velocity of 8.6 m/s, the penetration depth was 1.65 mm. As the inlet flow increases, it is interesting to note that the penetration depth also increases but not in a linear fashion.

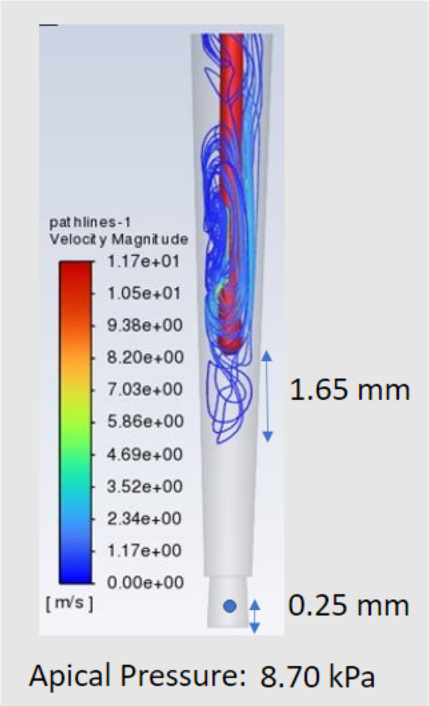

Figure 16: Streamline Scene with penetration depth and apical pressure for inlet velocity of 8.6 m/s for simplified geometry

The apical pressure is obtained at a distance of 0.25 mm from the bottom of root canal. The area weighted averaged for an inlet velocity of 8.6 m/s was 8.7 KPa. With the increase in flow velocity, the apical pressure seems to be increasing linearly for the three velocities considered in this study. Of particular interest is the turbulent intensity, a measure of swirl, which was plotted on the midplane contour. The turbulent intensity maximum value and distribution along the midplane for fluid inlet velocity of 8.6 m/s is shown in Fig. 17 below.

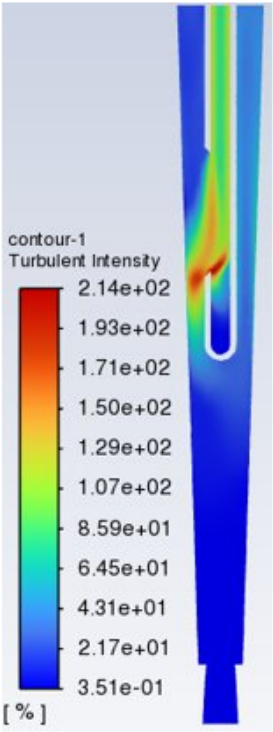

Figure 17: Turbulence intensity at 8.6 m/s for simplified geometry

The wall shear contour was obtained to examine the stress distribution on the wall of the root canal when the fluid is ejected from the needle. Figure 18 below shows the root canal wall shear stress distribution as a result of the fluid striking the root canal for 8.6 m/s fluid inlet velocity. Moreover, the maximum wall shear stress and area-weighted average values are also extracted for comparison purposes discussed later on in this report.

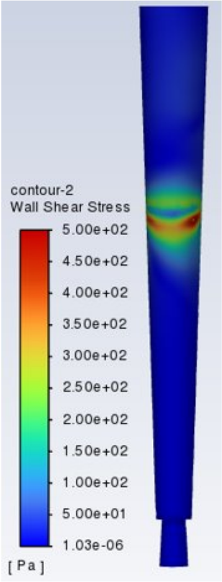

Figure 18: Wall shear stress contour at 8.6 m/s for simplified geometry

The velocity vector plot is also obtained to see the swirl and orientation of the fluid coming out of the needle. Figure 19 below shows the velocity vector plot for 8.6 m/s. There is swirl in the fluid just below the needle; two vortices: upper large one and lower smaller one can be seen from the vector plot. As the inlet fluid velocity increased, the vortices also increased.

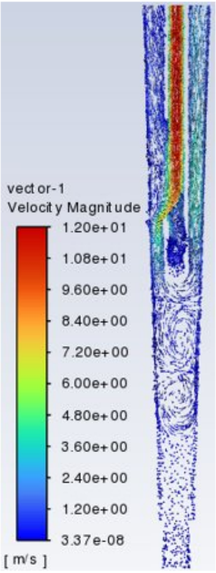

Figure 19: Vector plot at 8.6 m/s for simplified geometry

Table 2 provides the output parameters and how their values vary with change in irrigant flow rate. It can be seen that as the inlet speed increases, the apical pressure, penetration depth, wall shear stress, maximum velocity, and maximum turbulent intensity are all increasing. However, not all increases are linear, and this is discussed in detail further along the report.

Table 2: Effect of Variation of Speed

Variation of Speed (m/s)	Apical pressure (Pa)	Penetration depth (mm)	Flow Penetration Depth (mm)	Wall Shear Stress (Pa)	Maximum Velocity (m/s)	Maximum Turbulent Intensity (%)	Area Weighted Shear Stress (Pa)
6.00	4494.63	0.77	2.83	242.47	8.38	152.00	9.00
8.60	8743.07	1.65	1.95	562.03	11.70	214.00	16.94
12.00	16119.07	1.70	1.90	1121.64	16.00	298.00	27.81

4.2.2 Needle Insertion Depth

Needle insertion depth here represents the position of needle short of working length. Working length is the distance from the top of the canal to the point at the apical region where the preparation of the root canal terminates. In this study, the needle working length is considered to be 18.4 mm, which is the distance measured from the root canal opening to the apical constriction. The region below the apical constriction is called the apical foramen. Therefore, a needle depth of 1 mm indicates that the needle is placed at a distance of 1 mm from the constriction which translates to 17.4 mm measured from the top of the root canal. Similarly, the needle depth of 2 mm indicates that the needle is placed 2 mm from the apical constriction or 16.4 mm from the top of the root canal. Hence, the smaller the needle insertion depth, the deeper the needle is inserted into the root canal (i.e., closer to the apical foramen). Three different needle insertion depths of 1 mm, 2 mm, and 3 mm were considered for this study. For all three different simulation cases, the irrigant inlet velocity was held constant at 8.6 m/s.

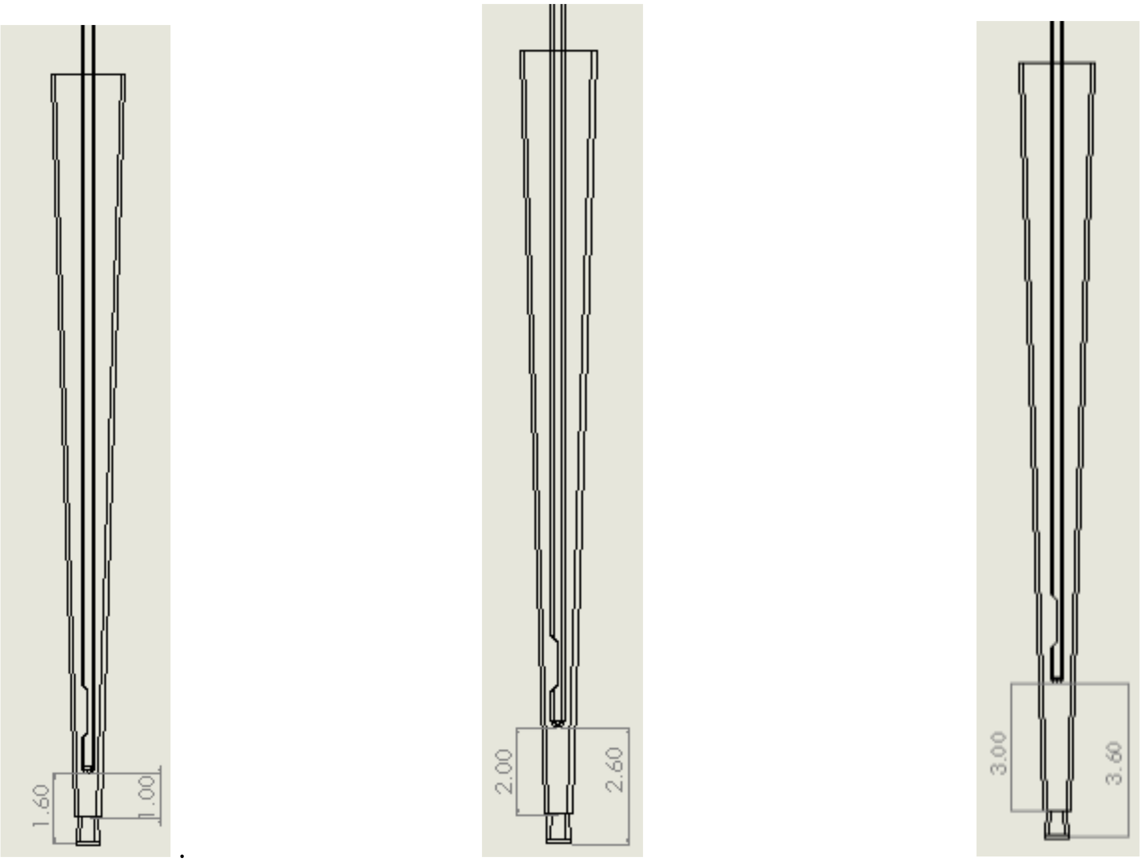

Figure 20: Needle insertion depth variations of 1mm (left), 2mm (center), and 3 mm (right).

As a representation, the velocity contour at mid-plane for needle insertion depth of 2 mm is given below in Fig. 21. Irrespective of the insertion depth, the maximum velocity remained constant. The flow penetration depth increased as the needle insertion depth increased from 1 mm to 3 mm, i.e., as the needle moved away from the apical foramen, the irrigant displayed better penetration within the root canal. For example, at a needle insertion depth of 2 mm, the flow penetration depth (distance between streamline end and bottom of needle) was 1.161 mm (see Fig. 22). It must be noted that a larger flow penetration depth doesn't necessarily indicate irrigant going deeper into the root canal. The other numerical values are provided in Table 3 for comparison purposes.

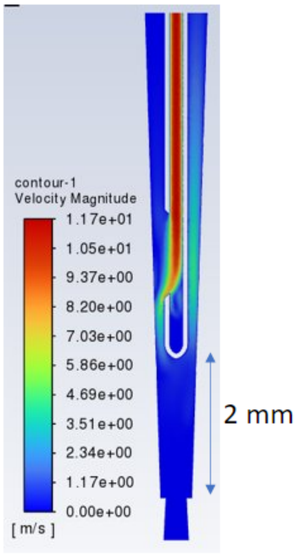

Figure 21: Velocity contour for needle insertion depth of 2 mm

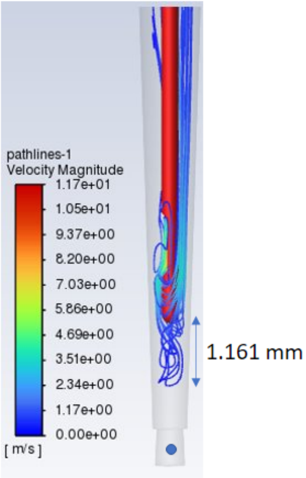

Apical Pressure: 11.64 kPa

Needle Depth: 2 mm

Figure 22: Streamline plot and apical pressure for needle insertion depth of 2mm

The wall shear stress trend was not as expected. It was anticipated that as the needle insertion depth increased (needle moves away from apical foramen), the maximum wall shear stress would decrease since the wall area increases. While the maximum wall shear stress for 1 mm insertion depth was higher than a 2 mm or 3 mm insertion depth, interestingly, the maximum wall shear stress for 2 mm was lower than that for 3 mm (reverse trend). Figure 23 shows the wall shear stress distribution for an insertion depth of 2 mm. With that said, the area weighted average wall shear stress decreased as needle insertion depth increased, and this was as anticipated. The contours showing the distribution of the other insertion depths can be found in the appendix. As expected, the apical pressure appeared to decrease as insertion depth increased.

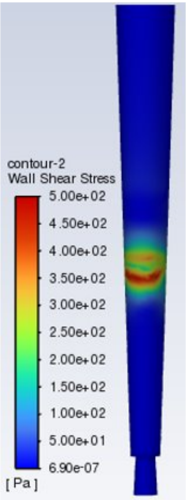

Needle Depth: 2 mm

Figure 23: Wall shear stress contour for needle insertion depth of 2 mm

Finally, the turbulent intensity contour was plotted on the mid-plane contour to examine local turbulence strength and swirl. The highest value for the turbulent intensity was observed for 3 mm needle insertion depth. Even though the turbulent intensity did decrease for higher insertion depths, for the 1 mm and 2 mm configurations, it was found to have similar values.

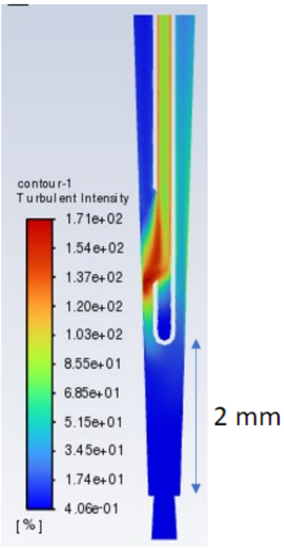

Needle Depth: 2 mm

Figure 24: Turbulent intensity for needle insertion depth of 2 mm

All numerical results are provided in Table 3 for quick comparison.

Table 3: Flow characteristics for various Needle Insertion Depth

Needle Depth (mm)	Apical pressure (Pa)	Penetration depth (mm)	Flow Penetration Depth (mm)	Wall Shear Stress (Pa)	Maximum Velocity (m/s)	Maximum Turbulent Intensity (%)	Area Weighted Shear Stress (Pa)
1.00	14344.03	0.37	1.23	607.79	11.70	173.00	19.64
2.00	11649.57	1.16	1.44	550.24	11.70	171.00	18.26
3.00	8743.07	1.65	1.95	562.03	11.70	214.00	16.94

4.2.3 Variation of Needle Tilt Angle

To study the effect of needle tilt angle, the needle penetration depth was kept constant at 3 mm, and the needle subsequently tilted 1° and 2° both in the clockwise and counterclockwise directions to observe the effect on the flow characteristics. The notch of the needle constantly faced the left side of the root canal wall; however, the angle varied in the clockwise or counterclockwise direction with the needle pivoting about its end. Figure 25 shows the investigated orientations.

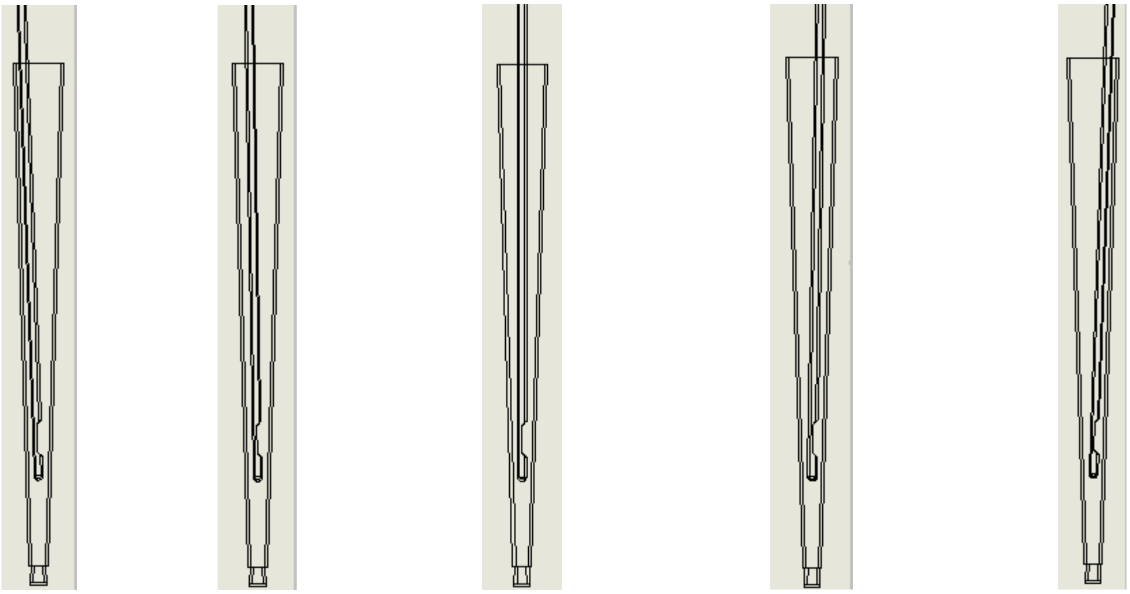

Figure 25: Tilt angle with sequence of 2° counterclockwise, 1° counterclockwise, 0°, 1° clockwise and 2° clockwise from left to right.

The velocity contour (Fig. 26) is plotted in the mid-plane which makes the tilt of the needle clearly visible. It was observed that for all the needle tilt angles, the maximum velocity was rather unchanged. Figure 27 shows the streamline for a needle tilted 2° counterclockwise (CCW). The observed flow penetration depth was 1.08 mm with an apical pressure of 8.4 kPa. The maximum flow penetration depth was found to be for the 1° clockwise (CW) configuration of the needle. The 2° CCW tilt also resulted in the lowest apical pressure, while the highest value observed was for the 1° clockwise configuration.

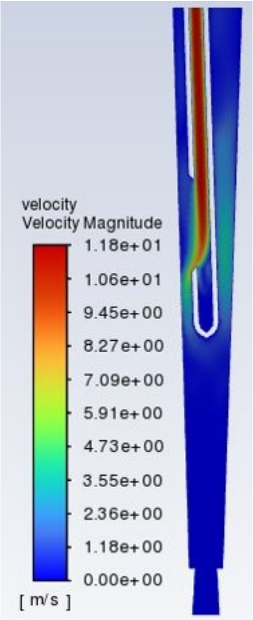

Figure 26: Velocity contour for needle tilt of 2° counterclockwise

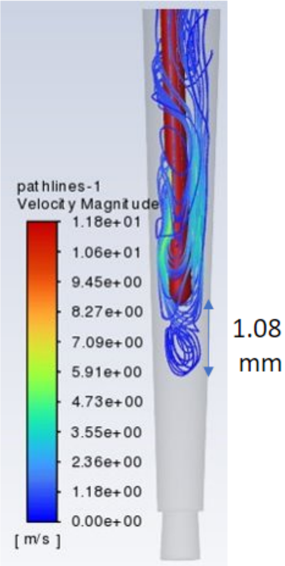

Apical Pressure: 8.4 kPa

Needle Tilt: 2^0 CCW

Figure 27: Streamline scene showing apical pressure and penetration depth for needle tilt of 2° counterclockwise.

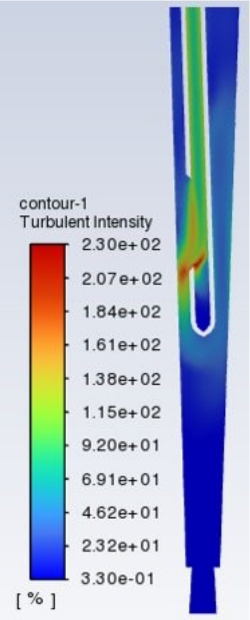

Figure 28: Turbulent intensity for 2° counterclockwise direction

Figure 28 shows the turbulent intensity contour which was also plotted in the mid-plane. As the needle tilted from CW to CCW, the maximum turbulent intensity increased to a maximum value of 230 indicating that the 2° CCW had the best swirl.

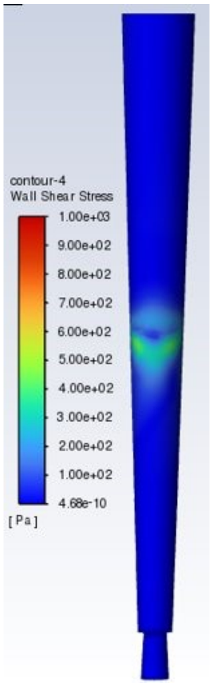

Figure 29: Wall stress contour for 2° counterclockwise rotations of needle

Figure 29 provides the wall shear stress distribution on the root canal wall when the needle is tilted to 2° CCW. In general, when the needle was tilted in the CCW orientations, the maximum wall shear stress was higher. This was expected as for CCW configurations, the needle exit was directly pointed at the root canal wall resulting in more direct impact. The lowest shear stress was when the tilt was absent. Despite this maximum shear stress trend, the average shear stress was highest for the CW orientations.

Table 4: Flow characteristics for various tilt angle

Tilt Angle	Apical pressure (Pa)	Penetration depth (mm)	Flow penetration depth (mm)	Wall Shear Stress (Pa)	Maximum Velocity (m/s)	Maximum Turbulent Intensity (%)	Area Weighted Shear Stress (Pa)
2 CW	9192.18	1.40	2.21	650.54	11.80	217.00	17.35
1 CW	9348.41	1.81	1.80	608.17	11.80	221.00	18.36
0 Tilt	8743.07	1.65	1.96	562.03	11.80	214.00	16.94
1 CCW	8584.73	0.79	2.82	641.46	11.80	228.00	17.08
2 CCW	8446.18	1.08	2.53	854.10	11.80	230.00	17.16

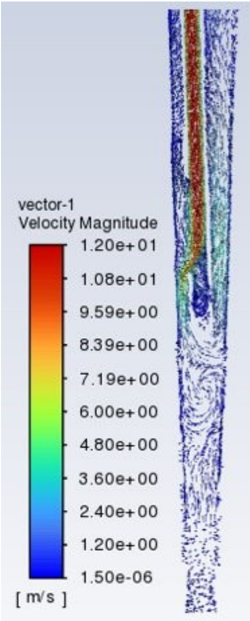

Figure 30: Vector plot for 2° counterclockwise rotations of needle

The vector plot in Fig. 30 depicts the flow coming out from the needle to the root canal. There is a vortex forming right below the needle as the fluid comes out which could help with swirl and removal of necrotic tissues.

4.3 Realistic Root Canal

The needle is kept concentric to the apical constriction of the root canal and simulation is performed for various input parameters: variation of fluid inlet velocity, variation of needle depth and variation of needle tilt angle. The results of the simulation are discussed based on the velocity contour, turbulent intensity contour, wall shear stress contour, penetration depth, flow pattern, and apical pressure.

4.3.1 Variation of Flow Rate

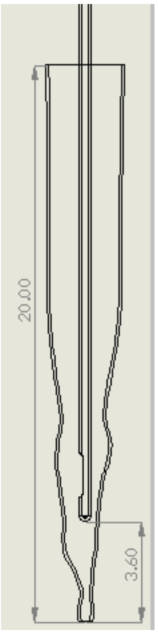

Figure 31: Needle and root canal configuration for variation of speed

The same flow rates used during the simplified root canal study of 0.181 mL/s, 0.25 mL/s, and 0.36 mL/s are considered for the inlet flow which are equivalent to the velocity of 6 m/s, 8.6 m/s and 12 m/s, respectively. For all the configurations, the needle is kept at the distance of 3.6 mm from the bottom of the root canal to have similar distance as that of the simplified root canal.

The figure below shows the plot for the velocity contour in the realistic root canal for the fluid inlet velocity of 8.6 m/s. The maximum velocity of the fluid inside the root canal is observed to be 11.7 m/s. With an increase in irrigant flow speed, the maximum velocity observed increased as well.

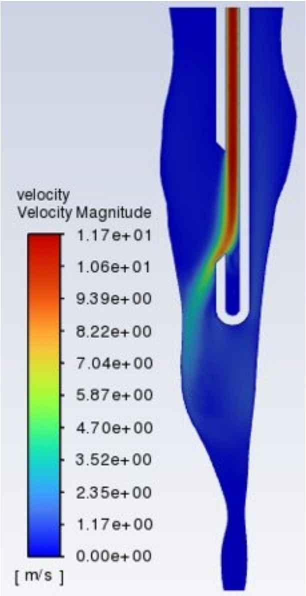

Figure 32: Velocity contour for inlet fluid velocity of 8.6 m/s

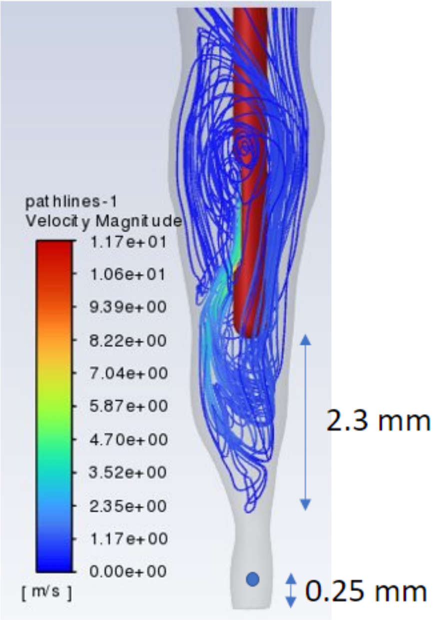

Figure 33: Streamline scene with apical pressure and penetration Depth for 8.6 m/s

The streamline plot shows a flow penetration depth of 2.3 mm for this simulation trial, while the apical pressure was 2826.27 Pa. At the highest irrigant inlet flow velocity of 12 m/s, the flow penetration depth and apical pressure were the highest as well, i.e., both parameters increased with flow rate. The turbulent intensity contour shows a more pronounced swirl in the apical third when compared to the simplified root canal geometry. A more detailed comparison between the two root canals is provided later in the report. As the flow velocity increased, the maximum turbulent intensity also increased.

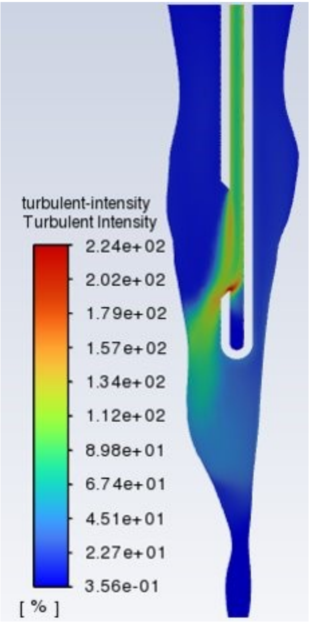

Figure 34: Turbulent Intensity contour for 8.6 m/s

The wall shear stress contour for the case of irrigant inlet flow of 8.6 m/s is shown in Fig. 35. The distribution shows a marked difference when compared to the simplified root canal. As the inlet irrigant flow velocity increased, both the maximum wall shear stress value and the average wall shear stress value increased. The values for the three different velocity trials are given in Table 5.

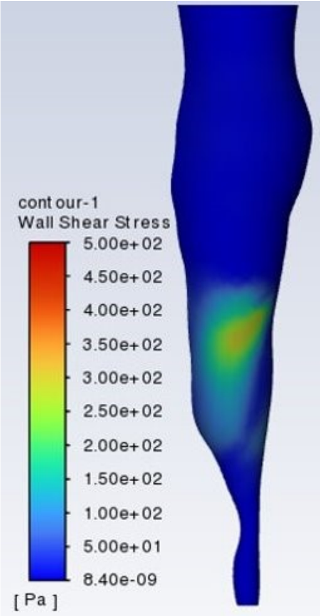

Figure 35: Wall Shear Stress for fluid inlet velocity of 8.6 m/s

The figure below shows the vector plot in the mid-plane of the realistic root canal for irrigant inlet velocity of 8.6 m/s. There are two vortices visible: a larger one immediately below the needle and a smaller one above the apical foramen.

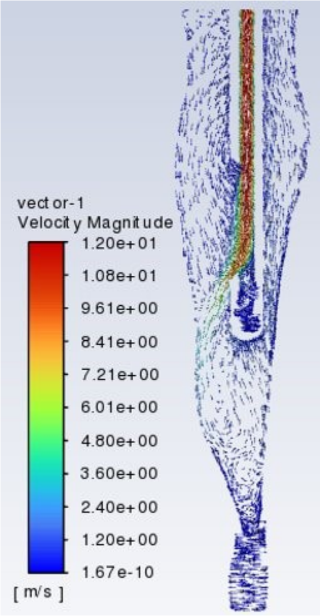

Figure 36: Vector plot for fluid inlet velocity 8.6 m/s

Table 5: Flow characteristics for variation of speed

Variation of Speed (m/s)	Apical pressure (Pa)	Penetration depth (mm)	Distance from bottom of root canal	Wall Shear Stress (Pa)	Maximum Velocity (m/s)	Maximum Turbulent Intensity (%)	Area Weighted Shear Stress (Pa)
6.00	1354.86	1.90	1.71	165.46	8.38	156.00	3.66
8.60	2836.27	2.30	1.31	333.71	11.70	214.00	7.10
12.00	5591.46	2.32	1.29	626.13	16.00	302.00	12.66

In short, with the increase in irrigant inlet velocity, the apical pressure, flow penetration depth, maximum wall shear stress, turbulent intensity, and average wall shear stress increased.

4.3.2 Variation of Needle Depth

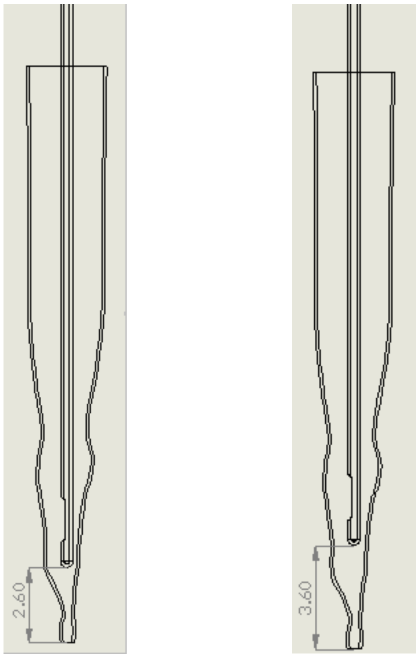

Figure 37: Configuration of the needle and root canal for 2 mm and 3 mm needle depth

To study the effect of varying needle insertion depth, only insertion depths of 2 mm and 3 mm were considered for the realistic root canal. For an insertion depth of 1 mm, the needle was physically in contact with the root canal geometry given the uneven wall contour. A needle insertion depth of 2 mm indicates that the needle tip is at a distance of 2.6 mm from the bottom of the root canal, and if the insertion depth is 3 mm, then the needle tip is at a distance of 3.6 mm from the bottom of the root canal. The needle is kept concentric to the apical constriction of the root canal and the fluid inlet velocity of 8.6 m/s (realistic clinical value) is set for each trial.

Figure 38 shows the velocity contour for the needle insertion depth of 2 mm. The maximum velocity is found to be 11.8 m/s which is slightly greater than the maximum velocity for 3 mm needle depth configuration which is 11.7 m/s. The fluid acquires maximum pressure before reaching the slot of needle and dissipates the energy to the fluid inside the root canal.

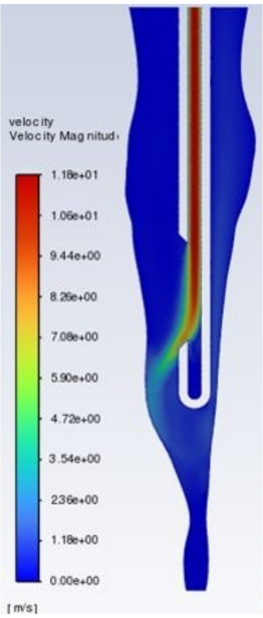

Figure 38: Velocity Contour for the needle depth of 2 mm at 8.6 m/s

Figure 39 below shows the streamline plot for the needle insertion depth of 2 mm and inlet velocity of 8.6 m/s. The flow penetration depth was observed to be 1.6 mm for this needle insertion depth. For the 3 mm insertion depth, the flow penetration depth was 2.3 mm. Again, flow penetration depth is the distance between streamline and bottom of the needle and does not indicate how deep the irrigant penetrates vertically within the root canal. A higher needle insertion depth (i.e., needle moves away from the apical foramen), the apical pressure and wall shear stress decreased, but the turbulent intensity and average wall shear stress remained largely unchanged. Figures 40 and 41 give the wall shear stress and turbulent intensity plots.

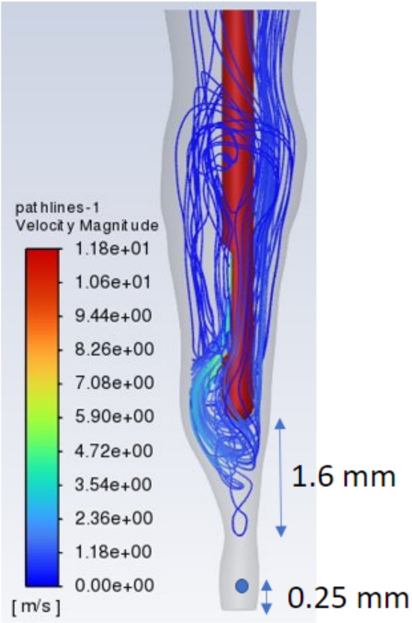

Figure 39: Streamline Scene with Penetration depth and Apical Pressure at 2 mm insertion depth

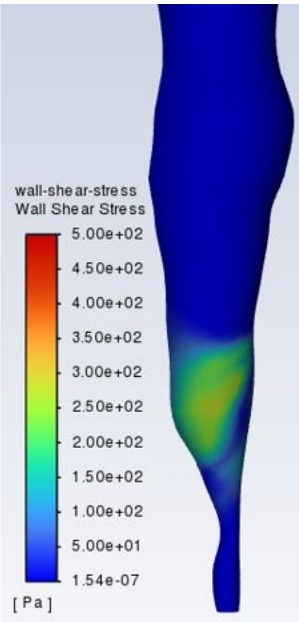

Figure 40:Wall Shear Stress for 2 mm needle insertion depth

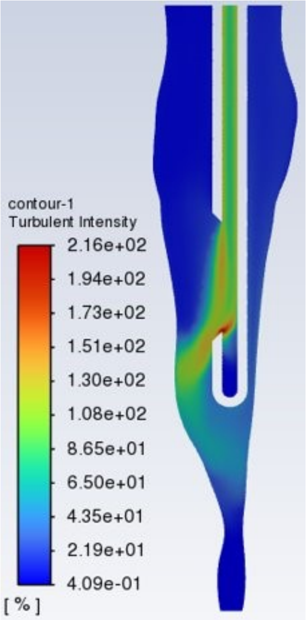

Figure 41: Turbulent Intensity for needle insertion depth of 2 mm

The vector plot for the needle insertion depth of 2 mm is shown in Fig. 42. There appears to be a small swirl zone right below the needle. Also, the flow appears to enter the apical foramen for the 2 mm insertion depth case but this is not observed for the 3mm needle insertion depth.

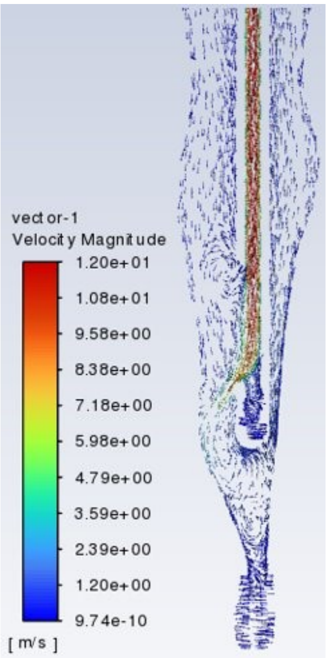

Figure 42: Vector plot for 2 mm insertion depth of the needle

Table 6: Flow Characteristics for 2 mm needle Insertion of the needle

Needle Depth (mm)	Apical pressure (Pa)	Penetration depth (mm)	Distance from bottom of root canal	Wall Shear Stress (Pa)	Maximum Velocity (m/s)	Maximum Turbulent Intensity (%)	Area Weighted Shear Stress (Pa)
2.00	3606.80	1.60	1.01	354.86	11.80	216.00	7.24
3.00	2836.27	2.30	1.31	333.71	11.70	214.00	7.10

4.3.3 Variation of Needle Tilt Angle

For this study, the irrigant inlet velocity was kept at 8.6 m/s, and the needle insertion depth was 3 mm (3.6 mm from bottom of the root canal). Just like for the simplified root canal geometry, the needle was tilted to 1° and 2° CW and CCW direction to obtain the desired configuration below in Fig. 43.

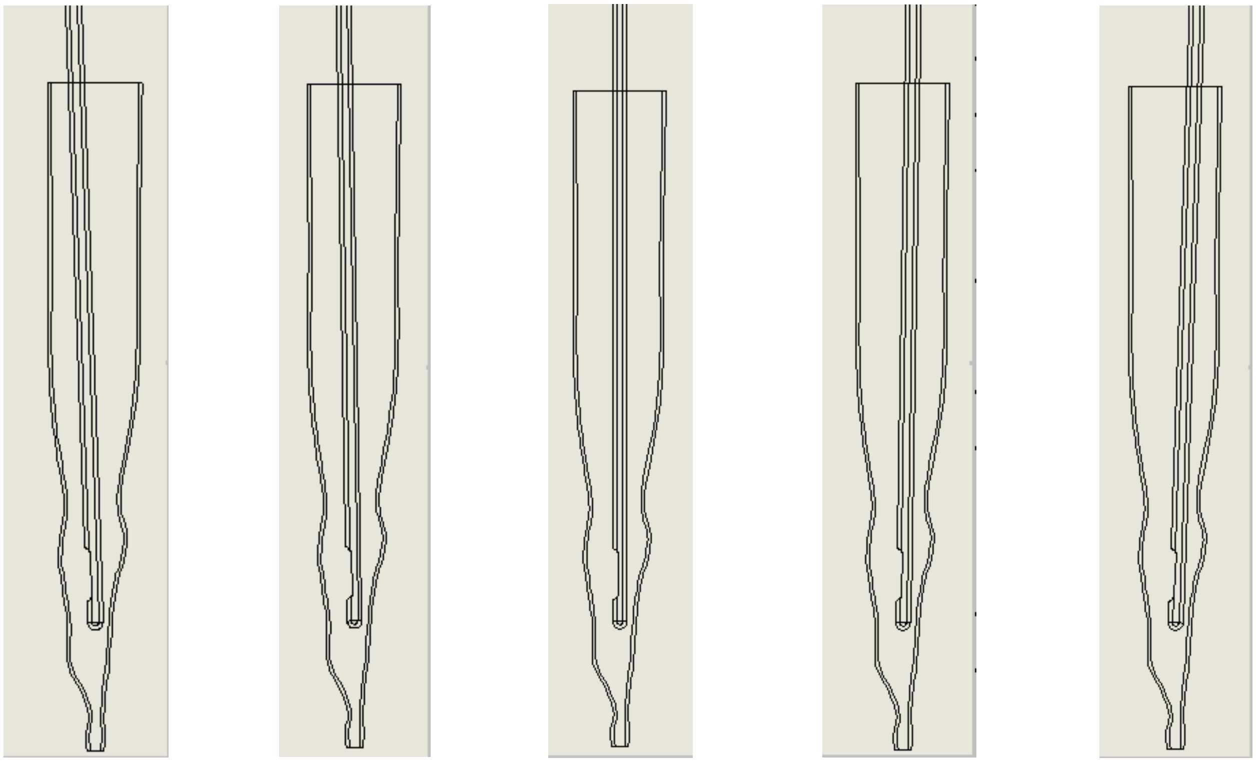

Figure 43: Configuration of different tilt angles: 2° counterclockwise, 1° counterclockwise, 0° tilt, 1° clockwise, 2° clockwise from left to right.

There was no change in maximum velocity observed, and this was as expected. The velocity contour for 1° CW orientation is given in Fig. 44. The contours for all other simulation cases is provided in the appendix.

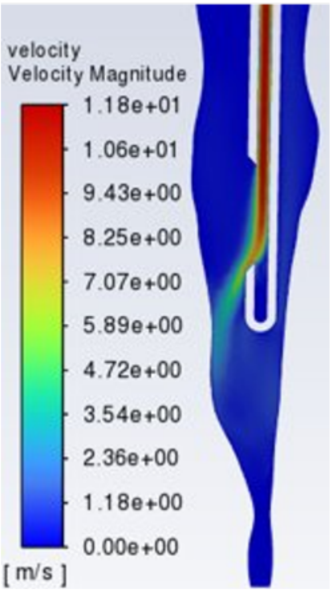

Figure 44: Velocity contour for 1° clockwise rotation of needle

Figure 45 shows the streamline plot for 1° CW orientation. The penetration depth was found to be 2.33 mm and the apical pressure was 2788 Pa. It was observed that the apical pressure was highest for the CCW cases, while the flow penetration was better for the CW cases.

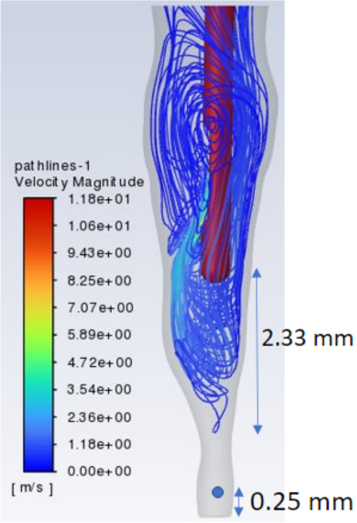

Apical Pressure: 2.8 kPa

Figure 45: Streamline Scene with Penetration Depth and Apical Pressure for 1° clockwise rotation of needle

The wall shear stress for the aforementioned orientation is given below in Fig. 46. It was found that the maximum wall shear stress occurred for the 2° CW case, but there was not much variation across all four orientations. The average wall shear stress was highest for the 1° CCW case, and interestingly the lowest value was found for the 2° CCW case.

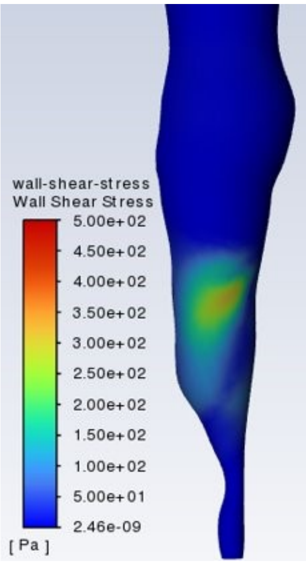

Figure 46: Wall Shear Stress Contour for 1^0 *clockwise rotations of needle*

The plot for the turbulent intensity is shown in Fig. 47. While there was no significant change in maximum value across the board for all simulations, the CW orientations had the highest maximum values for turbulent intensity.

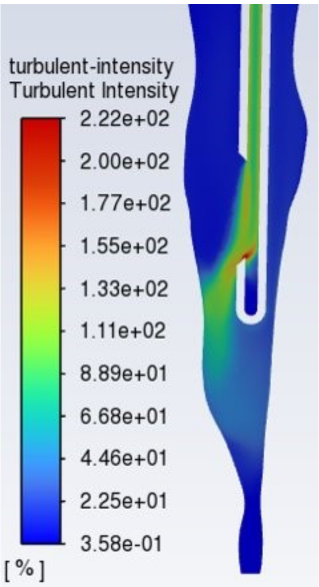

Figure 47: Turbulent intensity for penetration depth and apical pressure for 1° clockwise rotation of needle

The vector plot for the 1° CW tilt is shown below. There doesn't appear to be any noticeable swirl.

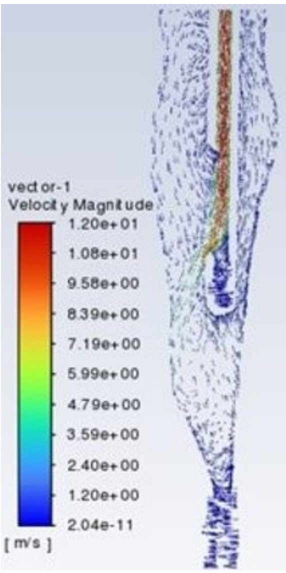

Figure 48: Vector plot for 1° clockwise rotation of needle

In short, the CW orientations had smaller apical pressures, higher turbulent intensity, and higher flow penetration.

Table 7: Flow Characteristics for variation of Tilt Angle

Tilt Angle	Apical pressure (Pa)	Penetration depth (mm)	Distance from bottom of root canal	Wall Shear Stress (Pa)	Maximum Velocity (m/s)	Maximum Turbulent Intensity (%)	Area Weighted Shear Stress (Pa)
2 CW	2692.16	2.27	1.34	351.15	11.80	222.00	6.91
1 CW	2788.00	2.33	1.28	328.43	11.80	222.00	7.13
0 Tilt	2836.27	2.31	1.30	333.71	11.70	214.00	7.10
1 CCW	3003.51	2.19	1.43	339.36	11.80	217.00	7.52
2 CCW	3083.21	1.72	1.89	320.73	11.80	211.00	6.85

4.4 Comparison of Simplified and Realistic Root Canal

4.4.1 Variation of Speed

When comparing the maximum velocity for both root canal geometries, there was no difference as expected for the different irrigant inlet velocity values (see Fig. 49). However, there was visible difference when comparing the flow penetration depth as seen in Fig. 50. As the inlet velocity increased, the flow penetration increased for both geometries (i.e., trend was the same), but the more realistic root had consistently higher flow penetration depth across the board. For both geometries, it appears that at higher velocities the flow penetration depth levels off.

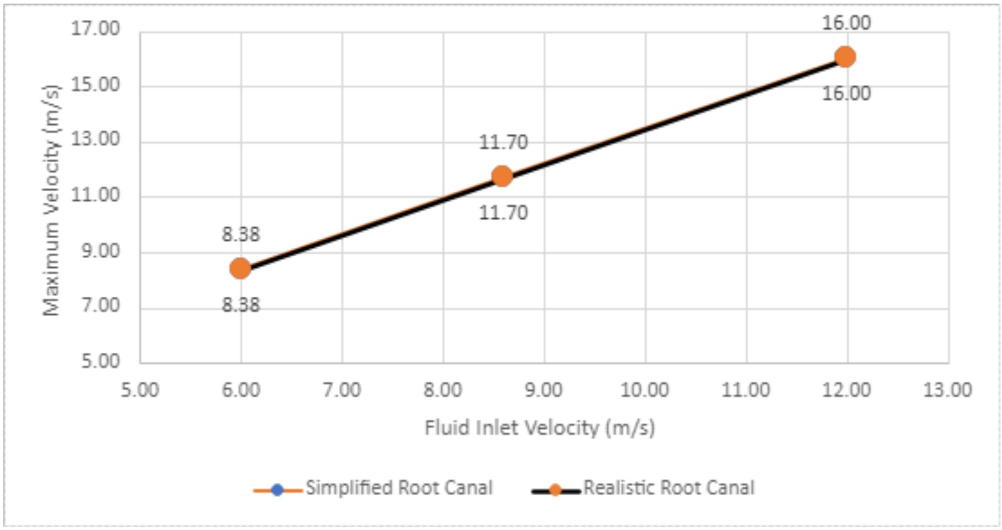

Figure 49: Graph of fluid inlet velocity vs maximum velocity

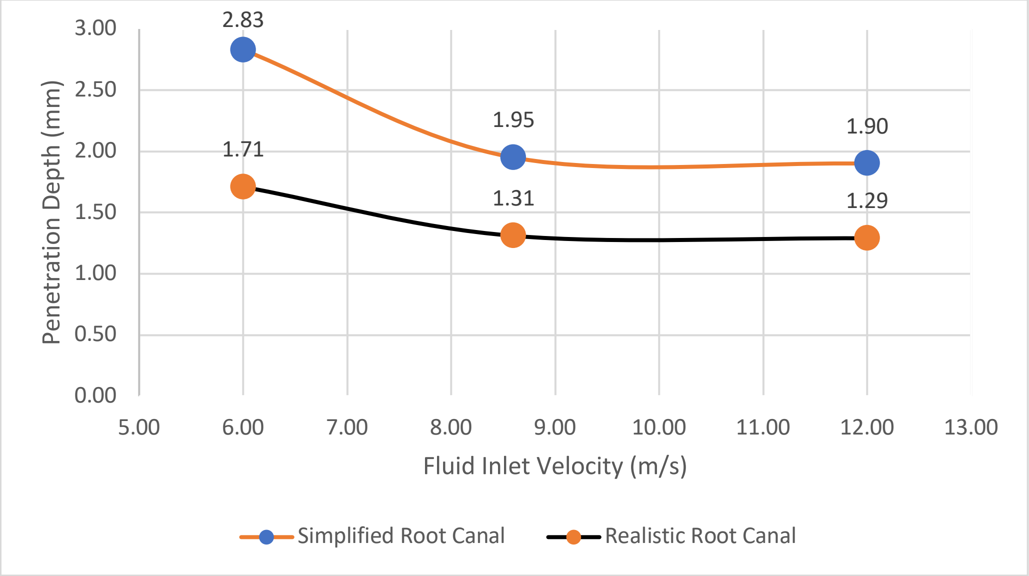

Figure 50: Graph of fluid inlet velocity vs penetration depth

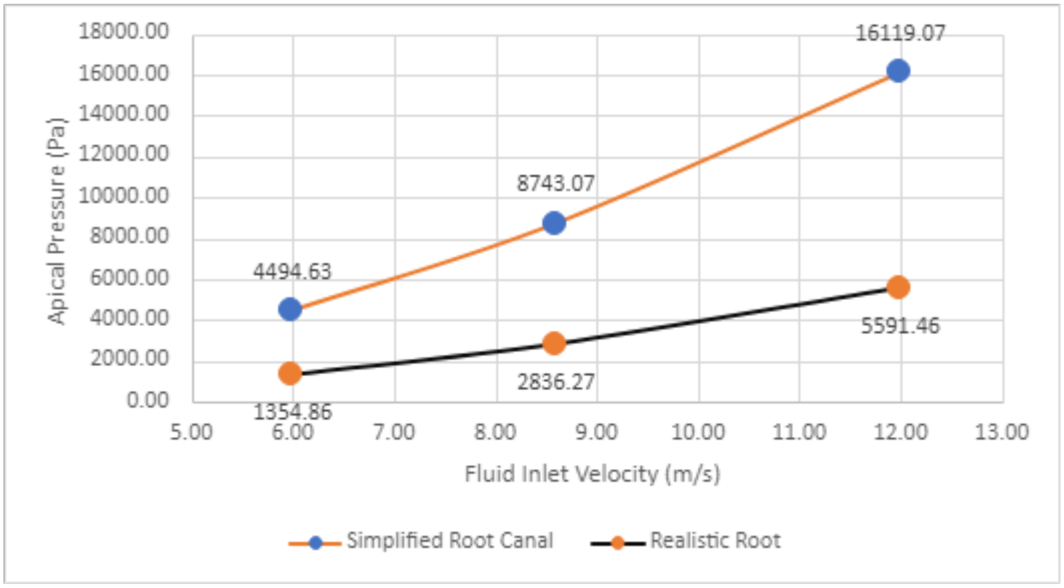

Figure 51: Graph of fluid inlet velocity vs apical pressure

Figure 51 shows the variation of apical pressure with inlet flow velocity. Both geometries showed the same trend where an increase in inlet velocity increased the apical pressure. The simplified geometry appeared to have consistently higher apical pressures at all flow rates. In addition, the rate of increase in apical pressure with flow rate was higher for simplified case. From Fig. 52, it can be seen that there was no significant difference in maximum turbulent intensity values at each irrigant inlet flow rate, but turbulent intensity increased with flow rate for both geometries.

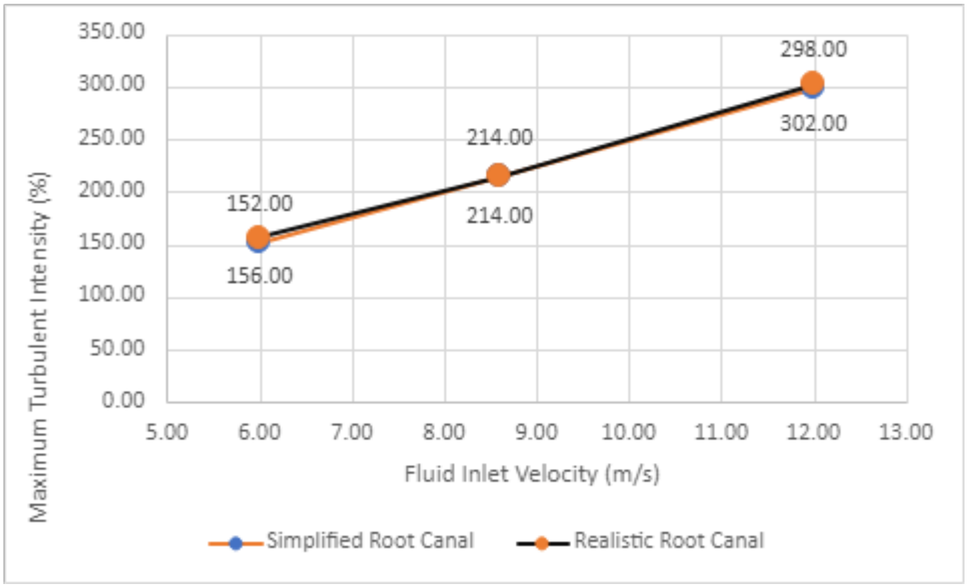

Figure 52: Graph of fluid inlet velocity vs maximum turbulent intensity

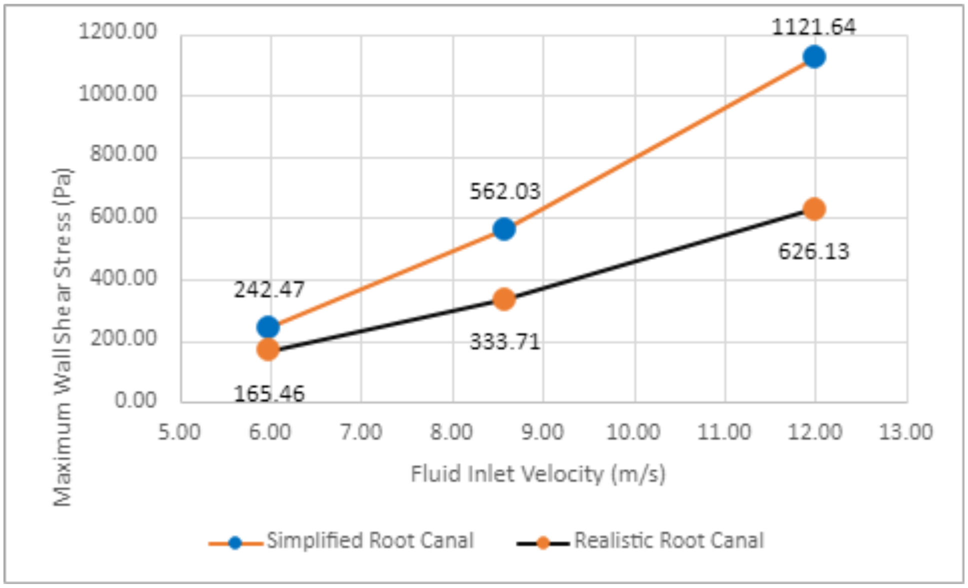

Figure 53: Graph of fluid inlet velocity vs maximum wall shear stress

The maximum wall shear stress and average wall shear stress increased with flow rate for both geometries; however, the realistic root canal displayed consistently lower values at all flow rates when compared to the simplified geometry. Also, as flow rate increased, the rate of increase in maximum and average wall shear stress was higher for the simplified geometry.

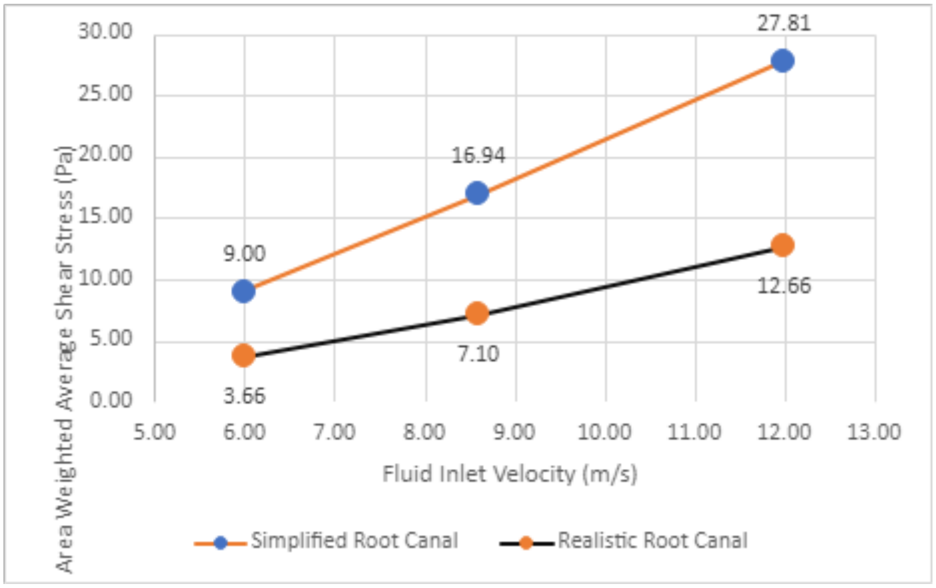

Figure 54: Graph of fluid inlet velocity vs area averaged wall shear stress

4.4.2 Needle Insertion Depth

The maximum velocity does not appear to be largely affected by needle insertion depth for both geometries as shown in Fig. 55.

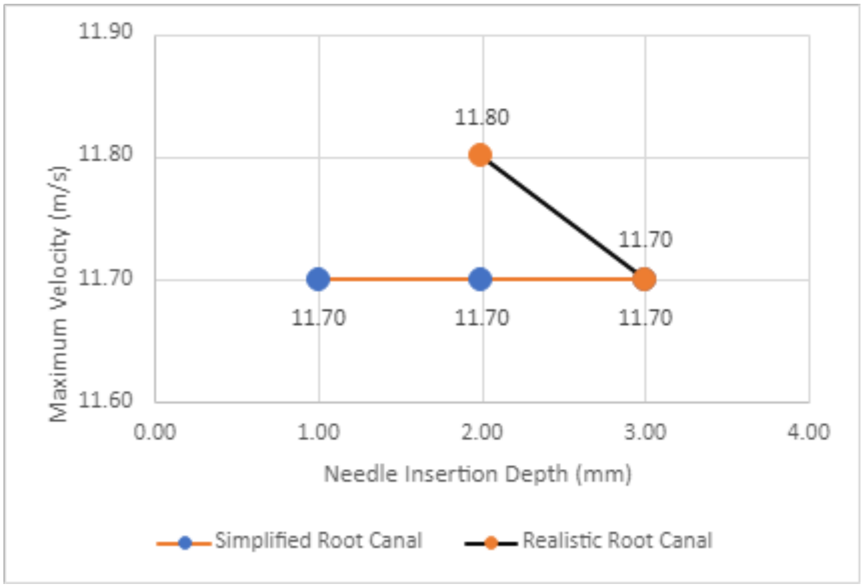

Figure 55: Graph of needle insertion depth vs maximum velocity

Results obtained indicate that as the needle insertion depth increased (needle moves away from apical foramen), the flow penetration depth increased for both geometries as shown in Fig. 56. With that said, realistic geometry had consistently lower flow penetration depth when compared to that of the simplified geometry. Another point to note is that as the insertion depth increased from 2 mm to 3 mm, the more simplified geometry showed a sharper increase in flow penetration.

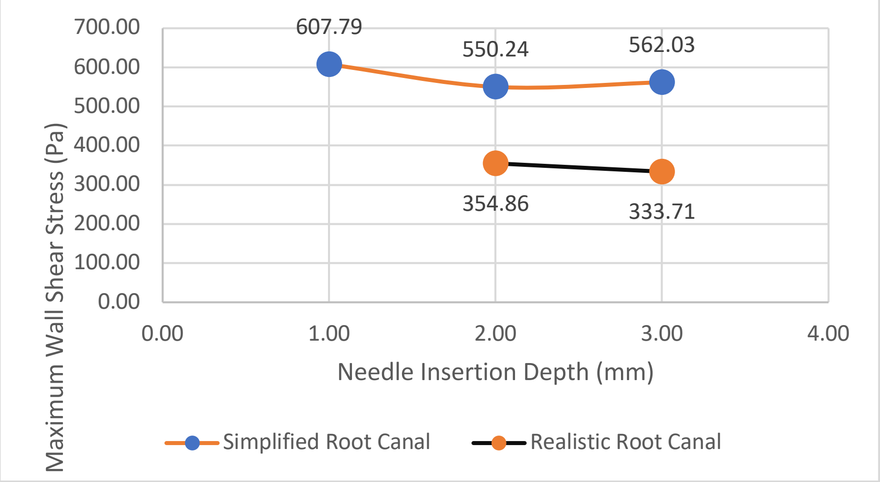

Figure 56: Graph of needle insertion depth vs flow penetration depth

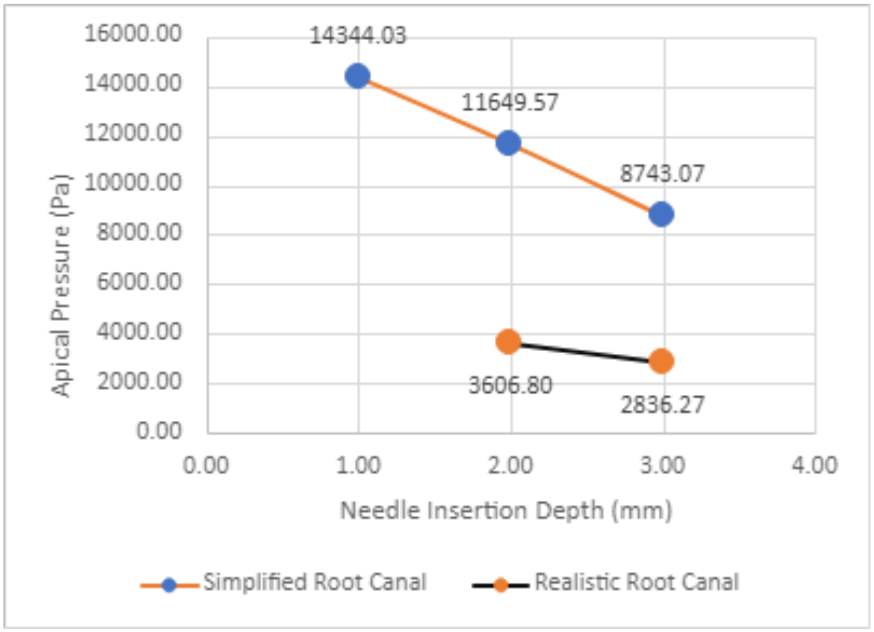

Figure 57: Graph of needle insertion depth vs apical pressure

Figure 57 indicated that both geometries demonstrated a diminishing linear trend as needle insertion depth increased (needle moves away from apical foramen). Despite this, the apical pressure at each depth was higher for the simplified root canal, and the drop in apical pressure with insertion depth was more pronounced for this geometry as well.

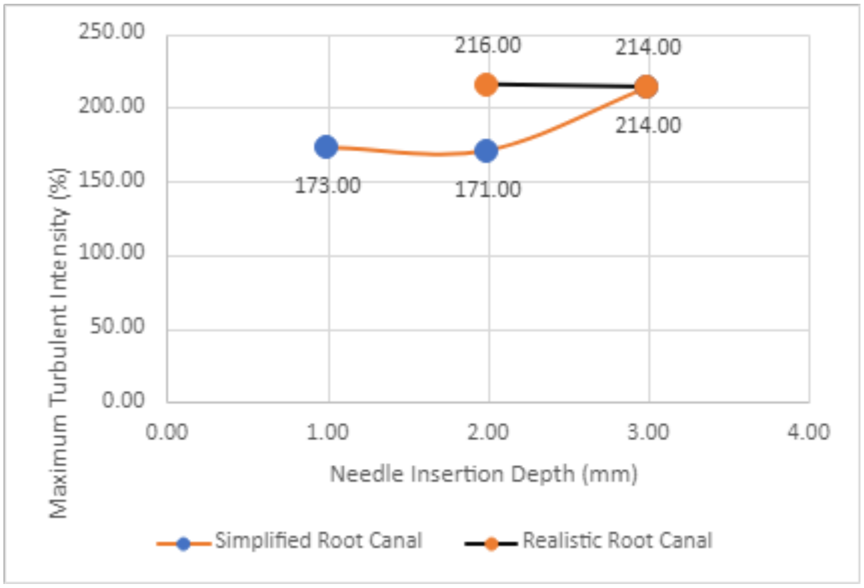

Figure 58: Graph of needle insertion depth vs maximum turbulent intensity

Interestingly, the maximum turbulent intensity for the 3 mm needle insertion depth is found to be the same for both root canal geometries (Fig. 58). However, for the 2 mm insertion depth, the realistic root geometry had a higher maximum turbulent intensity (26.3% higher). While the maximum turbulent intensity showed no significant change with needle insertion depth for the realistic root canal, it did increase with insertion depth for the simplified geometry. This shows that when the needle is positioned closer to the apical foramen, the realistic root geometry has better turbulent swirl characteristics.

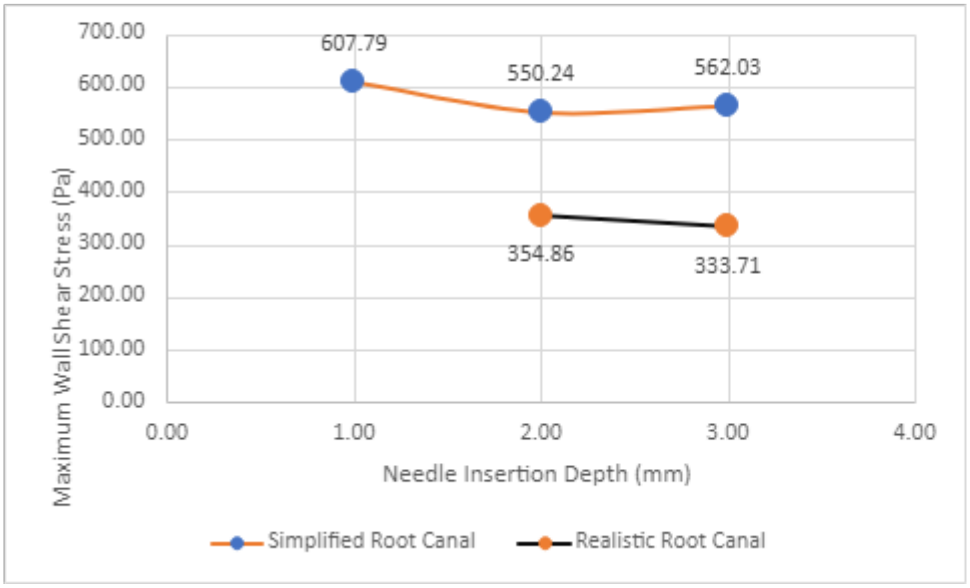

Figure 59:Graph of needle insertion depth vs maximum wall shear stress

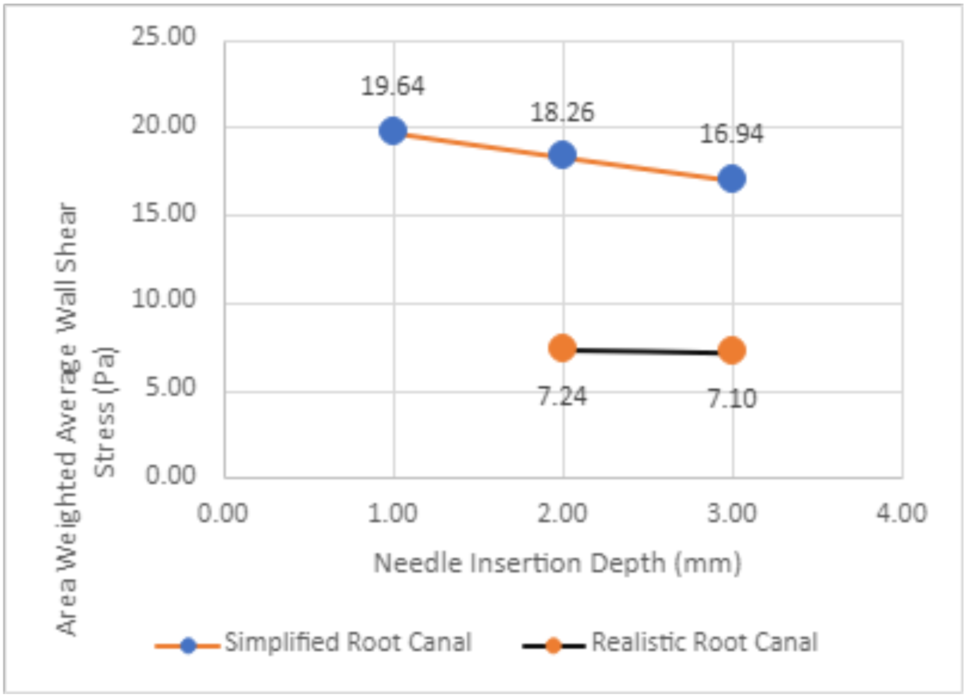

Figure 60:Graph of needle insertion depth vs area-weighted wall shear stress

Figures 59 and 60 illustrate the trends for maximum wall shear stress and average wall shear stress. The maximum wall shear stress was always lower (roughly half) at each needle depth for the realistic root canal and had a linear decrease from 2 mm to 3 mm insertion depth. The simplified geometry, in general, showed a decreasing trend as well, but there was a slight increase in maximum wall shear stress from 2 mm to 3 mm needle insertion depth. As for average shear stress, there was not much change for the realistic root, but a consistent linear decrease trend was seen for the simplified root. Interestingly, the maximum wall shear stress is about 30 times the average shear stress for the for the simplified root, but for the complex root it was about 50 times greater.

4.4.3 Needle Tilt Angle

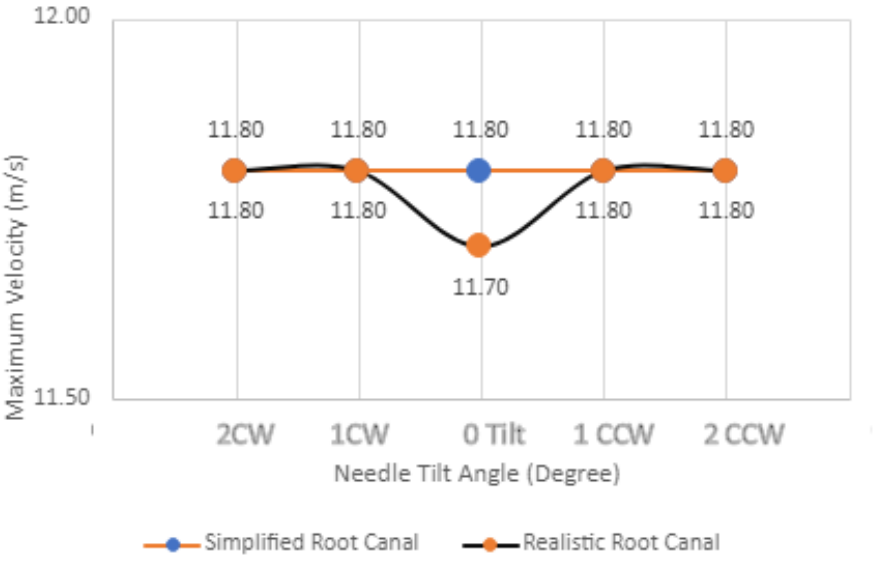

Figure 61: Graph of needle tilt angle vs maximum velocity

Across the board for all tilt angles, the maximum velocity showed no major difference. The only slight difference was for the no tilt case for the realistic root as shown in Fig. 61.

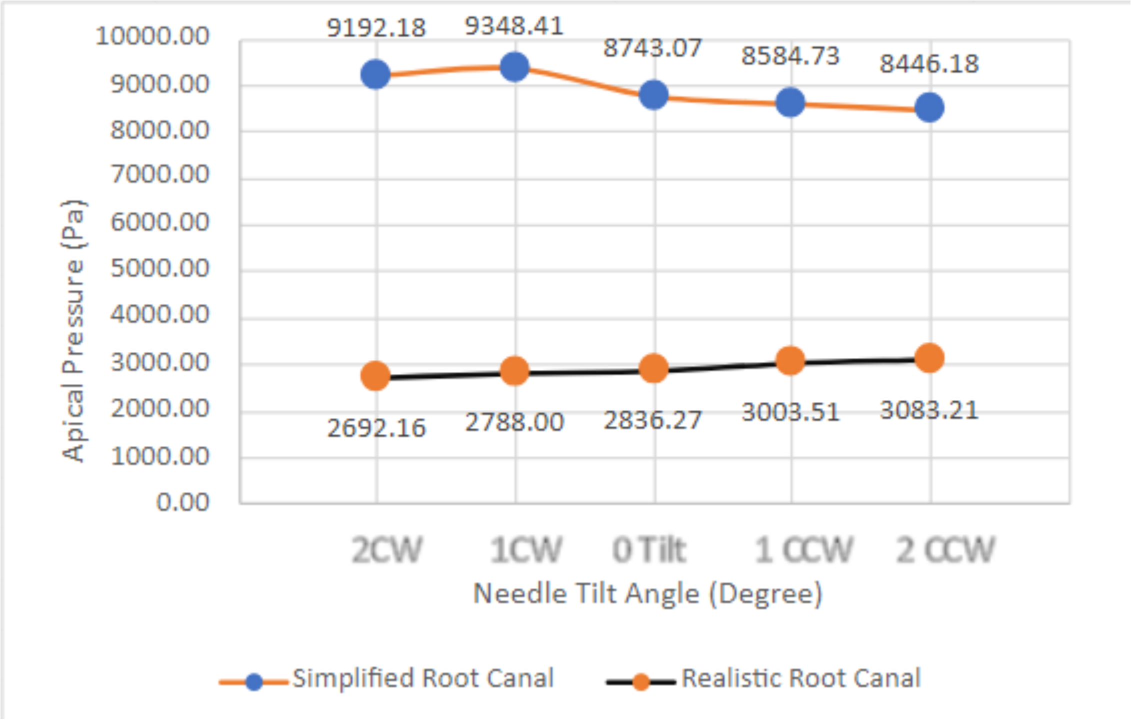

Figure 62: Graph of needle tilt angle vs apical pressure

There were contrasting trends for variation of apical pressure with tilt angle for both geometries (see Fig. 62). For the realistic root, there was a gradual increase in apical pressure as the needle tilted from CW to CCW orientation. However, for the simplified root, there was a gradual decrease in apical pressure as the needle tilted from CW to CCW orientation. Despite that, the apical pressure was consistently lower for the realistic root for all tilt angles. The maximum apical pressure occurred at 1° CW for simplified root and at 2° CCW for the realistic root.

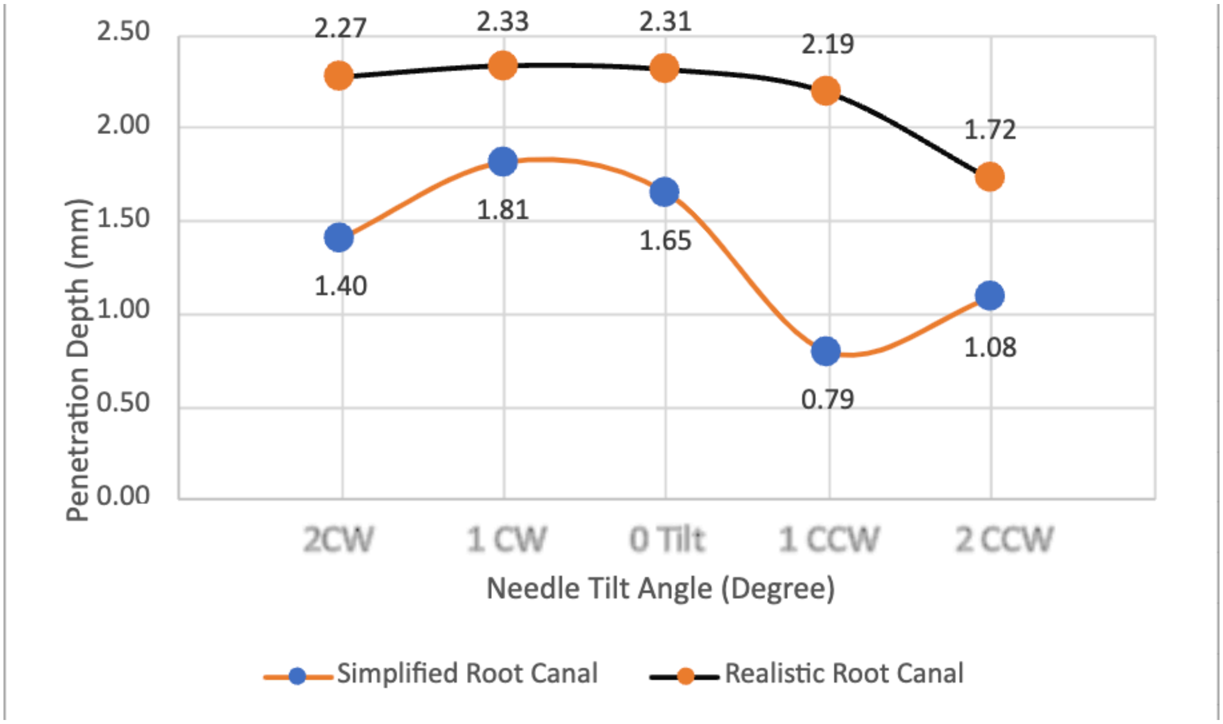

Figure 63: Graph of needle tilt angle vs flow penetration depth

Figure 63 shows the trend with tilt angle for flow penetration depth. For the realistic case, the flow penetrated deeper for all needle orientations, and it was greatest for the 1° CW tilt. The lowest flow penetration was witnessed for the most counterclockwise tilt. For the simplified root, the flow penetration was also highest for the 1° CCW tilt and lowest for the 2° CCW tilt. Despite this consistency for both geometries, the simplified root did not show a consistent pattern of flow penetration vs. needle tilt as shown in Fig. 63. The percent change between each tilt angle was large for this root geometry.

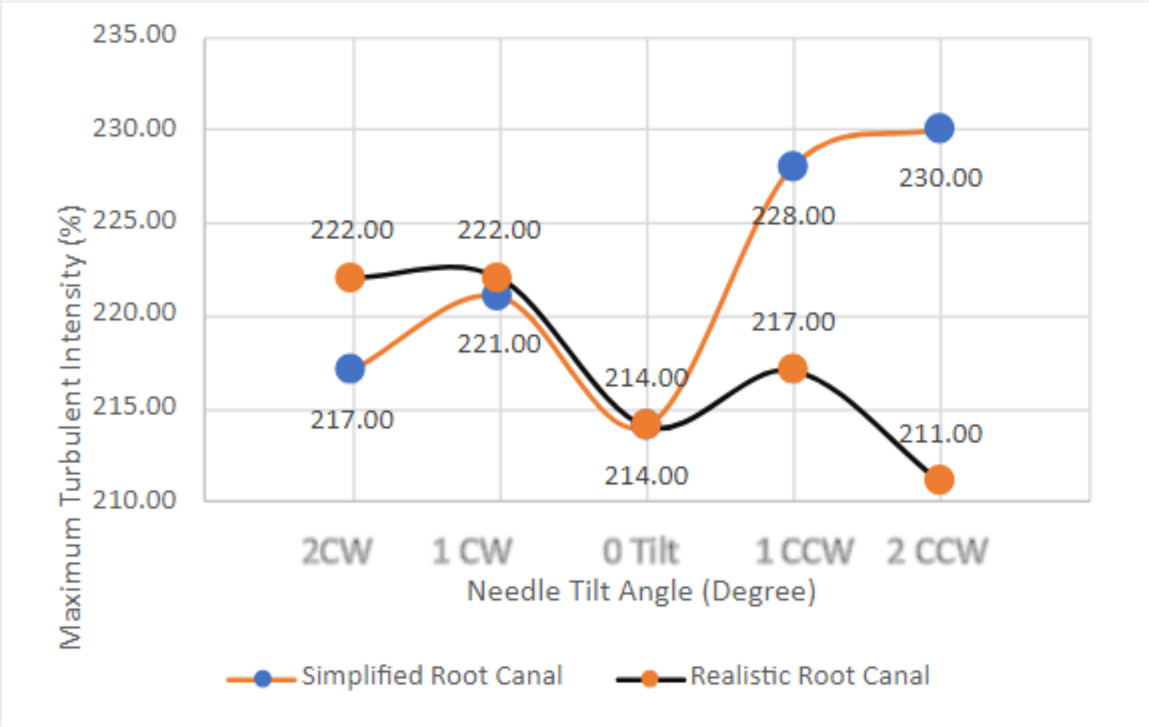

Figure 64: Graph of needle tilt angle vs maximum turbulent intensity

With respect to maximum turbulent intensity, the realistic root had higher values for the CW tilt; there was no difference between 1° or 2° tilt as seen in Fig. 64. The lowest value for this root geometry is for a 2° CCW tilt. The simplified geometry showed the reverse trend, where the maximum turbulent intensity value was higher in the CCW orientations. Interestingly, for the no tilt case, both root geometries had identical maximum turbulent intensity values.

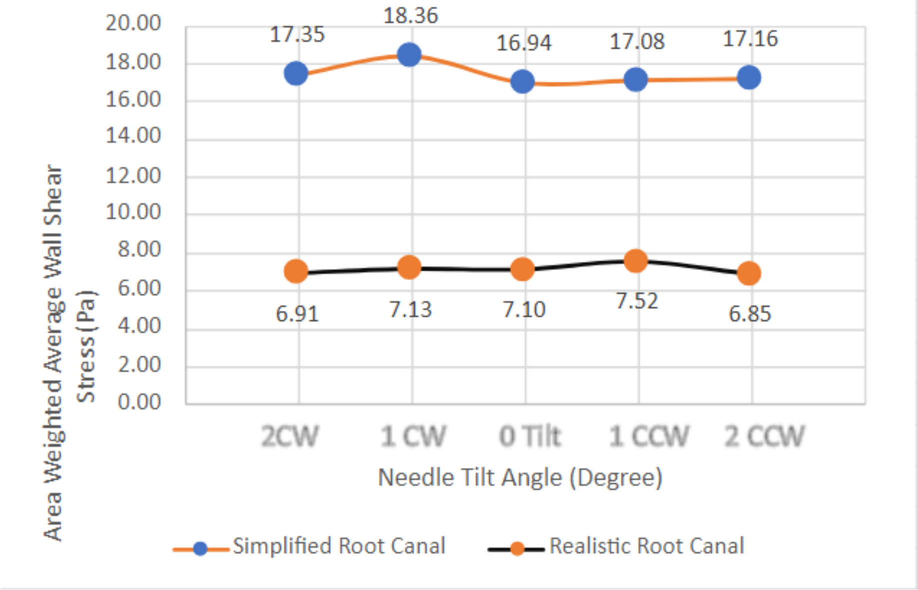

Figure 65: Graph of needle tilt Angle vs averaged wall shear stress

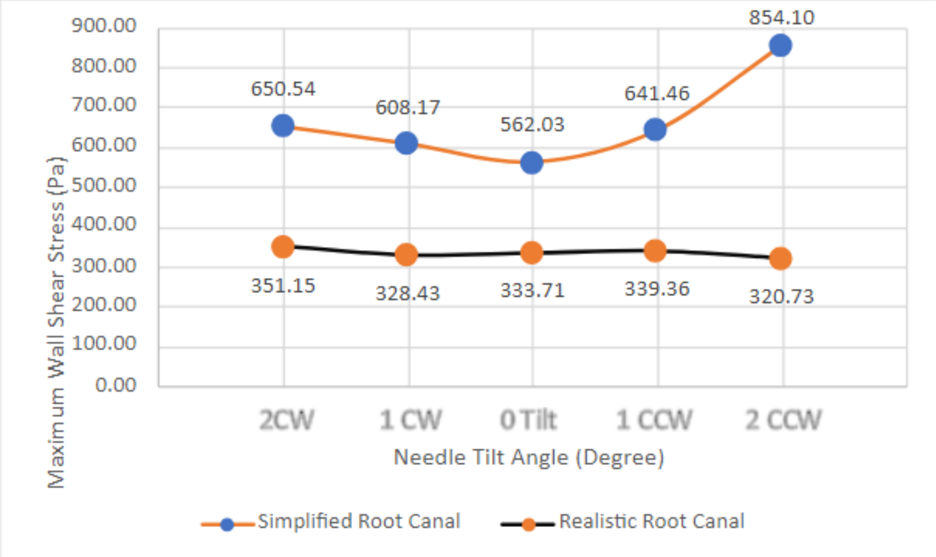

Figure 66:Graph of needle tilt angle vs maximum wall shear stress

Figures 65 and 66 illustrate the trends for the average wall shear stress and maximum wall shear stress for both geometries, respectively. The simplified root had consistently higher average wall shear (double) and maximum wall shear (triple) stresses throughout all tilt angles. While there was no significant change for either output parameter, the maximum wall shear stress was highest for the 1° CW orientation for simplified root and 2° CCW tilt for realistic root, i.e., inverse trend for both geometries.

Chapter 5 Design of Innovative Needle

There are some standardized needles that are used for endodontic therapy. These needles include flat bottomed, side vented, double side vented, notched and multi vented needle. The flat needle injects the flow directly into the apical region (vertical ejection from needle end) thus increasing the apical pressure without much effect on wall shear stress whereas for the side vented needle, the wall shear stress is greater on one side with less effect on the other side of root canal wall. The goal of this section is to modify the current side vented needle while keeping the manufacturability of the new needle in mind in order to enhance the irrigant flow characteristics within the root canal.

Table 8: Selection of best combination of input parameters

Variation of Speed (m/s)	Apical pressure (Pa)	Flow Penetration depth (mm)	Flow Distance from Root Canal Bottom (mm)
6.00	1354.86	1.90	1.71
8.60	2836.27	2.30	1.31
12.00	5591.46	2.32	1.29

Needle Depth (mm)	Apical pressure (Pa)	Flow Penetration depth (mm)	Flow Distance from Root Canal Bottom (mm)
2 mm	3606.80	1.60	1.01
3 mm	2836.27	2.30	1.31

Tilt Angle	Apical pressure (Pa)	Flow Penetration depth (mm)	Flow Distance from Root Canal Bottom (mm)
1 CW	2788.00	2.33	1.28
2 CW	2692.16	2.27	1.34
0 Tilt	2836.27	2.30	1.31
1 CCW	3003.51	2.19	2.19
2 CCW	3083.21	1.72	1.89

To achieve this, first the optimum combination of input parameters was selected based on results from previous sections and simulations run with the realistic root canal; see Table 8. While the flow penetration depth provides the distance between streamline and needle bottom, the flow distance from root canal bottom to the streamline must be calculated to understand how deep the irrigant is within the root canal. To calculate this, the flow penetration depth was subtracted from 3.6 mm (distance between needle bottom and root canal bottom). The best case was the 2 mm needle insertion depth since the distance between irrigant and root canal bottom was the smallest. The needle tilt angle was 1 CW since it had the lowest apical pressure and provided the best distance from flow to root canal bottom. The irrigant inlet velocity was selected as 8.6 m/s since this gave the best possible combination of apical pressure and distance between flow and root canal bottom. These input parameters are then held constant while the baseline side vented needle is then modified to study the effect on flow characteristics.

The two most important output parameters that were examined were the turbulent intensity contour plot and apical pressure. From the literature, it was found that the apical pressure must not exceed 35 mm of Hg (mercury), which is the equivalent of 4.66 KPa. This pressure is the intrapulpal tissue pressure, and if exceeded irreversible changes may occur in the root canal [18]. It is assumed that exceeding this pressure could result in extrusion of the irrigant. For comparison purposes, the flat-bottomed needle is also considered since this geometry results in the maximum apical pressure with the best flow penetration within the root canal. The goal here is to improve the swirl but avoid going beyond the threshold pressure.

For the flat-bottomed needle with aforementioned optimum input parameters, the apical pressure recorded was 13,854 Pa. This very high pressure would most likely cause extrusion of the irrigant, and this is very undesirable. The flow penetration depth was found to be 1.6 mm. The turbulent and velocity contours for the flat-bottomed needle are given below in Fig. 67.

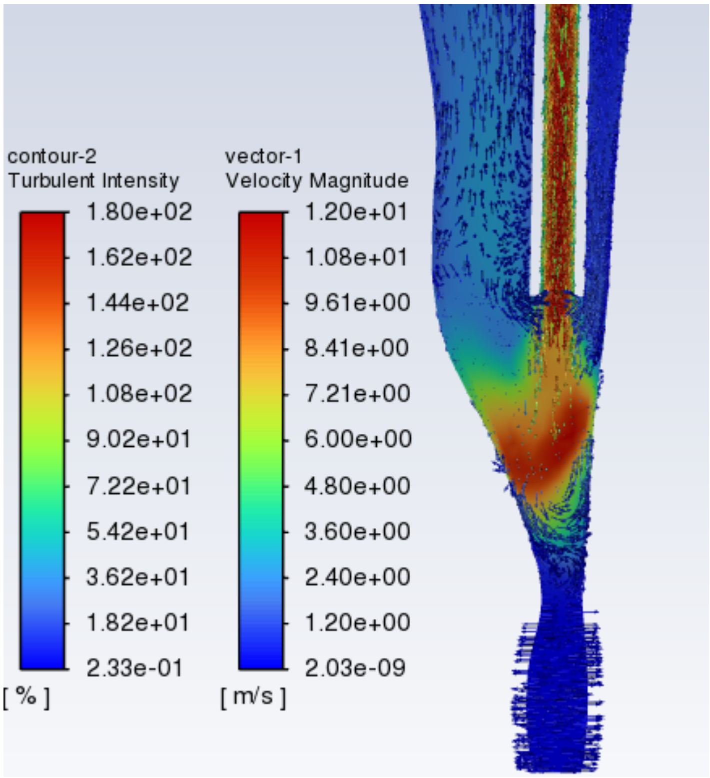

Figure 67:Turbulent and vector contour overlapped for flat bottomed needle.

There appears to be very high turbulent intensity at the constricted region of the root canal for the flat-bottomed needle. This is very beneficial since cleaning is enhanced within the root canal, but the high apical pressure renders this case not practical. The idea is to maintain the high turbulent intensity but decrease the apical pressure. For lower apical pressures, the side vented needle is an excellent candidate since the fluid ejects from the side and not directly into the apical constriction. For the optimal combination of input parameters, the side vented needle's (baseline case studied in previous sections) turbulent intensity and vector plot is shown below in Fig. 68.

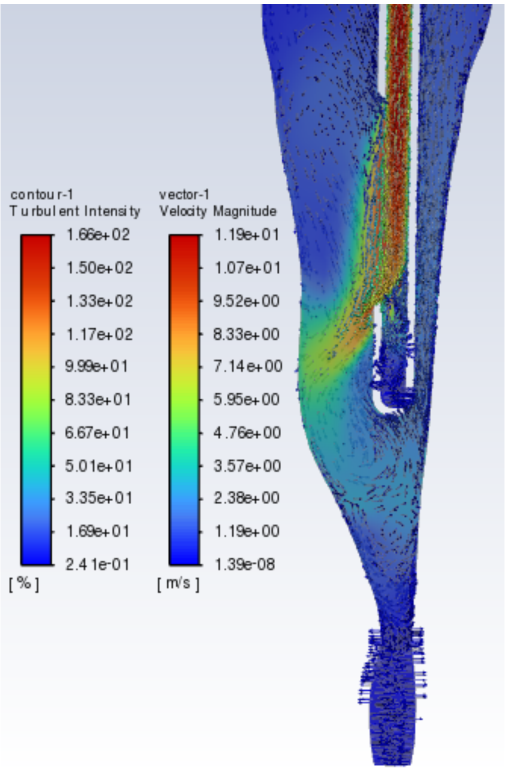

Figure 68: Turbulent intensity and vector plot for side-vented baseline needle

While the baseline side vented needle was good in terms of apical pressure, the turbulent intensity distribution was not ideal and needed to be improved, especially right below the needle and in the apical constriction. The baseline geometry was changed in such a way to direct the flow better towards the canal wall and promote swirl once the flow rebounds off the side wall of the root canal. This involved a slight lip at the top of the needle that was designed to be parallel to the flow leaving the side vent. The dimensions of the lip are given in Fig. 69 below.

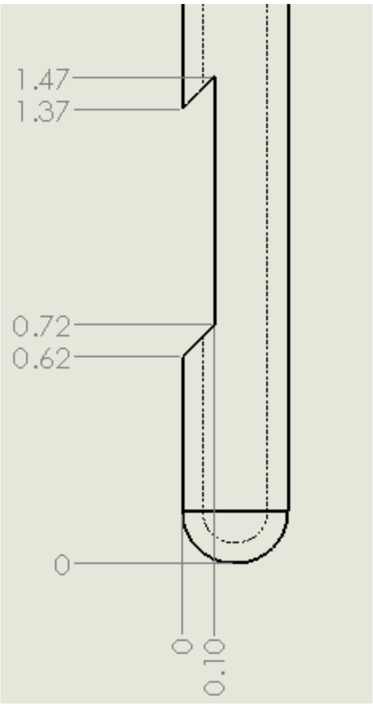

Figure 69: Detailed drawing of needle design 1

The turbulent intensity and velocity contours are given in Fig. 70 below. It can be seen that the turbulent intensity is significantly reduced when compared to the flat-bottomed needle. There is strong turbulence near the left root canal wall, but it is not pronounced above the apical constriction (i.e., immediately below the needle tip). The velocity vectors do confirm that there is some swirl near the apical constriction. However, the apical pressure did drop significantly and was 3,408 Pa as opposed to 13,854 Pa from the flat-bottomed needle. This is an improvement as the threshold pressure of 4,660 Pa is not breached. While this design was a step in the right direction, the turbulent intensity was lacking, so the next modification was made.

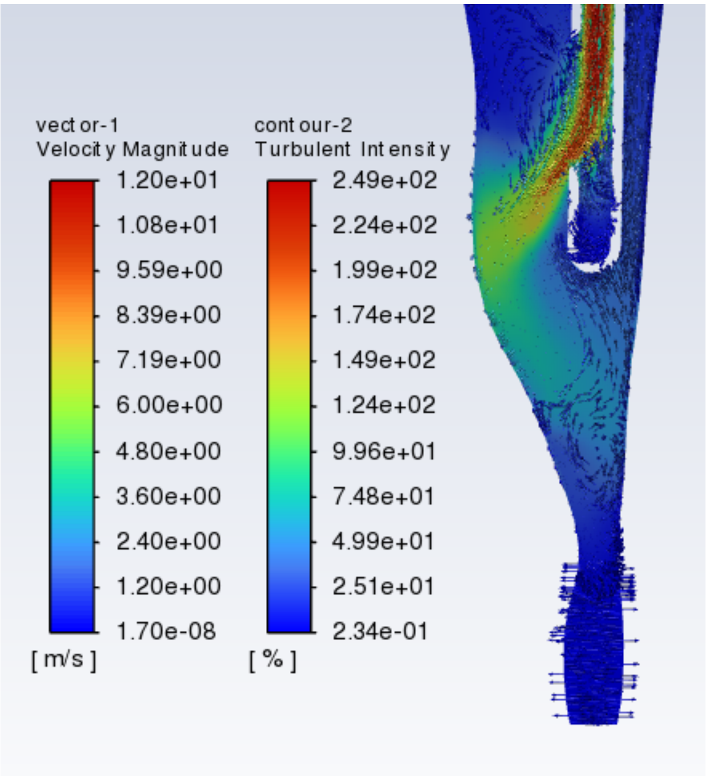

Figure 70: Turbulent and vector contour overlapped for new needle design 1

To boost the intensity, the side vented needle was further modified with an orifice at the bottom of the needle. The motivation was to get more flow directly eject into the constriction, just like a flat-bottomed needle. Since only a small portion of the flow will go directly into the constriction, this shouldn't create a significant increase in apical pressure. The orifice diameter at the bottom was set to 0.05 mm as shown in Fig. 71 below. Simulation results showed no significant change in turbulent intensity and apical pressure (3,464 Pa), but there was more swirl visible in the apical constriction as shown by the velocity vectors (Fig. 72). This indicated that the orifice diameter was too small creating a large flow resistance and hence less flow from the bottom. Also, this design iteration showed better swirl near the left wall of the root canal, and this was absent for previous design.

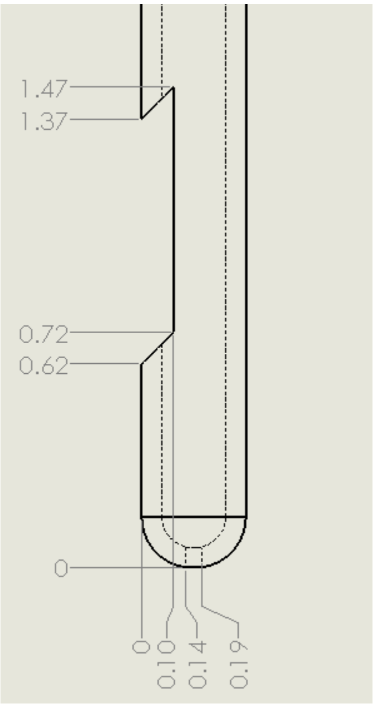

Figure 71: Needle design 2 detailed drawing

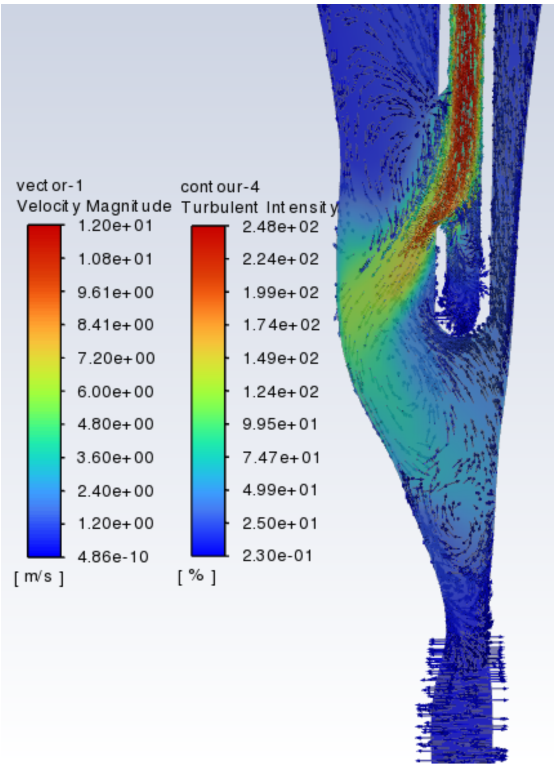

Figure 72: Turbulent and vector contour overlapped for needle design 2.

To circumvent this issue, the size of the orifice at the bottom was increased from 0.05 mm to 0.1 mm, and a slight change was also made to the dimensions of the side vent to strengthen the swirl near the left wall as shown in Fig. 73 below. Design iteration 3 resulted in an apical pressure of 3183.2 Pa, and this was well below the threshold pressure. The modification to the side vent strengthened the swirl near the left wall of the root canal, and the increase in orifice diameter strengthened the turbulence intensity and swirl vertically below the needle as shown in Fig. 74.

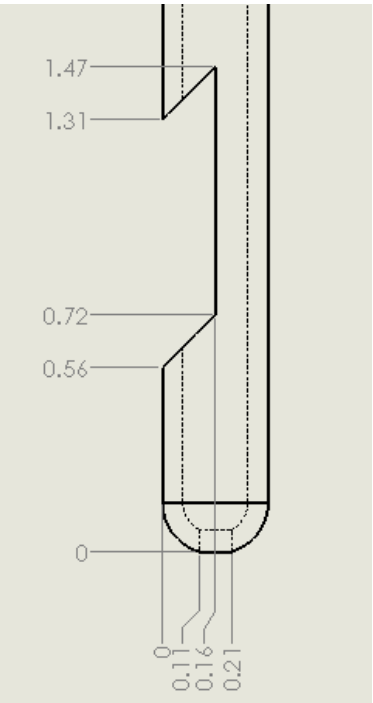

Figure 73: Detailed Drawing for needle design 3

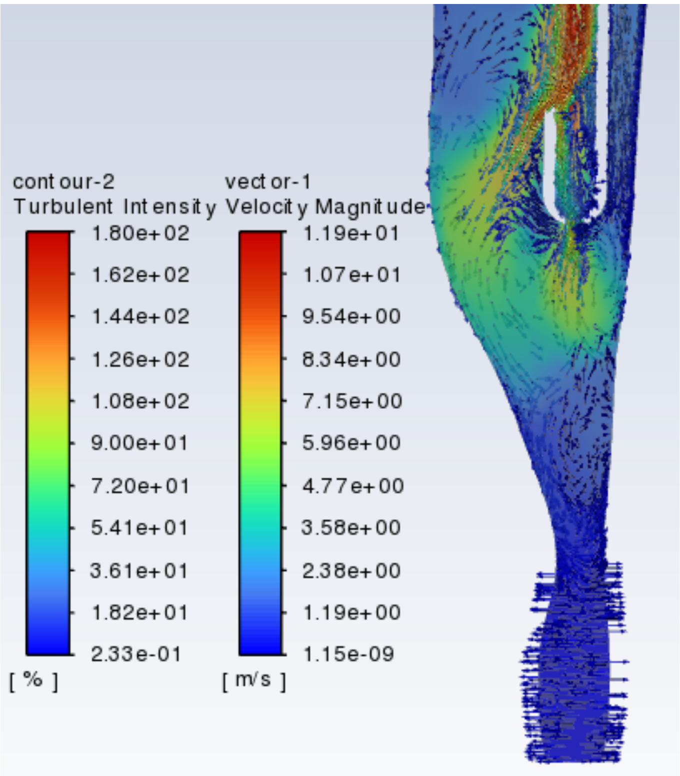

Figure 74: Turbulent and vector contour overlapped for needle design 3

To further make the flow better, the orifice at the bottom of the needle is increased to 0.12 mm as shown in Fig. 75. The depth of the notch is maintained the same as in needle design 3. The apical pressure of 3678.37 Pa is obtained from the simulation which was within our threshold value of 4,666 Pa. Figure 76 shows the distribution of turbulent intensity and vector plot for the needle iteration number 4. It is found to be the best in terms of swirl and distribution of turbulent intensity at the apical third region of the root canal, thus increasing the chance of efficient and safe irrigation.

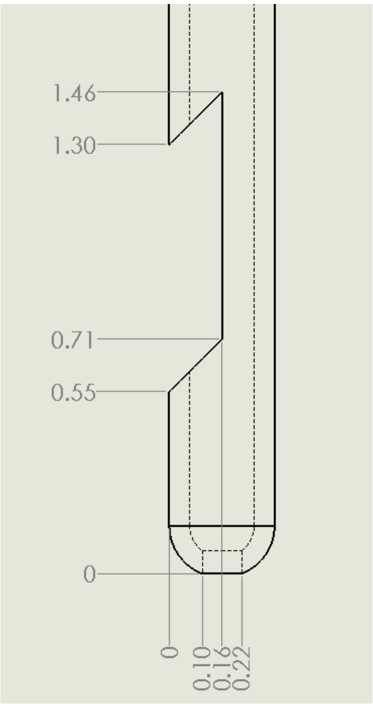

Figure 75: Detailed drawing of needle design 4

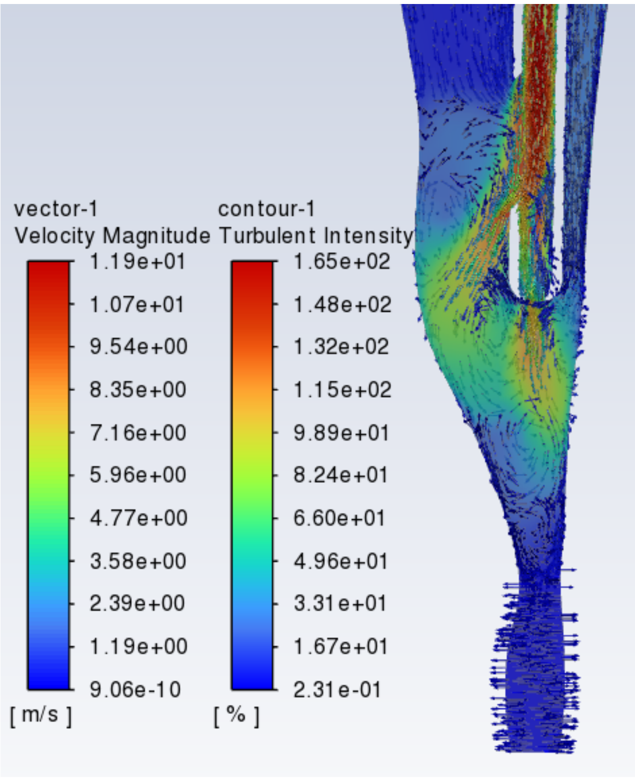

Figure 76: Turbulent and vector contour overlapped for needle design 4

Chapter 6 Conclusion

The major objectives of this study were to: (1) develop a more realistic root canal geometry in CAD by using data from the literature; (2) establish flow characteristics trends for simplified root canal and compare them to realistic root canal; (3) modify existing needle to enhance flow characteristics. From objectives 1 and 2, it was concluded that the flow characteristics are not the same for simplified and realistic root canal geometries, and future studies must use the more realistic root canal geometry as opposed to the simplified geometry that is used by many researchers. Also, studies in the literature did not account for threshold pressure that could cause extrusion of the irrigant and significant discomfort. This study accounted for that pressure and identified the optimal combination of irrigant flow rate, needle insertion depth, and needle tilt angle. Finally, through objective 3, a new needle design is proposed that enhances flow turbulence and swirl near the apical third which might result in improved irrigation and hence irrigation success.

Chapter 7 Future Scope of study

CFD alone is not sufficient to predict efficiency. Therefore, it is important to validate the information obtained in this study through experiments. Also, the simulation can be improved in the following way. For this study, the root canal was already patched with liquid, and the needle injected irrigant into existing fluid in the root canal. It is recommended that future studies use multiphase flow model to simulate the onset of irrigation when the fluid ejects into the root canal filled with air. More aggressive needle designs could be considered to improve swirl characteristics and keep apical pressure below the threshold value.

Appendices

Appendix A

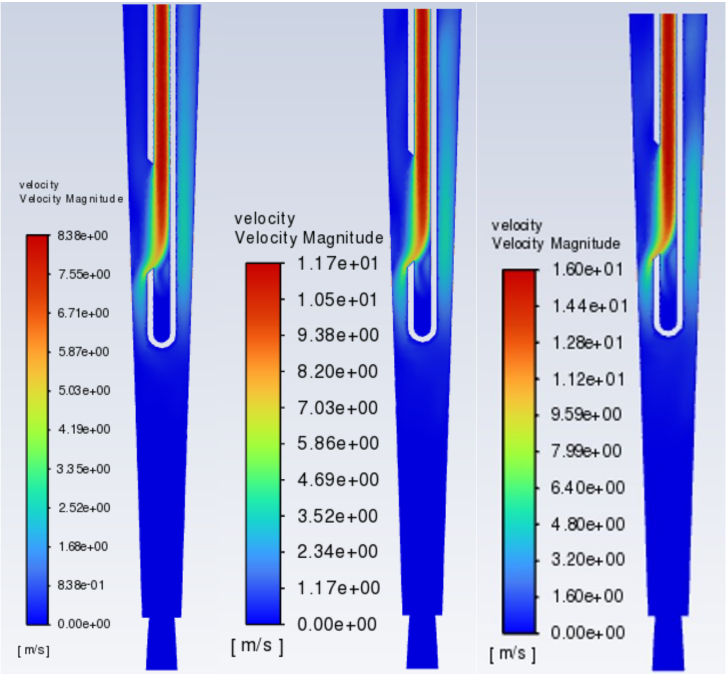

Figure 77: Velocity contour for 6 m/s, 8.6 m/s, 12 m/s for simplified geometry

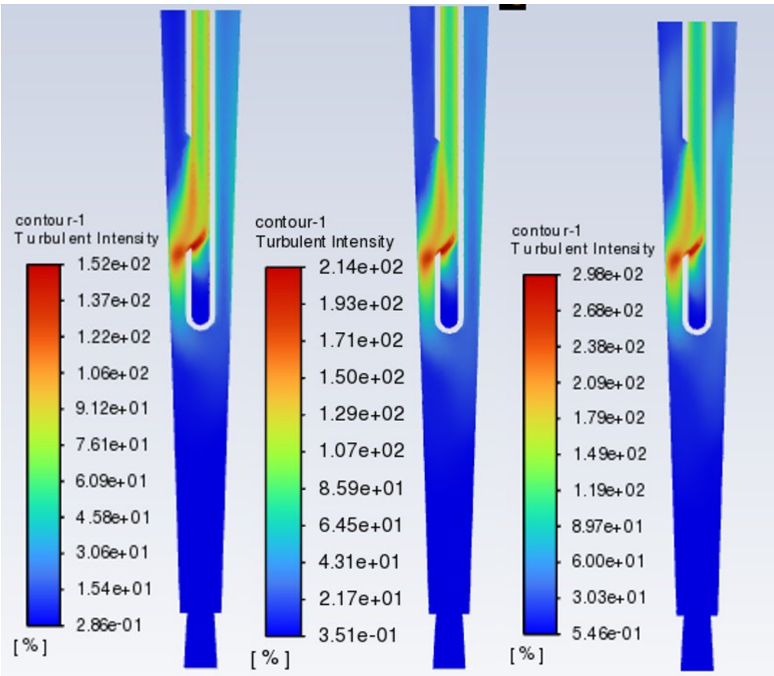

Figure 78: Turbulent intensity contour for 6 m/s, 8.6 m/s, 12 m/s for simplified geometry

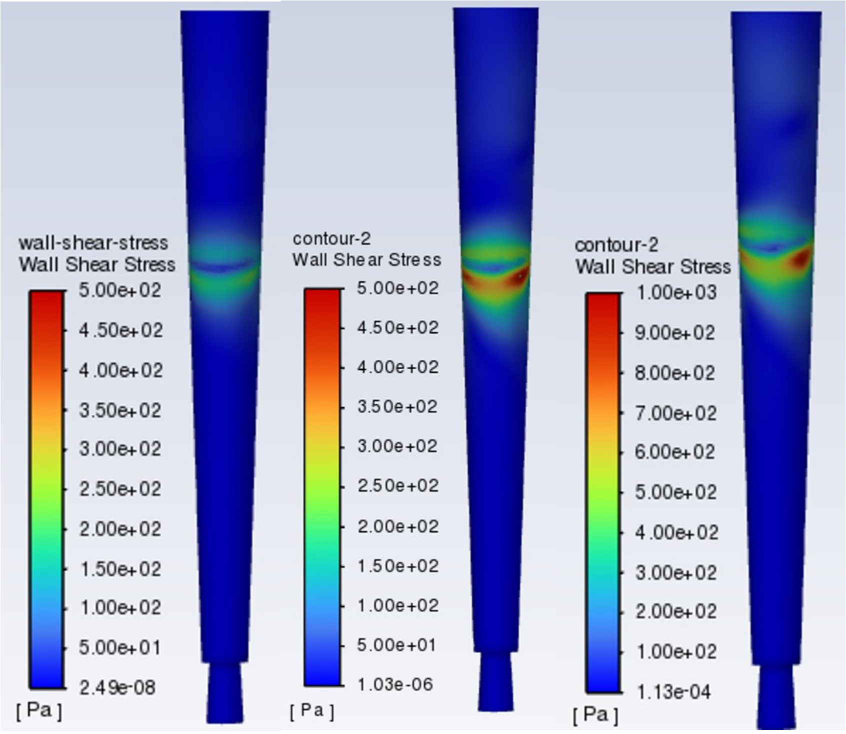

Figure 79:Wall shear stress contour for 6 m/s, 8.6 m/s, 12 m/s for simplified geometry

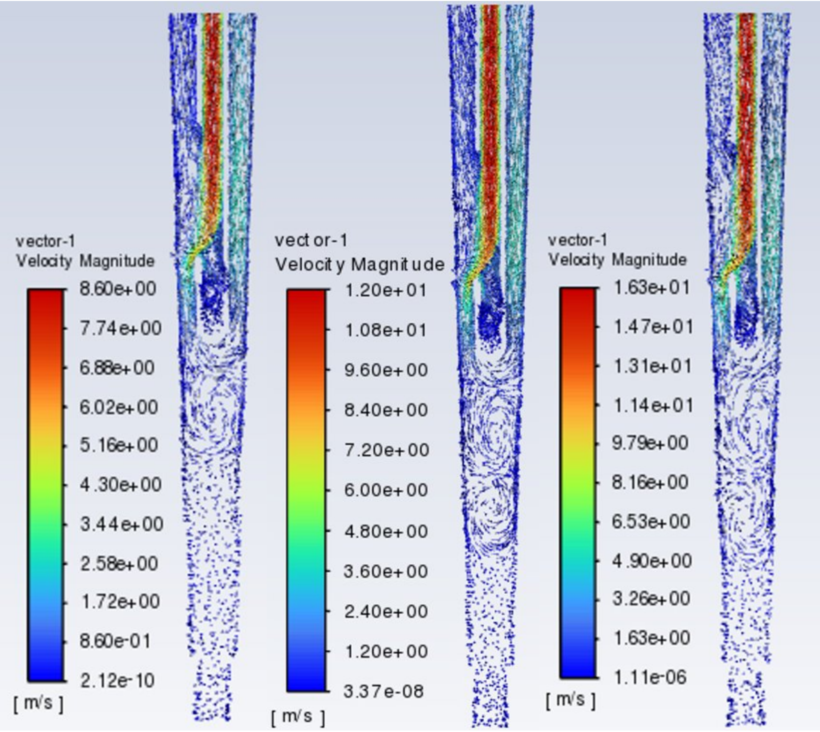

Figure 80: Vector plot for 6 m/s, 8.6 m/s, 12 m/s for simplified geometry

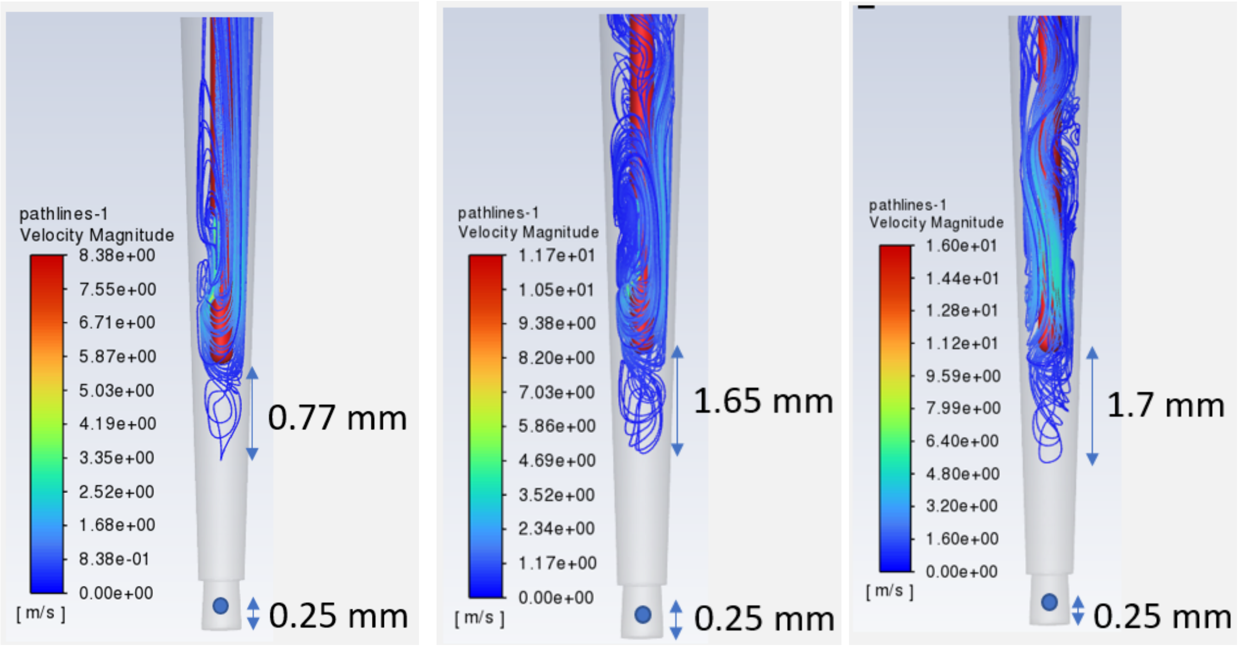

Figure 81:Streamline plot for 6 m/s, 8.6 m/s, 12 m/s for simplified geometry

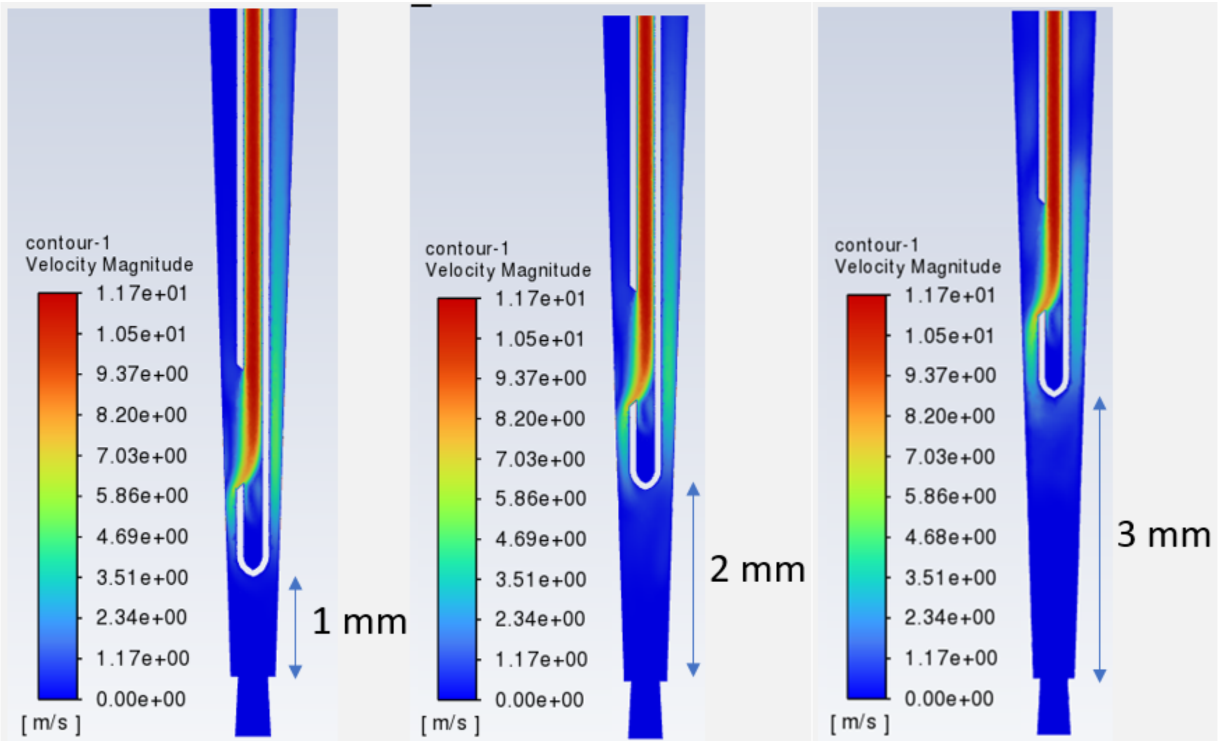

Figure 82: Velocity contour for needle insertion depth of 1 mm, 2 mm and 3 mm for simplified geometry

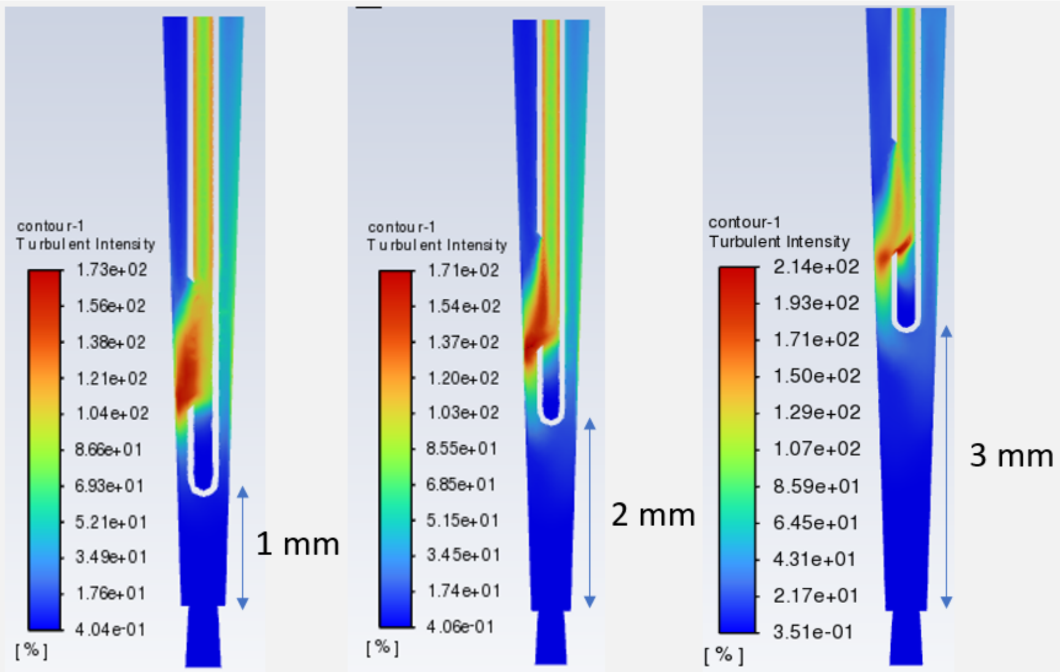

Figure 83: Turbulent intensity for needle insertion depth of 1 mm, 2 mm and 3 mm for simplified geometry

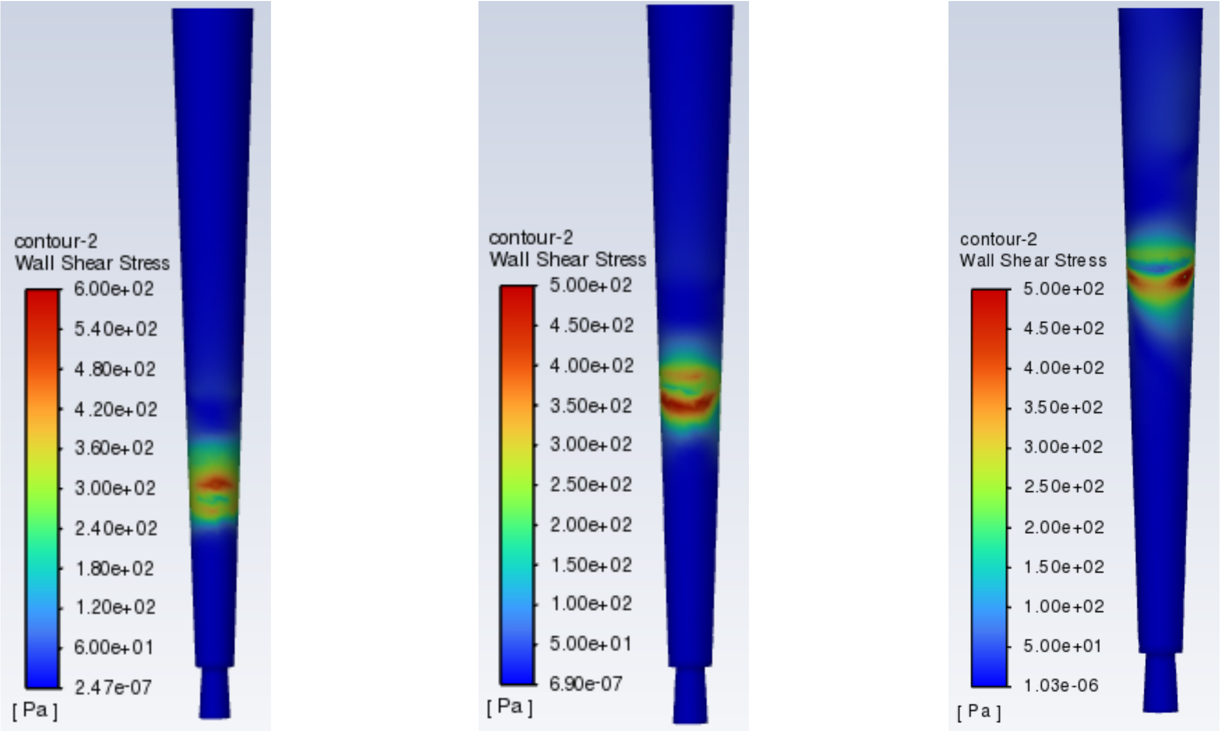

Figure 84: Wall shear stress plot for needle insertion depth of 1 mm, 2 mm and 3 mm for simplified geometry

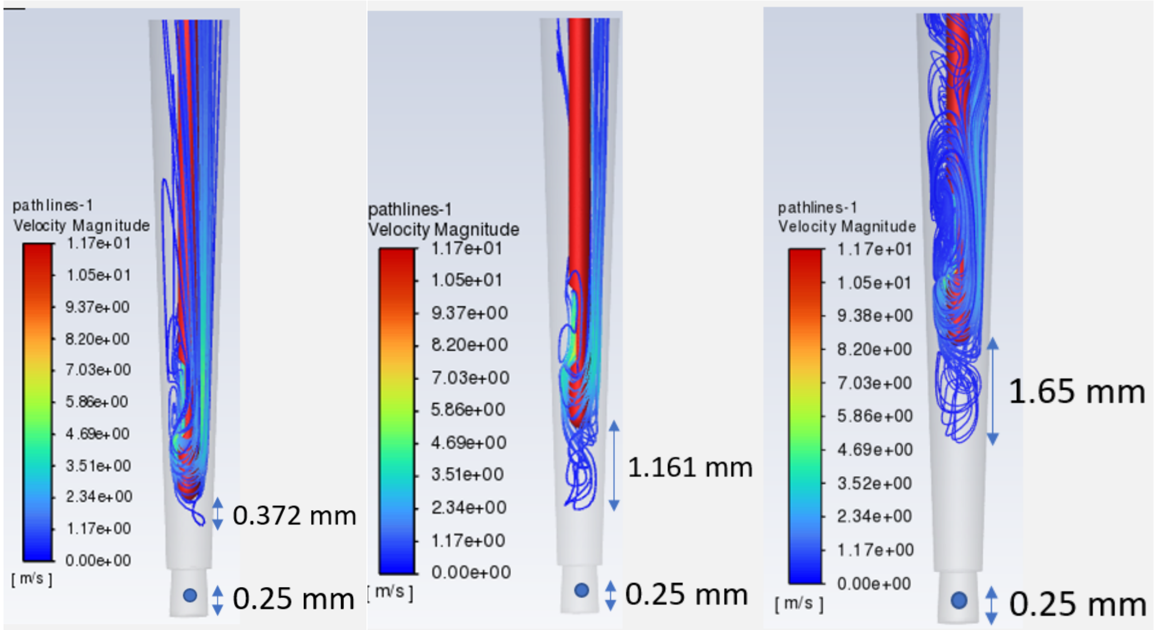

Figure 85: Streamline plot for needle insertion depth of 1 mm, 2 mm and 3 mm for simplified geometry

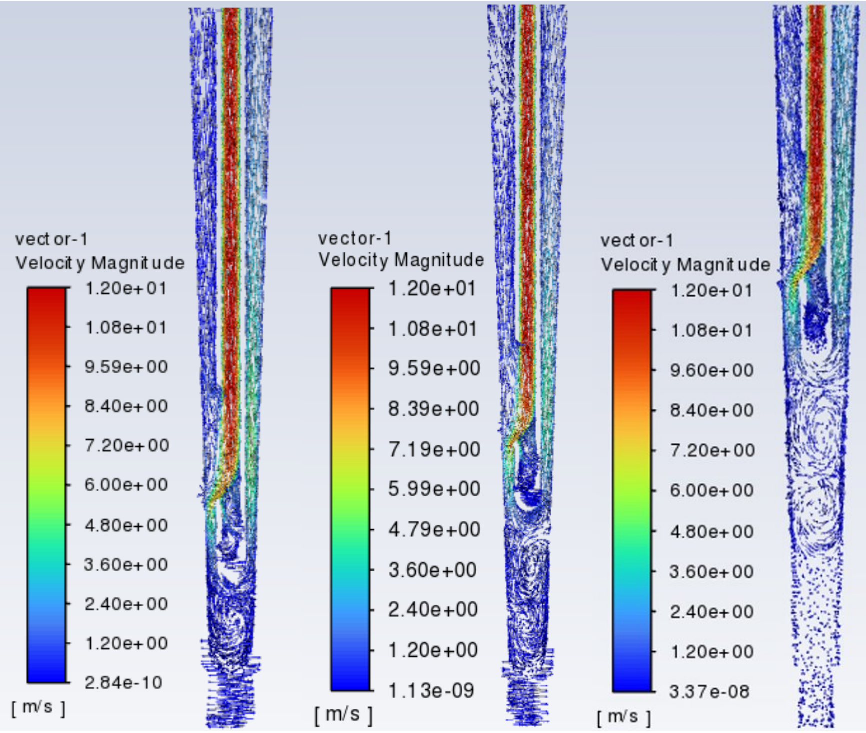

Figure 86: Vector plot for needle insertion depth of 1 mm, 2 mm and 3 mm for simplified geometry

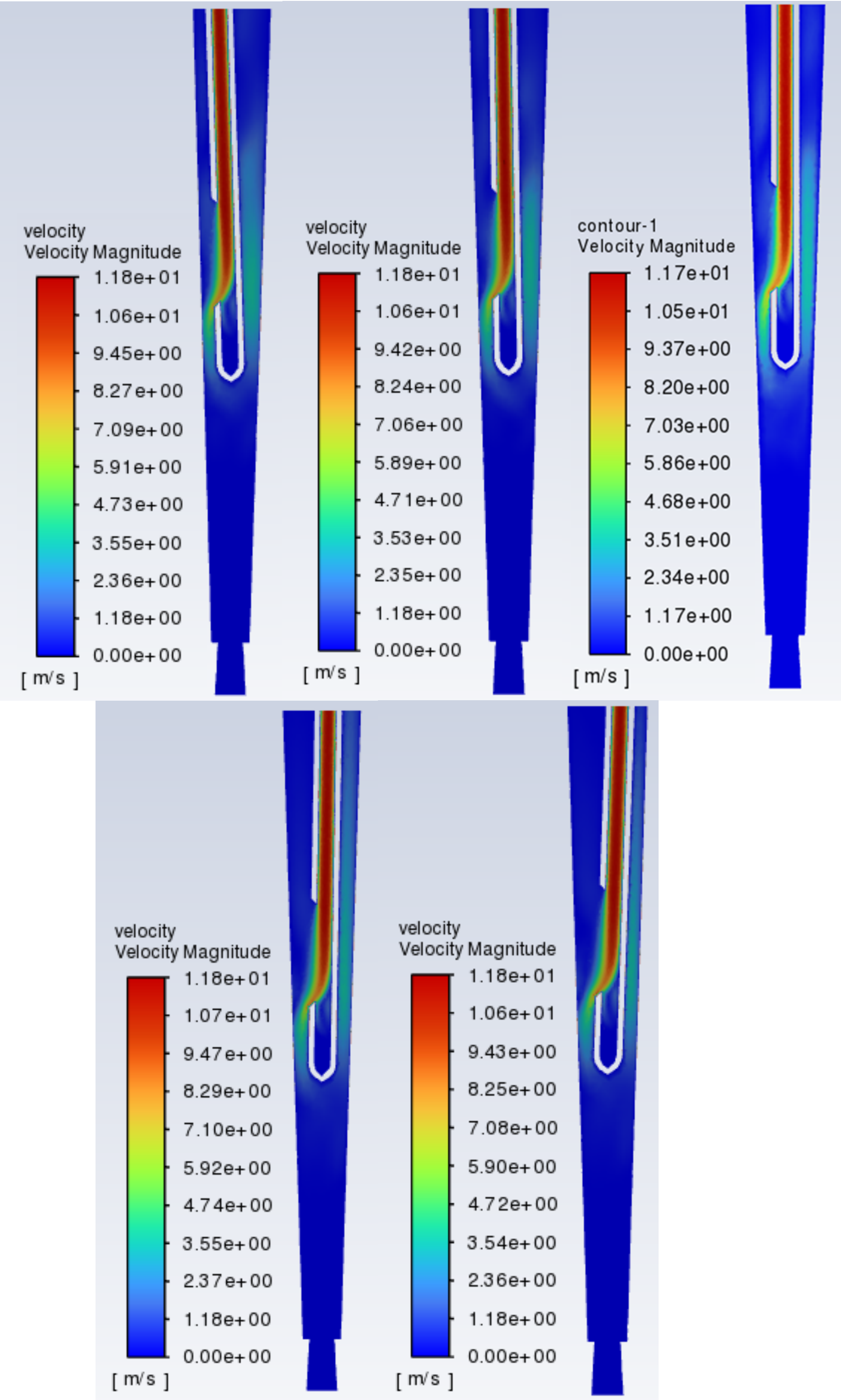

Figure 87: Velocity contour for tilt angle 2° CCW, 1° CCW, 0°, 1° CW, and 2° CW for simplified geometry

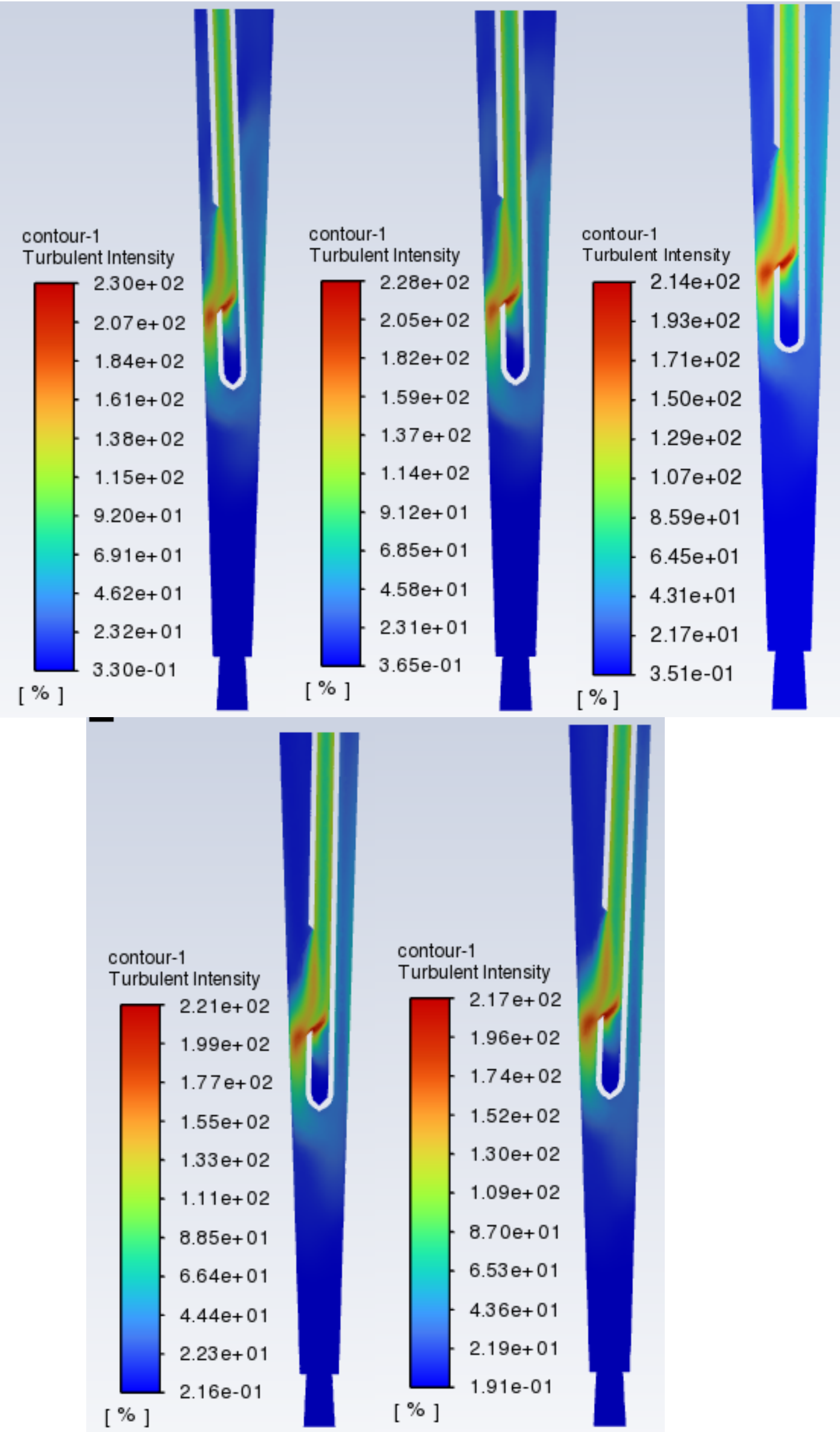

Figure 88: Turbulent intensity contour for tilt angle 2° CCW, 1° CCW, 0°, 1° CW, and 2° CW for simplified geometry

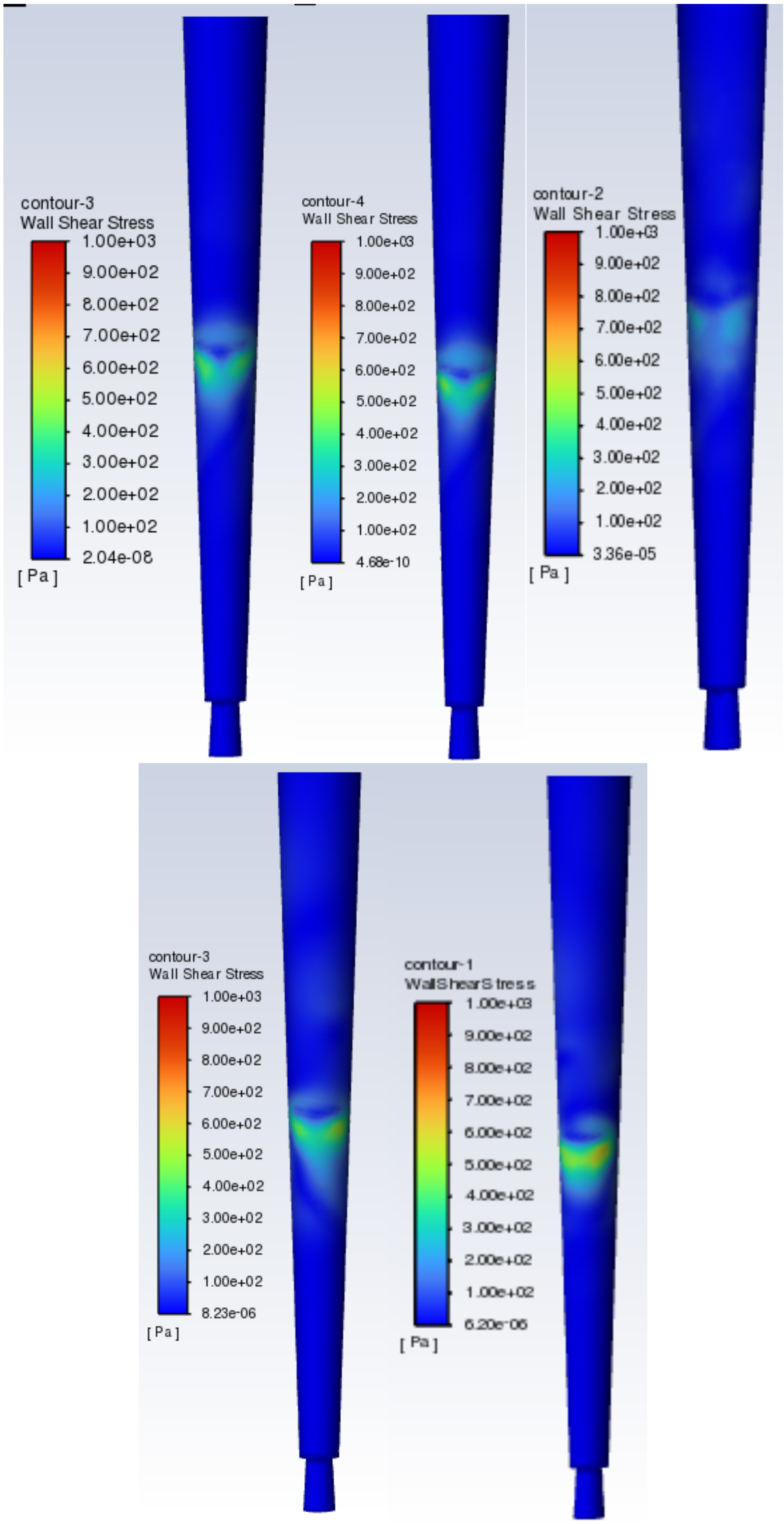

Figure 89: Wall shear stress contour for tilt angle 2° CCW, 1° CCW, 0°, 1° CW, and 2° CW for simplified geometry

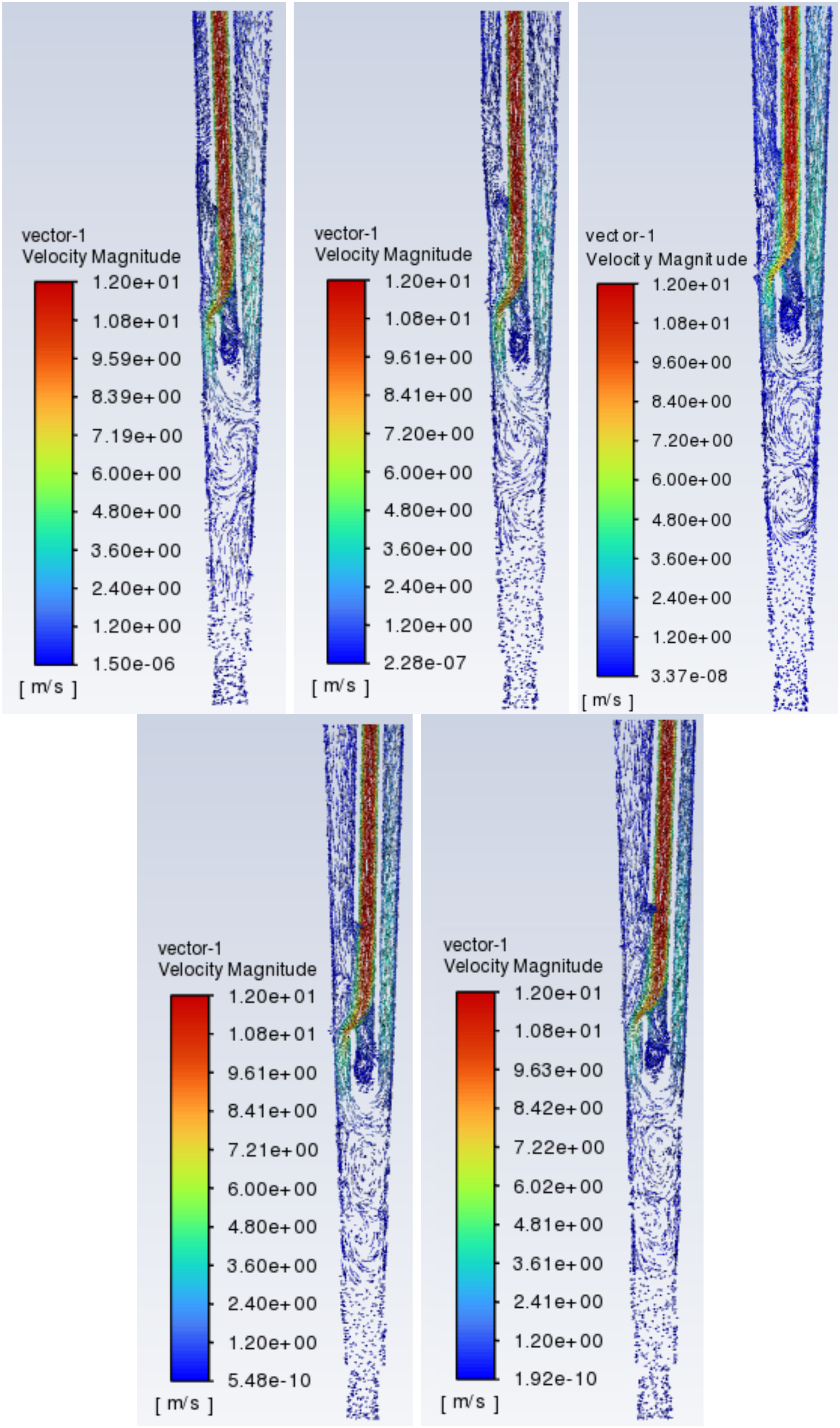

Figure 90: Vector plot for tilt angle 2° CCW, 1° CCW, 0°, 1° CW, and 2° CW for simplified geometry

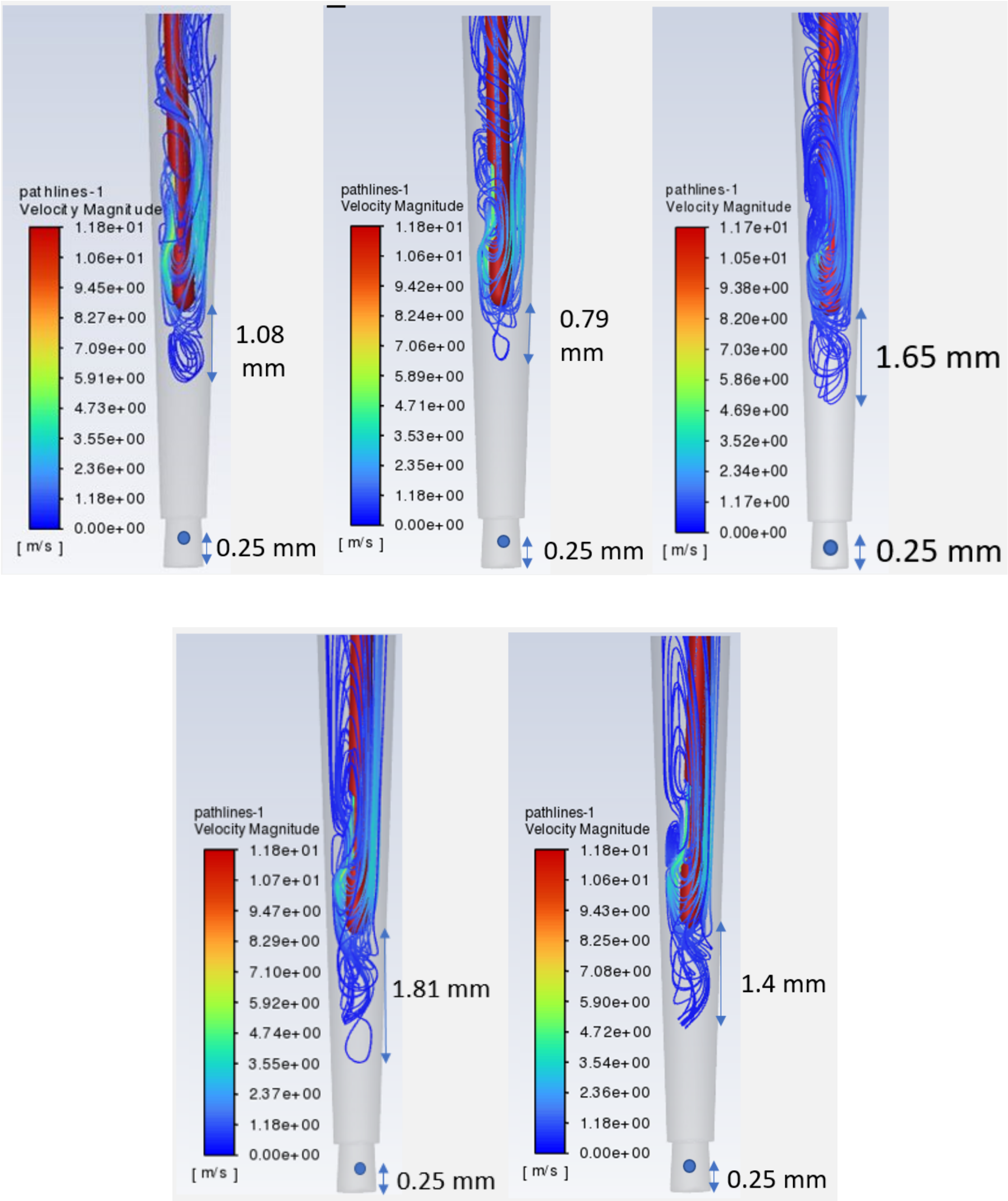

Figure 91: Streamline plot for tilt angle 2° CCW, 1° CCW, 0°, 1° CW, and 2° CW for simplified geometry

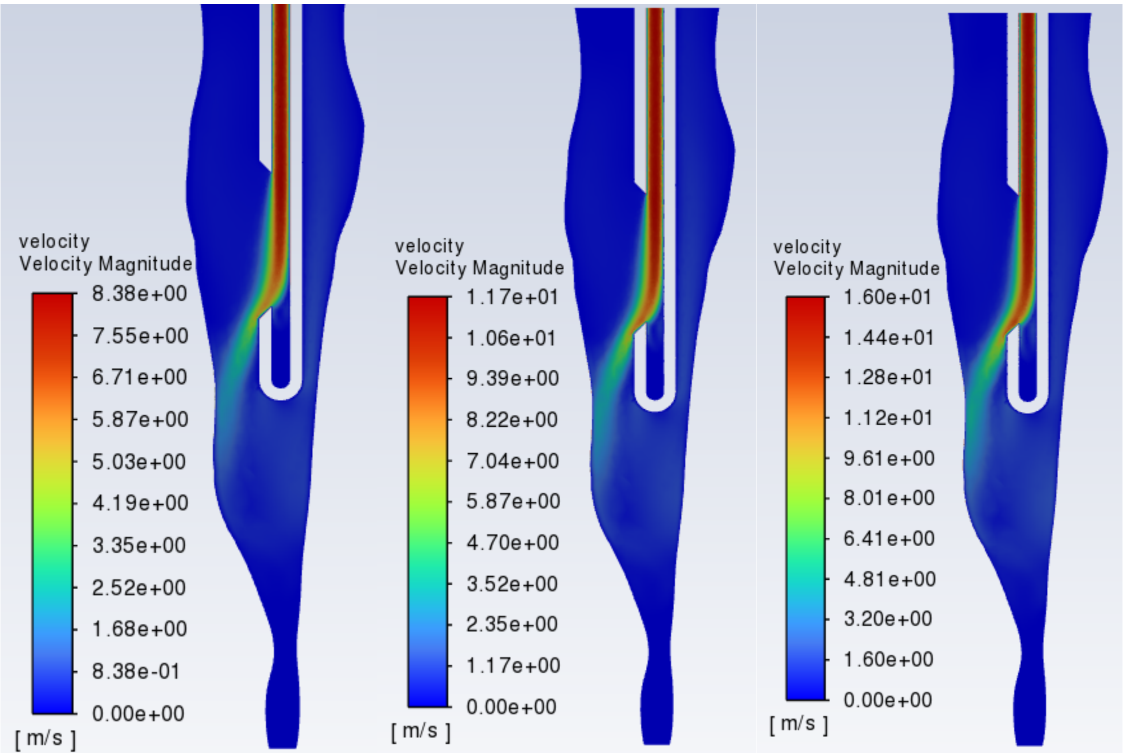

Figure 92: Velocity contour for 6 m/s, 8.6 m/s, 12 m/s for realistic geometry

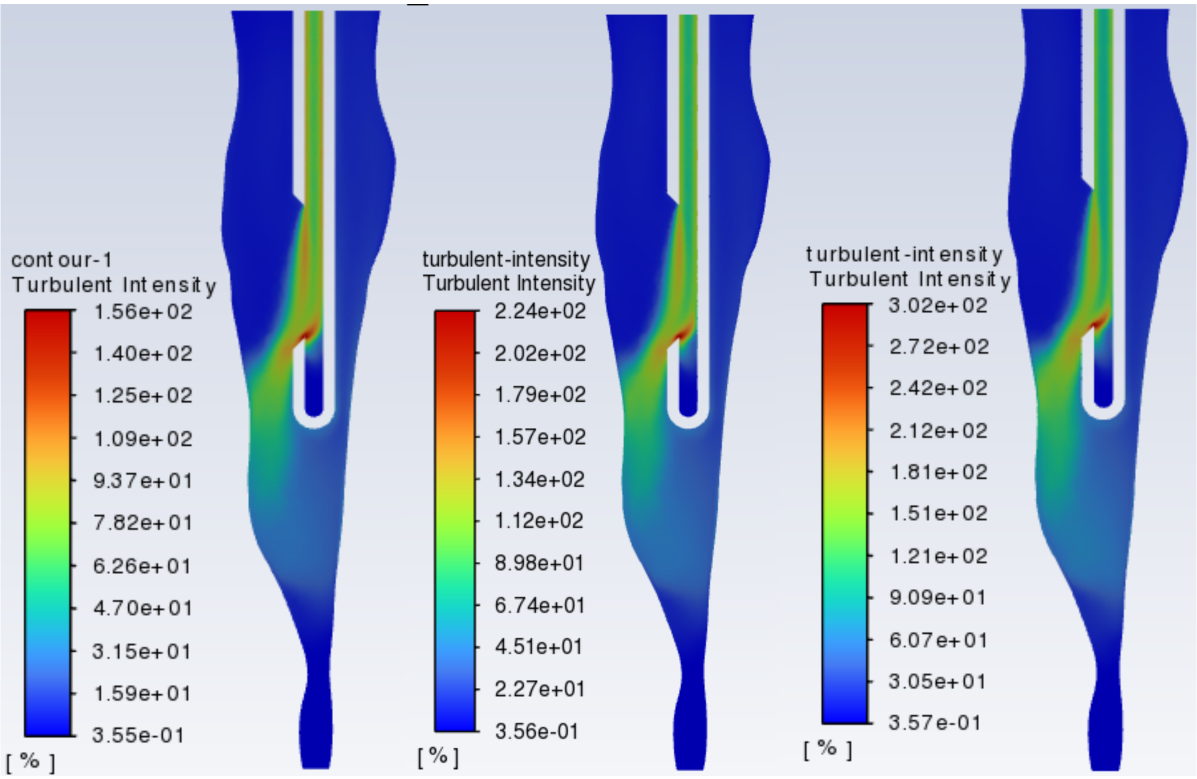

Figure 93: Turbulent intensity contour for 6 m/s, 8.6 m/s, 12 m/s for realistic geometry

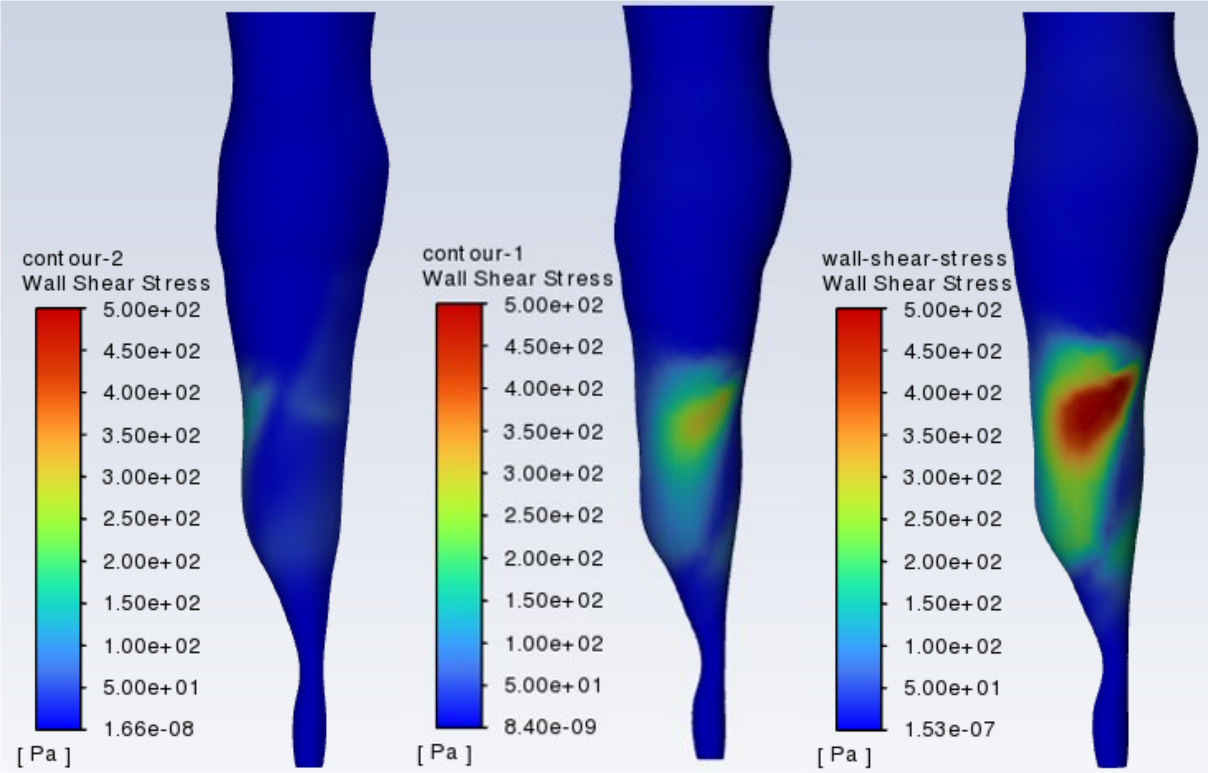

Figure 94: Wall shear stress contour for 6 m/s, 8.6 m/s, 12 m/s for realistic geometry

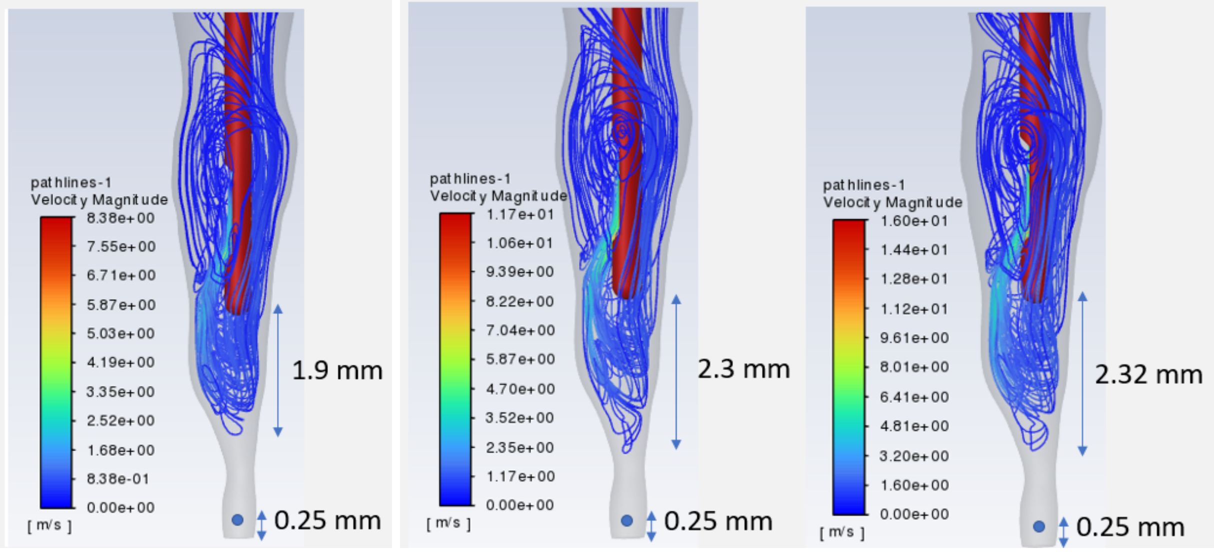

Figure 95: Streamline plot for 6 m/s, 8.6 m/s, 12 m/s for realistic geometry

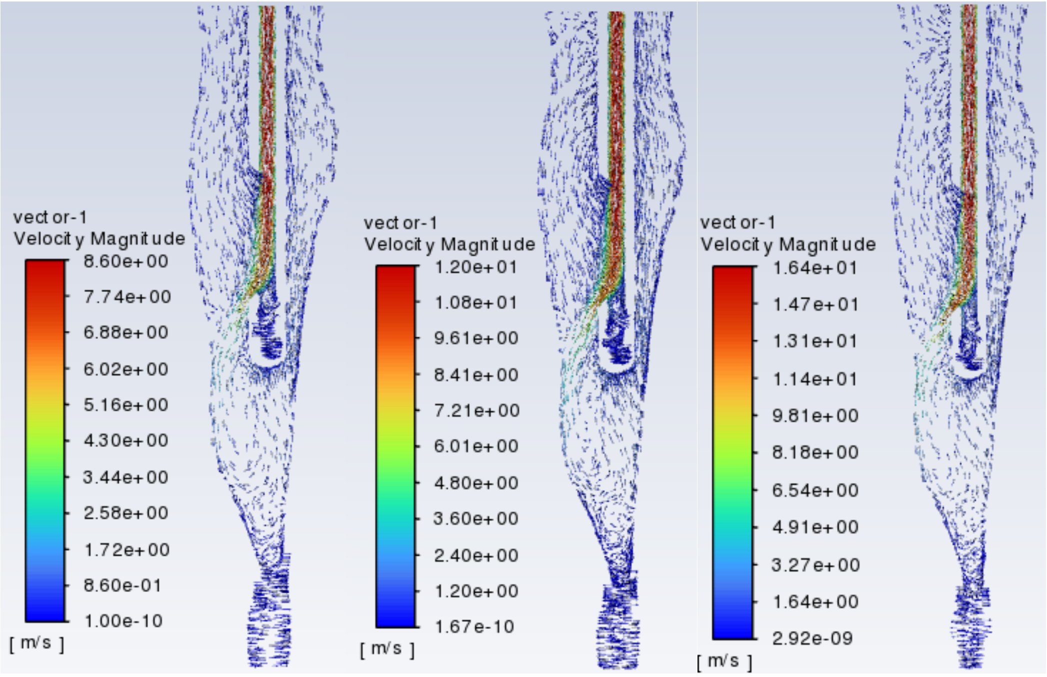

Figure 96: Vector plot for 6 m/s, 8.6 m/s, 12 m/s for realistic geometry for realistic geometry

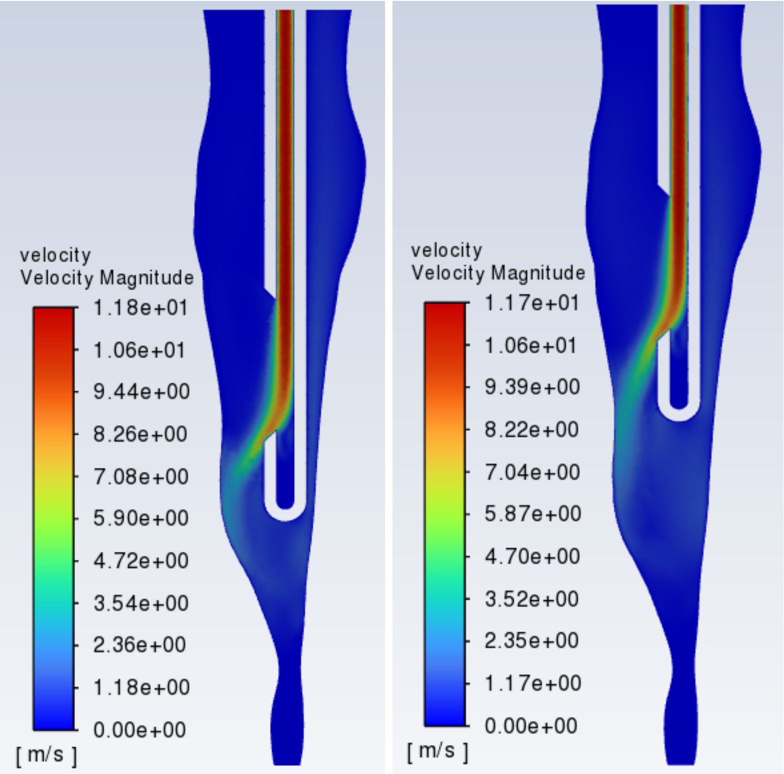

Figure 97: Velocity contour for needle insertion depth of 2 mm and 3 mm for realistic geometry

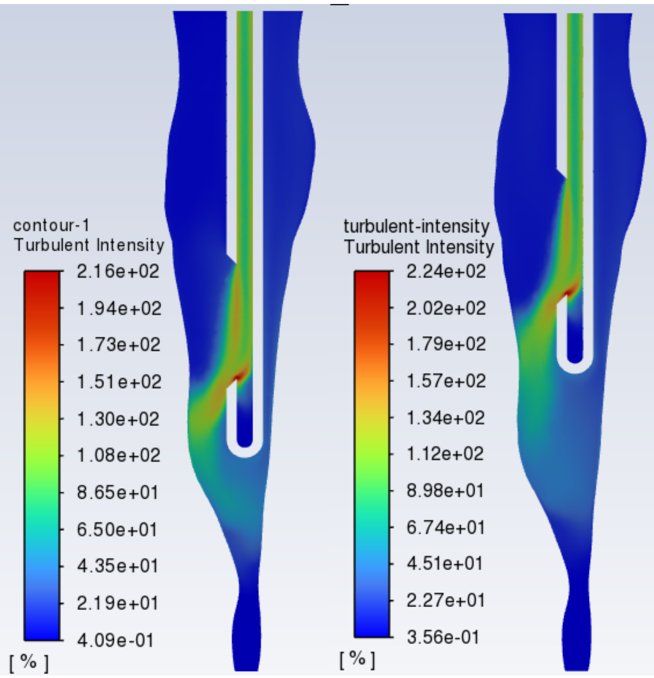

Figure 98: Turbulent intensity for needle insertion depth of 2 mm and 3 mm for realistic geometry

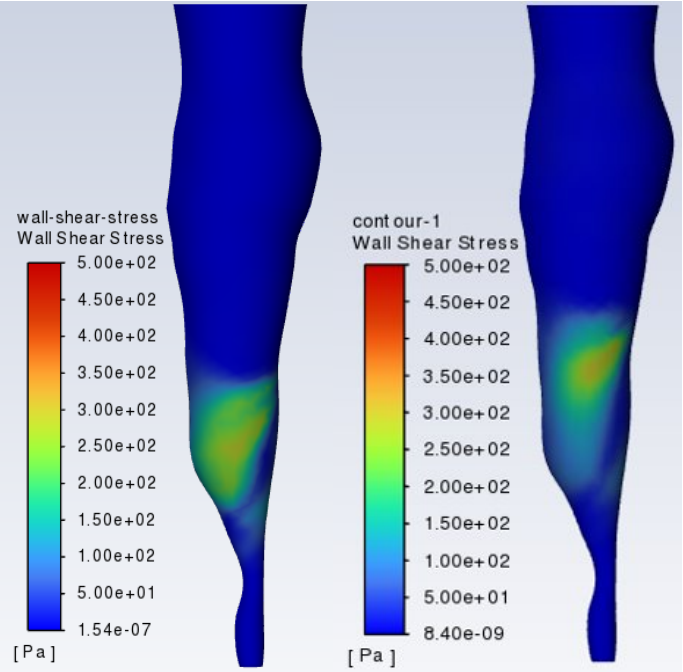

Figure 99: Wall shear stress for needle insertion depth of 2 mm and 3 mm for realistic geometry

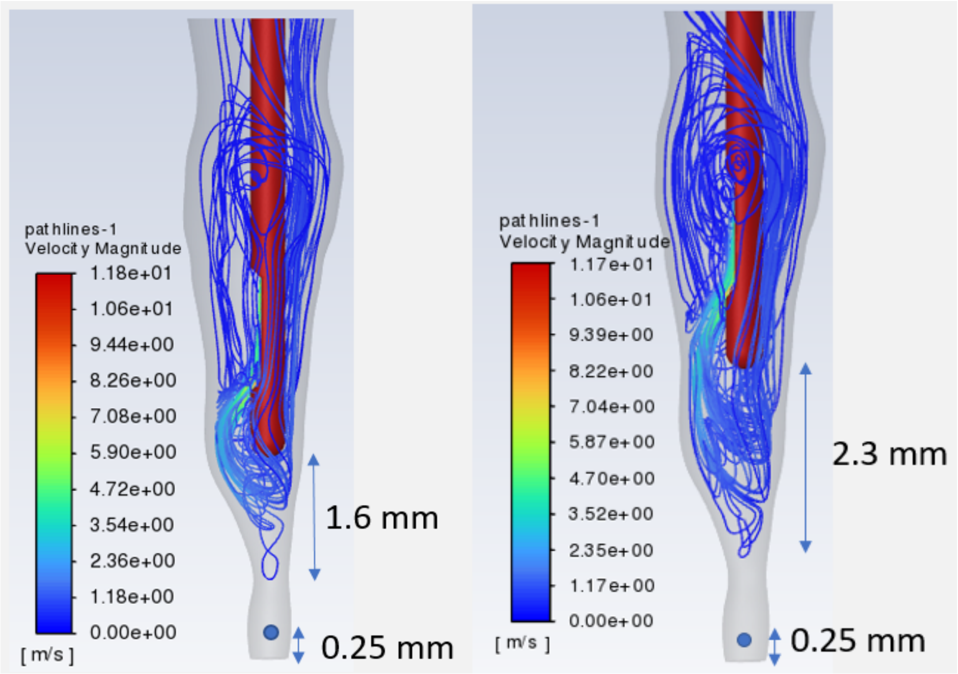

Figure 100: Streamline contour for needle insertion depth of 2 mm and 3 mm for realistic geometry

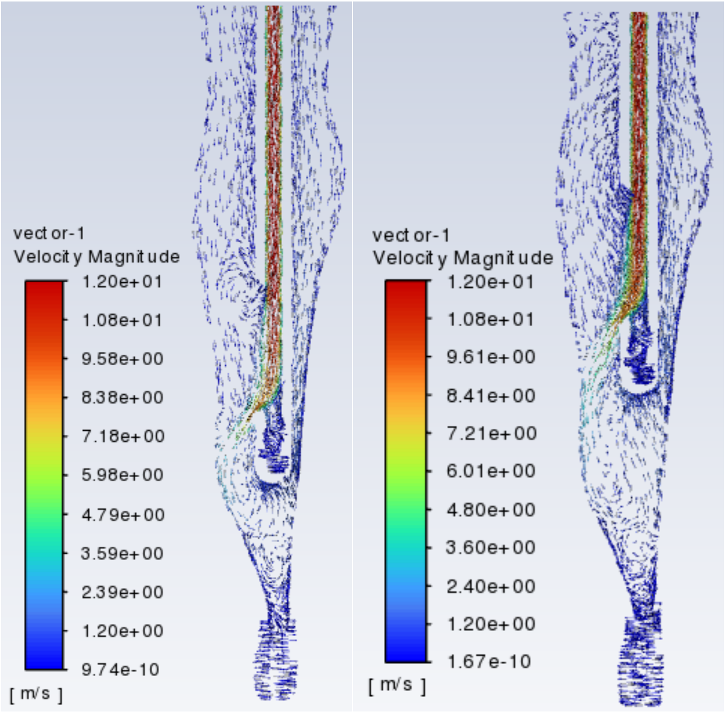

Figure 101: Vector plot for needle insertion depth of 2 mm and 3 mm for realistic geometry

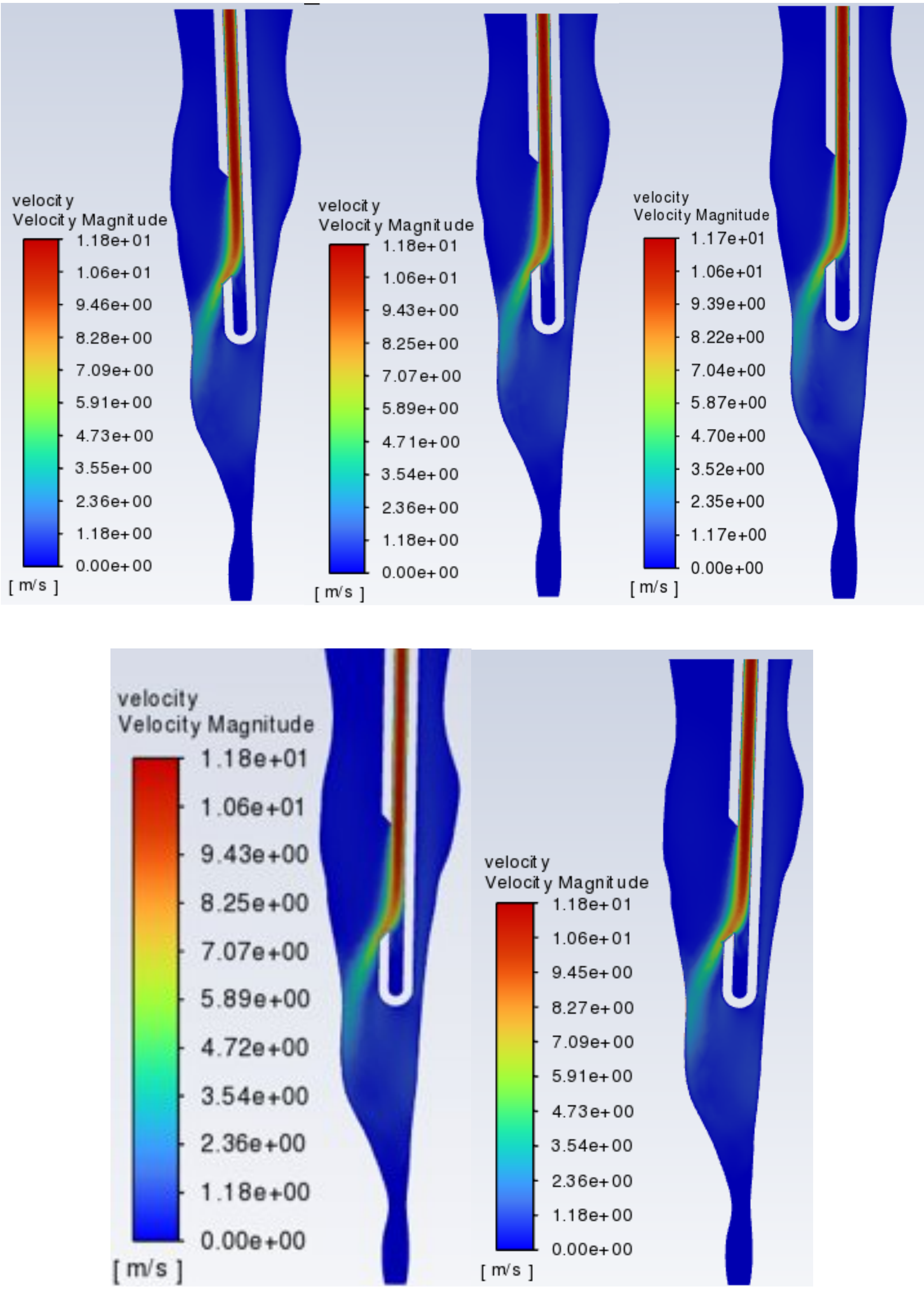

Figure 102: Velocity Contour for tilt angle 2° CCW, 1° CCW, 0°, 1° CW, and 2° CW for realistic geometry

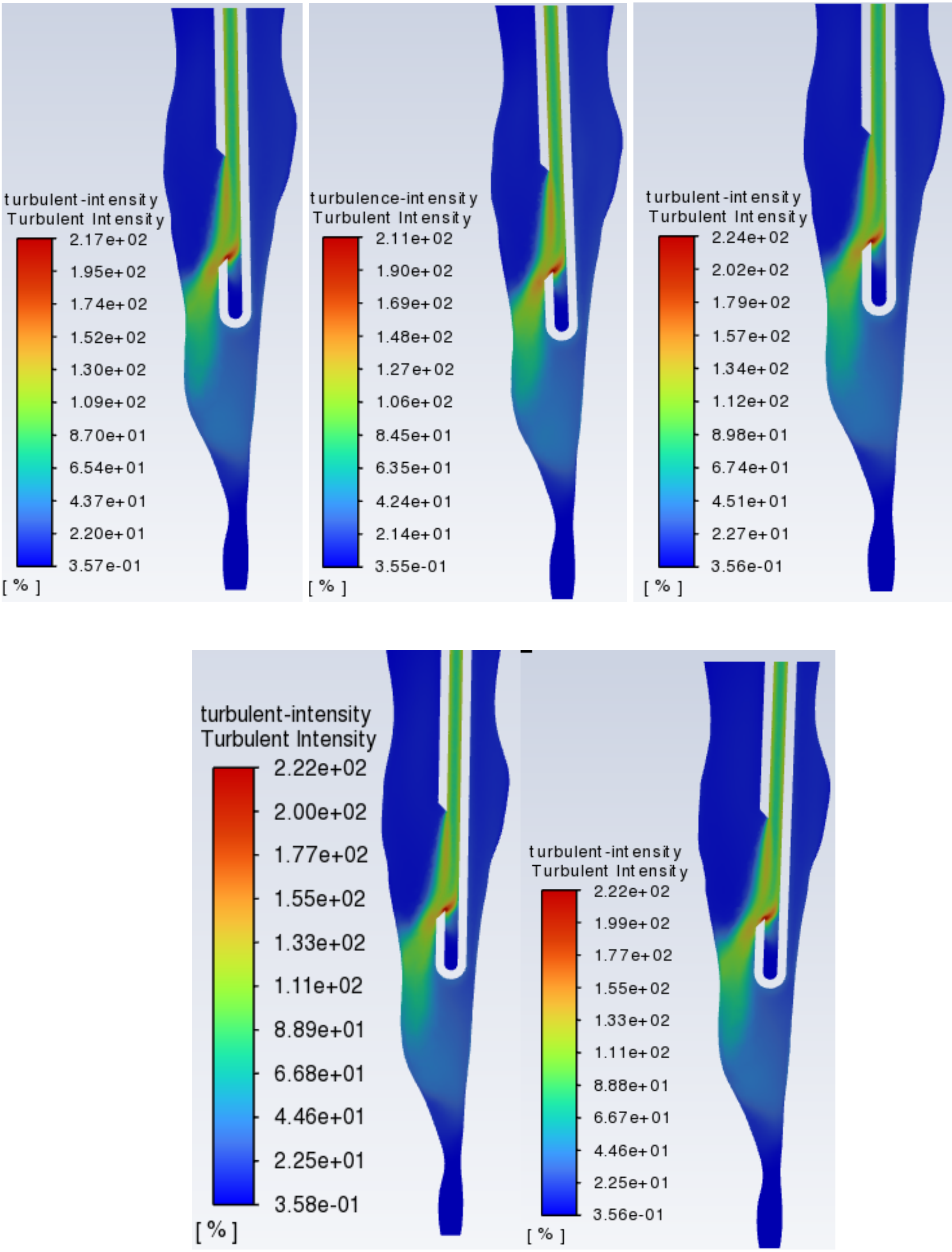

Figure 103: Turbulent Intensity contour for tilt angle 2° CCW, 1° CCW, 0°, 1° CW, and 2° CW for realistic geometry

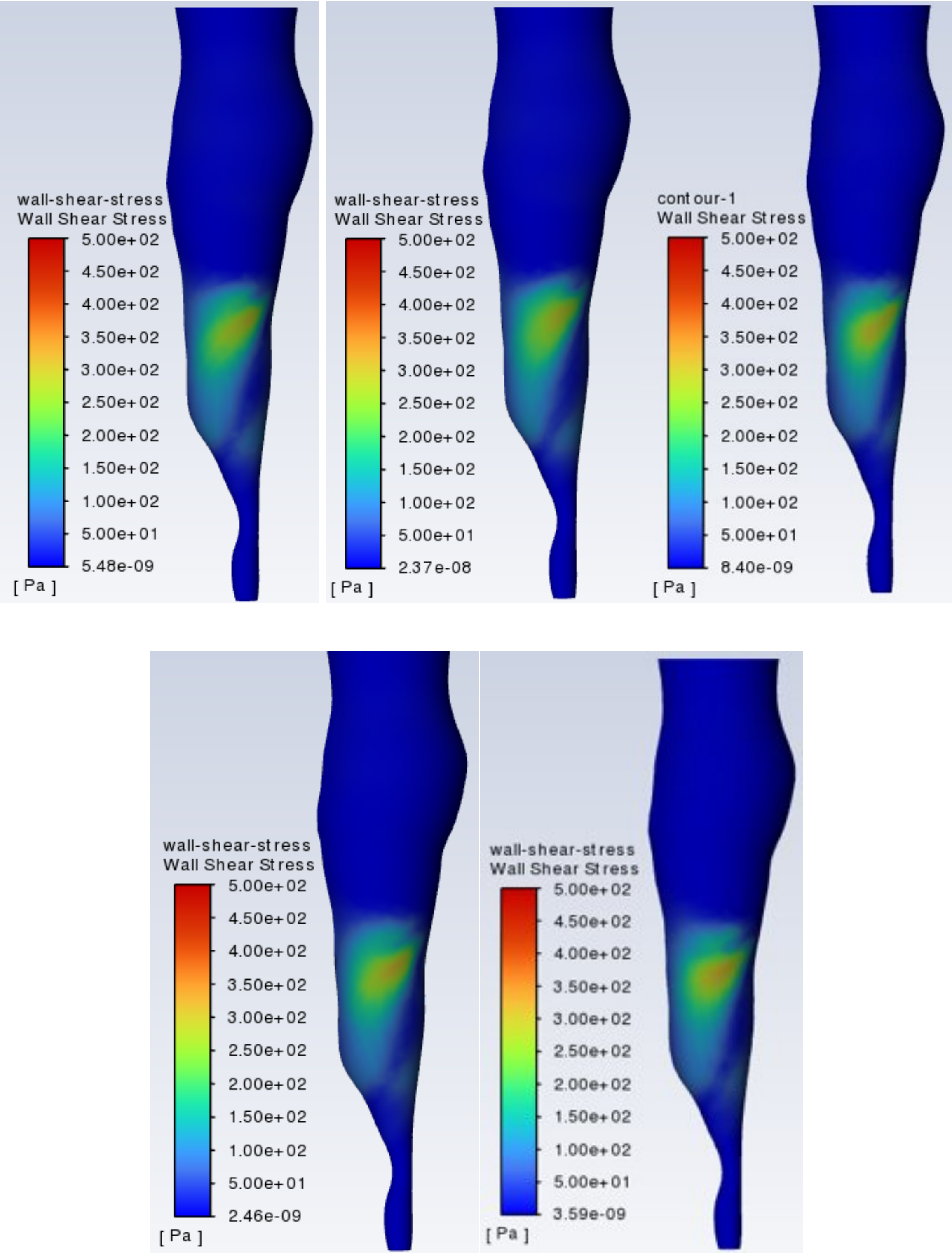

Figure 104: Wall shear stress plot for tilt angle 2° CCW, 1° CCW, 0°, 1° CW, and 2° CW for realistic geometry

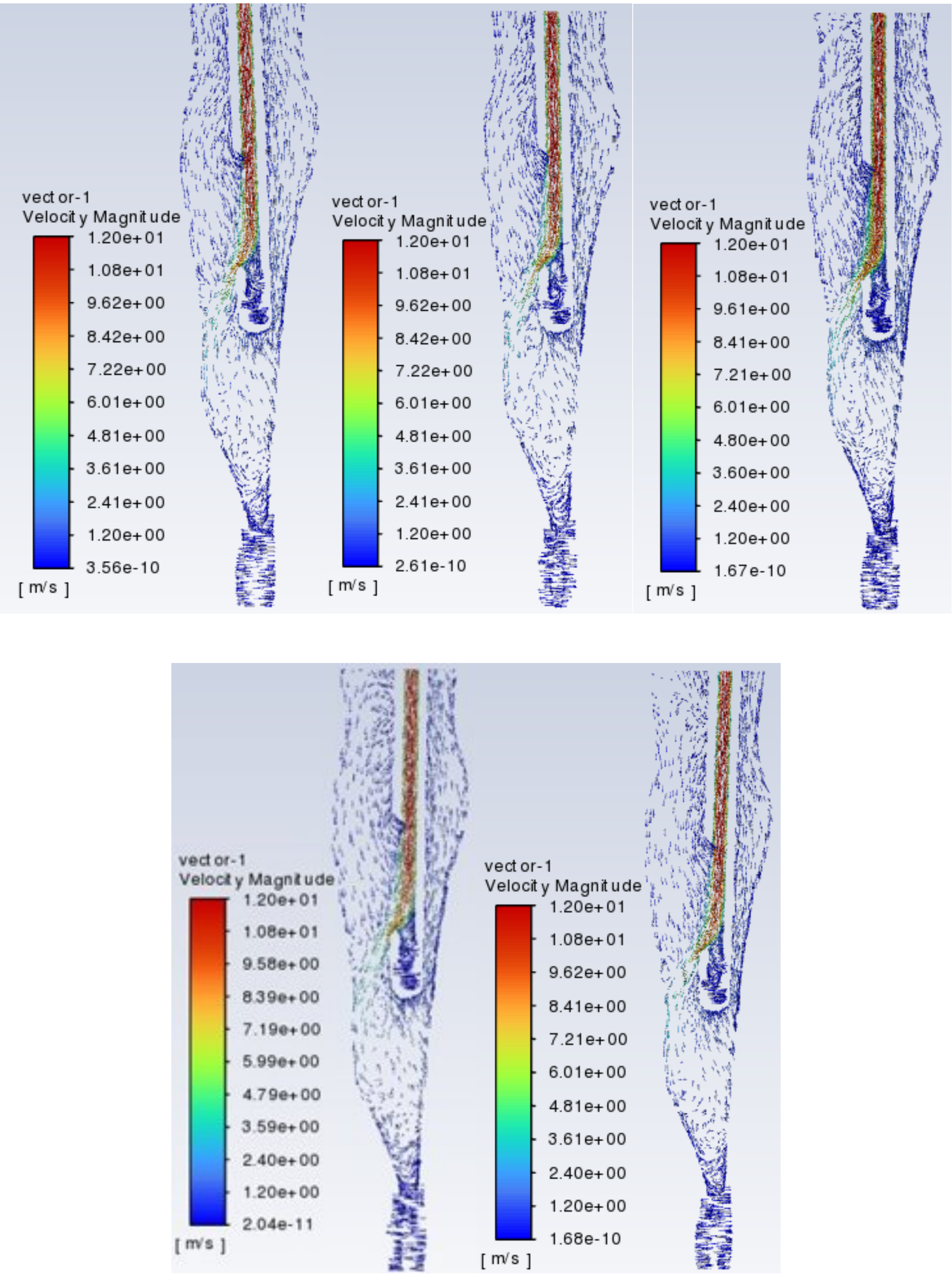

Figure 105: Vector plot for tilt angle 2° CCW, 1° CCW, 0°, 1° CW, and 2° CW for realistic geometry

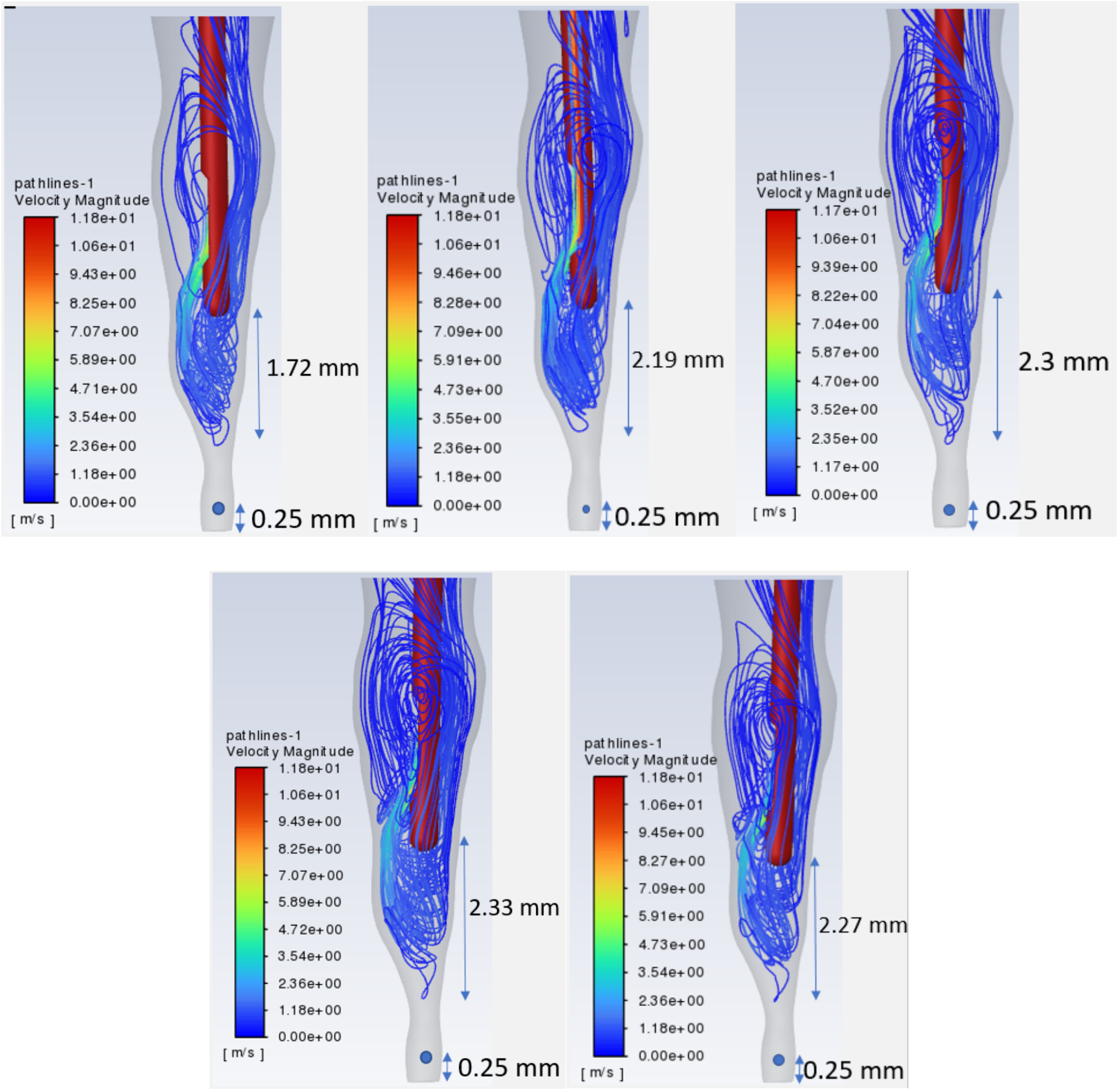

Figure 106: Streamline plot for tilt angle 2° CCW, 1° CCW, 0°, 1° CW, and 2° CW for realistic geometry

References

1. Song, M., Kim, H.-C., Lee, W., & Kim, E. (2011). Analysis of the Cause of Failure in Nonsurgical Endodontic Treatment by Microscopic Inspection during Endodontic Microsurgery. Journal of Endodontics, 37(11), 1516–1519.

2. Wong, R. (2004). Conventional endodontic failure and retreatment. Dental Clinics of North America, 48(1), 265–289.

3. Endo MS, Ferraz CC, Zaia AA, Almeida JF, Gomes BP. Quantitative and qualitative analysis of microorganisms in root-filled teeth with persistent infection: Monitoring of the endodontic retreatment. Eur J Dent 2013;7:302-9.

4. Konstantinidi, E., Psimma, Z., Chávez de Paz, L. E., & Boutsioukis, C. (2017). Apical negative pressure irrigation versus syringe irrigation: a systematic review of cleaning and disinfection of the root canal system. International Endodontic Journal, 50(11), 1034–1054.

5. Ram, Z. (1977). Effectiveness of root canal irrigation. Oral Surgery, Oral Medicine, Oral Pathology, 44(2), 306–312.

6. Ali A, Bhosale A, Pawar S, Kakti A, Bichpuriya A, Agwan MA. Current Trends in Root Canal Irrigation. Cureus. 2022 May 8;14(5):e24833. doi: 10.7759/cureus.24833. PMID: 35698671; PMCID: PMC9184175.

7. Hülsmann M, Hahn W. Complications during root canal irrigation--literature review and case reports. Int Endod J. 2000 May;33(3):186-93. doi: 10.1046/j.1365-2591.2000.00303.x. PMID: 11307434.

8. Boutsioukis C, Lambrianidis T, Kastrinakis E, Bekiaroglou P. Measurement of pressure and flow rates during irrigation of a root canal ex vivo with three endodontic needles. Int Endod J. 2007 Jul;40(7):504-13. doi: 10.1111/j.1365-2591.2007.01244.x. Epub 2007 Feb 27. PMID: 17326784.

9. Boutsioukis C, Lambrianidis T, Kastrinakis E. Irrigant flow within a prepared root canal using various flow rates: a Computational Fluid Dynamics study. Int Endod J. 2009 Feb;42(2):144-55. doi: 10.1111/j.1365-2591.2008.01503.x. PMID: 19134043.

10. Boutsioukis C, Verhaagen B, Versluis M, Kastrinakis E, van der Sluis LW. Irrigant flow in the root canal: experimental validation of an unsteady Computational Fluid Dynamics model using high-speed imaging. Int Endod J. 2010 May;43(5):393-403. doi: 10.1111/j.1365-2591.2010.01692.x. PMID: 20518932.

11. Boutsioukis C, Verhaagen B, Versluis M, Kastrinakis E, Wesselink PR, van der Sluis LW. Evaluation of irrigant flow in the root canal using different needle types by an unsteady computational fluid dynamics model. J Endod. 2010 May;36(5):875-9. doi: 10.1016/j.joen.2009.12.026. Epub 2010 Feb 21. PMID: 20416437.

12. Boutsioukis C, Lambrianidis T, Verhaagen B, Versluis M, Kastrinakis E, Wesselink PR, van der Sluis LW. The effect of needle-insertion depth on the irrigant flow in the root canal: evaluation using an unsteady computational fluid dynamics model. J Endod. 2010 Oct;36(10):1664-8. doi: 10.1016/j.joen.2010.06.023. Epub 2010 Aug 17. PMID: 20850673.

13. Boutsioukis C, Gogos C, Verhaagen B, Versluis M, Kastrinakis E, Van der Sluis LW. The effect of root canal taper on the irrigant flow: evaluation using an unsteady Computational Fluid Dynamics model. Int Endod J. 2010 Oct;43(10):909-16. doi: 10.1111/j.1365-2591.2010.01767.x. Epub 2010 Jul 5. PMID: 20618877.

14. Quadri, Zeya & Zeya, Kyaw & Faisal, Mohammad. (2014). Using CFD as a tool for analysis of endodontic irrigation: Maxillary and mandibular teeth cases

15. Teja KV, Ramesh S, Vasundhara KA, Janani KC, Jose J, Battineni G. A new innovative automated root canal device for syringe needle irrigation. J Taibah Univ Med Sci. 2021 Aug 19;17(1):155-158. doi: 10.1016/j.jtumed.2021.07.011. PMID: 35140579; PMCID: PMC8801474.

16. Zhou, N., Huang, Z., Yu, M. et al. Influence of needle working length and root canal curvature on irrigation: a computational fluid dynamics analysis based on a real tooth. BMC Oral Health 22, 179 (2022). https://doi.org/10.1186/s12903-022-02205-2

17. Razumova S, Brago A, Howijieh A, Barakat H, Manvelyan A, Kozlova Y. An In Vitro Evaluation Study of the Geometric Changes of Root Canal Preparation and the Quality of Endodontic Treatment. Int J Dent. 2020 Aug 12;2020:8883704. doi: 10.1155/2020/8883704. PMID: 32849874; PMCID: PMC7441414.

18. V. Gopikrishna, BDS, MDS, Ph.D. Grossman’s Endodontic Practice. Chennai, India, Wolters Kluwer, 2020.